Summer 2020

Synthesis and Characterization of Earth Abundant Metal Phosphide Photocatalysts for the Reverse Water Gas Shift Reaction

John D. Springer
Western Washington University, springj5@wwu.edu

Synthesis and Characterization of Earth Abundant Metal Phosphide Photocatalysts for the Reverse Water Gas Shift Reaction

By

John D. Springer

Accepted in Partial Completion
of the Requirements for the Degree
Master of Science

ADVISORY COMMITTEE

Dr. Mark Bussell, Chair

Dr. Robert Berger

Dr. David Rider

GRADUATE SCHOOL

David L. Patrick, Dean

Master's Thesis

In presenting this thesis in partial fulfillment of the requirements for a master's degree at Western Washington University, I grant to Western Washington University the non-exclusive royalty-free right to archive, reproduce, distribute, and display the thesis in any and all forms, including electronic format, via any digital library mechanisms maintained by WWU.

I represent and warrant this is my original work, and does not infringe or violate any rights of others. I warrant that I have obtained written permissions from the owner of any third party copyrighted material included in these files.

I acknowledge that I retain ownership rights to the copyright of this work, including but not limited to the right to use all or part of this work in future works, such as articles or books.

Library users are granted permission for individual, research and non-commercial reproduction of this work for educational purposes only. Any further digital posting of this document requires specific permission from the author.

Any copying or publication of this thesis for commercial purposes, or for financial gain, is not allowed without my written permission.

John D. Springer

July 29th, 2020

Synthesis and Characterization of Earth Abundant Metal Phosphide Photocatalysts for the Reverse Water Gas Shift Reaction

A Thesis
Presented to
The Faculty of
Western Washington University

In Partial Fulfillment
Of the Requirements for the Degree
Master of Science

by
John D. Springer
July, 2020

Abstract

This thesis work focuses on the synthesis and characterization of photocatalysts composed of metal phosphide nanoparticles on a titania (TiO_2) support for the conversion of carbon dioxide (CO_2) to carbon monoxide (CO) via the reverse water gas shift (RWGS) reaction. The CO product can be subsequently converted to solar fuels such as methanol (CH_3OH), thus lowering the carbon footprint associated with the combustion of liquid fuels. The photocatalysts are composed of a tunable light absorber, indium-gallium phosphide ($In_xGa_{1-x}P$), and nickel phosphide (Ni_2P) as a co-catalyst, on TiO_2. The photocatalysts are characterized using diffuse reflectance ultraviolet-visible (UV-Vis) spectroscopy to determine band gaps, and methods such as X-ray diffraction (XRD), energy dispersive spectroscopy (EDS), and X-ray photoelectron spectroscopy (XPS) to probe structure and composition. This combination of characterization techniques allows for synthetic strategies to probe how varying the In/Ga molar ratio affects photocatalyst properties, which leads to tunability in the band gaps of the materials. The Ni_2P cocatalyst has been synthesized onto the $In_xGa_{1-x}P/TiO_2$, with the expectation that photoexcited electrons will be transferred to Ni_2P with sufficient energy to drive the RWGS reaction. The RWGS activity will be tested in a flow reactor system outfitted with a xenon arc lamp as the light source and a gas chromatograph (GC) for determination of CO_2 conversion and product selectivity under light and dark conditions at varying reaction temperatures.

Acknowledgements

Thesis Committee Chair:	Dr. Mark E. Bussell
Thesis Committee Members:	Dr. David Rider
	Dr. Robert Berger
Research Group Members:	Jake Schare, Reilly Lynch, Ryan Hagmann, Sam Baldwin
Instrument Technicians:	Sam Danforth, Kyle Mikkelsen, Michael Kraft, Colin Hanson, Charles Wandler
Financial Support:	Joint Center for Deployment and Research in Earth Abundant Materials (JCDREAM)
Western Washington University:	Advanced Materials Science and Engineering Center, Chemistry Department, Scientific and Technical Services

Table of Contents

List of Figures and Schemes

List of Tables

Chapter 1: Introduction

Fossil fuels are limited to reserves within the earth's crust and this resource is predicted to be depleted within the next 50 years if society does not find an alternate energy supply.[1] If the predicted fuel crisis is not alarming enough, something else to consider is the consequences that burning fossil fuels have on our environment. Average global temperature has increased by 1.5 K since the industrial revolution, slowly melting icecaps and impacting human habitats such as Greenland that depend on structurally sound sea-ice structures.[2,3] In addition, the excessive melting of the icecaps is leading to higher oceanic tides, which has dire flooding effects on small islands; especially communities that are protected from the tides of the ocean by dikes. The 1.5 K temperature increase has grabbed our attention, but it is minute compared to the expected 4.1-4.8 K increase expected by the end of the 21st century.[3,4]

Atmospheric carbon dioxide (CO_2) contributes 60% to global climate change,[5] and CO_2 concentration has increased from 280 to 412 parts per million (ppm) since the industrial revolution.[6] The atmospheric CO_2 concentration is expected to increase dramatically, given the projected increasing in carbon emissions from 32 gigatons per year (Gt/yr) in 2013 to 45 Gt/yr in 2040.[6] This thesis research aims to contribute to the reduction of the global carbon footprint by working towards a fossil fuel replacement. Photosynthesized liquid hydrocarbons could replace fossil fuels, helping to avoid the fuel crisis that approaches as our fossil fuel resources come closer to depletion.

Hydrogen fuel cells are an attractive alternative to fossil fuel combustion, due to the clean production of electricity and the high energy density (by mass) of hydrogen. Unfortunately, the displacement of fossil fuels with hydrogen fuel cells would require uprooting the deeply

established storage and transportation infrastructure currently in place. However, synthesized hydrocarbons are much easier to integrate, as storage and transportation methods would be mostly unchanged.

This project aims to develop affordable, robust, and tunable photocatalysts for the reverse water gas shift (RWGS) reaction (Equation 1.1),[7] which yields carbon monoxide (CO).

$$CO_2 + H_2 \longrightarrow CO + H_2O \qquad \Delta H° = 42.1 \text{ kJ/mol} \qquad \mathbf{1.1}$$

This reaction is energy intensive due to its endothermic nature and its high activation energy (222.2 kJ/mol).[8] Harnessing solar energy through photocatalysis could serve as a sustainable route for converting CO_2 to CO. Fuels such as ethanol, methanol, and a variety of longer chain liquid hydrocarbon fuels can then be synthesized using CO as a reactant in the Fischer-Tropsch process,

$$n\text{CO} + (2n + 1)\text{H}_2 \longrightarrow \text{C}_n\text{H}_{(2n+2)} + n\text{H}_2\text{O} \qquad \mathbf{1.2}$$

overall resulting in a method for solar fuel synthesis, thus slowing the depletion of fossil fuels and reducing CO_2 emissions.[9] Titania (TiO_2) is known to be a catalyst for the RWGS reaction, making it a good choice as a support material for a RWGS photocatalyst. However, its activity towards the RWGS reaction is reported to be only about 0.012 millimoles of CO per gram of catalyst per hour (mmol g-cat^{-1} h^{-1}) under ultraviolet (UV) light irradiation using a 1:1 CO_2/H_2 flow-rate of 20 mL/min at 373 K.[10] The low activity can be explained primarily by the fact that, due to its wide band gap of 3.18 eV, TiO_2 absorbs only a small fraction of the terrestrial solar spectrum (Figure 1.1).[10]

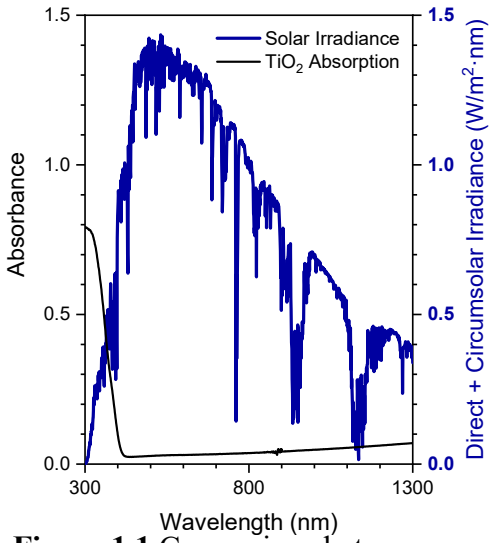

Figure 1.1 Comparison between terrestrial solar irradiance (blue) and TiO_2 absorbance (black).

For this reason, it is common to use a light absorber in tandem with TiO_2.

Figure 1.2 includes absorption spectra of ~3 nm indium-gallium phosphide nanoparticles having the general formula $In_xGa_{1-x}P$. These spectra show that by varying x in $In_xGa_{1-x}P$ absorption peaks move within the visible region (from ~500 nm for $In_{0.3}Ga_{0.7}P$ to ~600 nm for $In_{0.75}Ga_{0.25}P$, indicating a decrease in band gap with higher indium content). Absorption in the visible region makes $In_xGa_{1-x}P$ a candidate for dispersion onto TiO_2 as a visible light harvester.

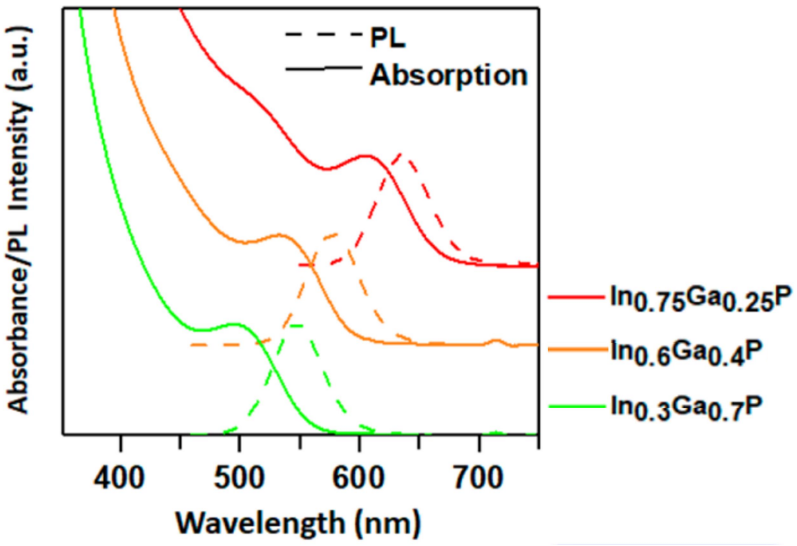

Figure 1.2 Absorption spectra of $In_xGa_{1-x}P$ nanoparticles - *J. Am. Chem. Soc.*, **2018**, 140, 12144.[11]

In addition to using a light harvester, depositing a cocatalyst onto the surface of TiO_2 has been shown to increase activity dramatically. This is partially due to charge separation between the light harvester and the cocatalyst, decreasing electron/hole recombination rates. Tahir found that 5 wt% silver nanoparticles on a TiO_2 support (5 wt% Ag/TiO_2) can reach 1.3 mmol g-cat^{-1} h^{-1} under ultraviolet (UV) light irradiation using a 1:1 CO_2/H_2 flow-rate of 20 mL/min at 373 K.[10] Jia reported that palladium nanoparticles on niobium oxide (Pd/Nb_2O_5), under irradiation from a

300 W xenon lamp, converted CO_2 at a rate of 18.8 mmol g-cat^{-1} h^{-1} using a batch reactor with a 1:1 CO_2/H_2 ratio at a total pressure of 27 psi.[12]

Cocatalysts are typically composed of expensive noble metals such as rhodium and ruthenium, greatly limiting their scalability in an industrial setting.[13,14] Among new cocatalysts that are receiving increasing attention is nickel phosphide (Ni_2P) due to its high photostability, high activity, and low cost.[15] By integrating Ni_2P with CdS nanorods, activity towards the hydrogen evolution reaction (HER) exhibited an increase from 167 to 553 mmol h^{-1} g^{-1} under visible light irradiation by a 300 W xenon lamp ($\lambda > 420$ nm) at ambient/room temperature, using Na_2S (0.75 M) and Na_2SO_3 (1.05 M) as hole scavangers.[16] The 553 mmol h^{-1} g^{-1} rate also surpassed the performance of a similar system that used platinum as the cocatalyst in place of Ni_2P.[16] Ni_2P has also been integrated with titania nanorods, producing 9.38 mmol H_2 h^{-1} g^{-1} via the HER.[17] A recent density functional theory (DFT) study shows evidence that the (0001) crystal plane of Ni_2P evidently favors H_2 dissociation, making it a good candidate for the RWGS reaction.[18] Aside from the DFT study, Ni_2P remains a relatively unexplored photocatalyst for the RWGS reaction.

It is reported that Ni_2P has a low bandgap of 1.0 electron volts (eV),[15,20] making it essentially a conducting material; photo-excited Ni_2P electrons are too short lived to be useful for the RWGS reaction. To enhance the potential for high catalytic activity, indium-gallium phosphides with the general formula $In_xGa_{1-x}P$ can serve as a wide band gap light harvester. These semiconducting nanoparticles can be supported on the TiO_2 along with a Ni_2P cocatalyst, allowing photo-excited electrons in the semiconductor to migrate to an adjacent Ni_2P nanoparticle, as is demonstrated by a schematic of the photocatalyst proposed in this thesis

(Figure 1.3). A more representative sketch of the catalyst is presented in Figure 1.4. A TiO_2 particle would have Ni_2P and $In_xGa_{1-x}P$ particles scattered throughout its pores.

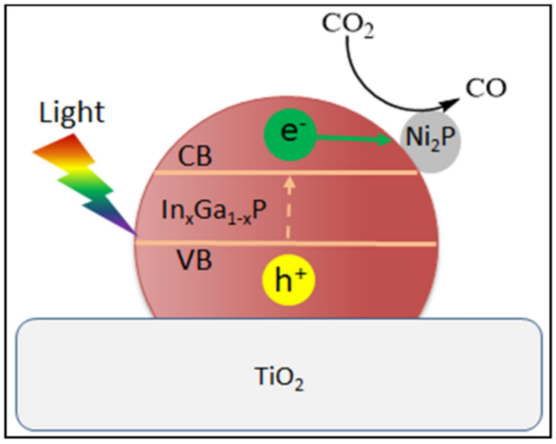

Figure 1.3 Schematic of proposed photocatalyst for RWGS reaction.

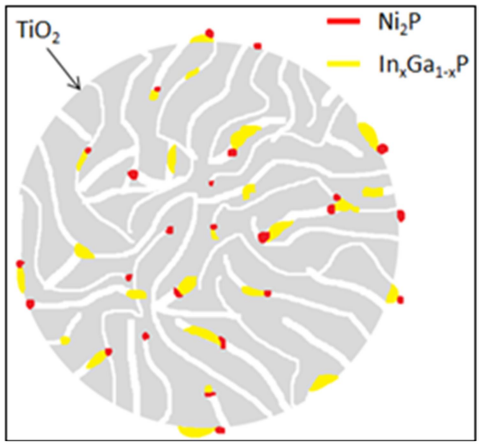

Figure 1.4 A schematic of the proposed photocatalyst, showing TiO_2 porosity.

Once an electron has migrated to the conduction band of Ni_2P, it is relatively far from its corresponding hole, left behind in $In_xGa_{1-x}P$, resulting in a decreased likelihood of a recombination event. The longer-lived excited state increases the probability of the electron being available for a reaction before it has a chance to migrate back to $In_xGa_{1-x}P$ and recombine with its hole. The idea of energy transfer from $In_xGa_{1-x}P$ to Ni_2P is supported by photo-luminescence (PL) data in the literature. PL is the radiative result of photo-excited electrons relaxing down to a lower excited state, resulting in emission of a photon in order to balance the energy loss, conserving absolute energy of the system. Figure 1.5 shows that by loading TiO_2 nanorods with Ni_2P, PL was quenched

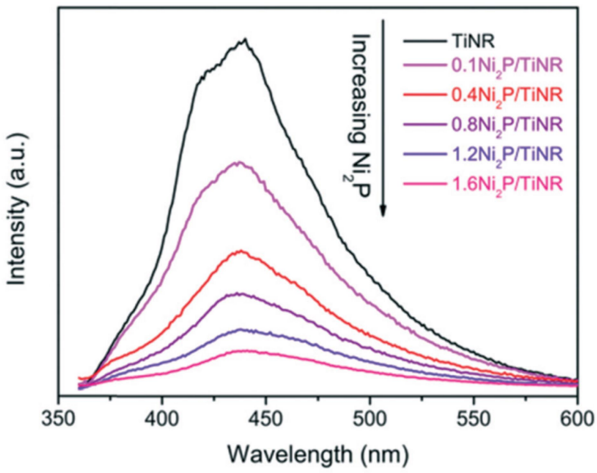

Figure 1.5 Photoluminescence spectra of TiO_2 nanorods (TiNR) with increasing Ni_2P loading.[17]

increasingly as Ni_2P loading was increased.[17] This result indicates charge transfer from TiO_2 to Ni_2P.[17] Figure 1.2, presented earlier, shows $In_xGa_{1-x}P$ nanoparticles absorbing light in the ultraviolet-visible (UV-Vis) range, accompanied by their photoluminescence with maxima in the 550-650 nanometer (nm) range.[11] Given that $In_xGa_{1-x}P$ nanoparticles radiate photoluminescence in the visible and that Ni_2P has been shown to quench visible photo-luminescence via excited state electron transfer, a hypothesis is formed that a heterogeneous system could absorb visible light with $In_xGa_{1-x}P$ nanoparticles, and transfer photoexcited electrons to Ni_2P for use in the RWGS reaction. The electron transfer process is introduced in Figure 1.6 as a band diagram, showing that the conduction band of InP and GaP are both of higher energy than the conduction band of Ni_2P,[15,21,22,23] which is higher in energy than the reduction potential of CO_2 to CO.[24] This work focuses on the synthesis and characterization of a Ni_2P-$In_xGa_{1-x}P/TiO_2$ heterogeneous catalysis system for driving the RWGS reaction.

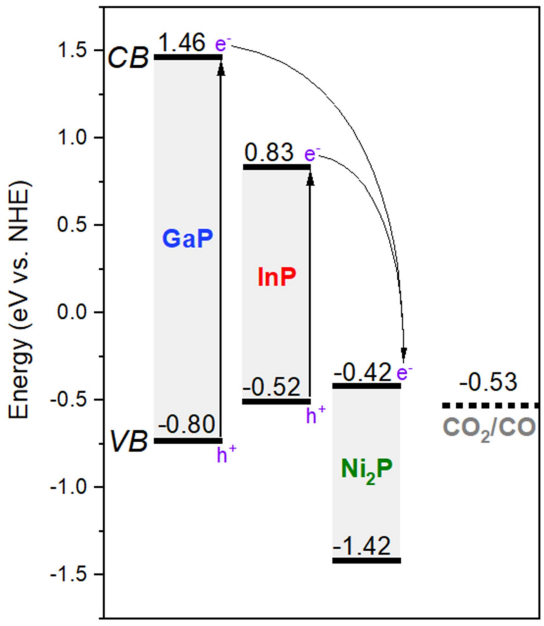

Figure 1.6 Proposed band energy diagram for GaP and InP nanoparticles and Ni_2P cocatalyst compared with CO_2 reduction energy.[15,21,22,23,24]

Despite the expectation that excited electrons in the proposed system will have the required energy to reduce CO_2, the reactants still need to meet a thermal energy requirement necessary to react. Ni_2P has the potential to solve this problem as well. Due to the low band gap of Ni_2P of 1.0 eV,[15,20] absorbed light is expected to primarily produce heat via thermalization and nonradiative relaxation of photoexcited electrons via lattice vibrations (phonons).[13,25] This can result in localized heating of active sites, ultimately transferring thermal energy to reactants. To summarize, the scheme proposed here is that $In_xGa_{1-x}P$ nanoparticles will absorb visible light and transfer excited electrons to Ni_2P active sites. Meanwhile, Ni_2P will absorb light to produce heat from the nonradiative relaxation of photoexcited electrons and it will transfer some of that heat to the $In_xGa_{1-x}P$ creating a photothermal effect, driving the RWGS reaction.

To optimize these semiconductors, band gap tunability is key. A low band gap material can absorb a high number of photons, though too low of a band gap will result in excited electrons with insufficient energy to drive the RWGS reaction. Another key importance to keep in mind when tuning band gaps has to do with the "inverted region effect". Electron transfer (ET) rates typically increase with increasing driving force due to the increasing energy difference between electron donors and acceptors. The inverted region effect predicts that ET rates will decrease once the reorganization energy of the reaction becomes comparable to the difference between acceptor and donor energy levels.[26]

One method for tuning band gaps is to synthesizing nanoparticles at various sizes to induce a quantum confinement effect. Studies suggest that by applying the quantum confinement effect to indium phosphide (InP) and cadmium selenide (CdSe) nanoparticles, band gaps in the 1.4-3.7 eV range for InP and the 1.8-4.9 eV range for CdSe should be achievable by varying nanocrystal radius (1-5 nm).[27] The primary method for tuning the band gap of $In_xGa_{1-x}P$

nanoparticles focused on in this work involves adjusting the indium-gallium (In/Ga) molar ratio of in the nanoparticles. It has been reported (Figure 1.7) that by tuning the In/Ga molar ratio in $In_xGa_{1-x}P$ nanowires, the band gap of the nanowires increased from 1.35 eV to 2.3 eV.[28]

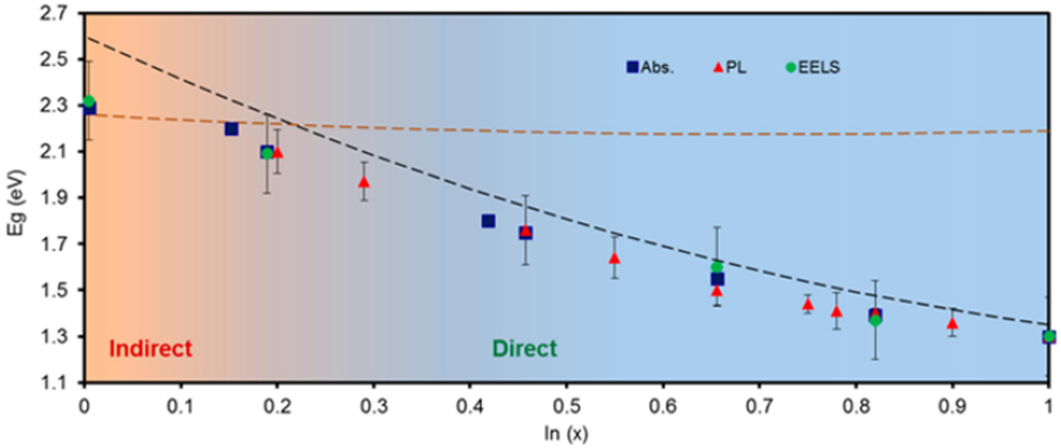

Figure 1.7 Experimental evidence of $In_xGa_{1-x}P$ band gap dependence on indium (In) content (x). Band gaps determined from UV-vis-NIR absorption (blue squares), photo-luminescence (red triangles), and electron energy loss spectroscopy (green rhombuses) measurements were compared. Expected band gaps (E_Γ) are shown in the yellow (indirect) and black (direct) dashed lines, and were calculated using the relation $E_\Gamma(X) = E_\Gamma^A(X) + E_\Gamma^B(1-X) - cX(1-X)$, where c is the bowing parameter (0.2 and 0.65 for indirect and direct band gaps, respectively).[28]

The overarching goal in this thesis project was to apply band gap tunability in photocatalyst-development through the synthesis of TiO_2-supported $In_xGa_{1-x}P$ nanoparticles ($In_xGa_{1-x}P/TiO_2$). Solar energy absorbed by $In_xGa_{1-x}P$ should be able to be transferred to the cocatalyst (Ni_2P) in the form of excited electrons to be utilized to drive the RWGS reaction (schematic presented earlier in Figure 1.3). One major goal here was to develop a method for tuning the band gap of the $In_xGa_{1-x}P$ nanoparticles by synthesizing them on a TiO_2 support at sizes below their ~11 nm Bohr exciton radius in order to induce a quantum confinement effect. Quantum confinement results in larger band gaps as nanoparticle size decreases below the material's Bohr exciton radius. Another major goal was to tune band gap by vary the In/Ga ratio in $In_xGa_{1-x}P$ nanoparticles (also supported on TiO_2).

Chapter 2: Experimental Methods

2.1 Reagents

Silica (Cabot, Cab-O-Sil, EH-5, 380 m^2/g) was calcined before use by heating to 773 K in air for 3 h and titania (Evonik, AEROXIDE, P25, 35-65 m^2/g) was calcined at 673 K in air for 3 h before use. The supports were then stored at 383 K. Metal nitrates were purged with nitrogen gas (N_2) to maintain dry crystals before massing. All other chemicals were used as received.

2.2 Synthesis of Supported Indium-Gallium Phosphides

The titania-supported and silica-supported indium-gallium phosphide catalysts ($In_xGa_{1-x}P/TiO_2$ and $In_xGa_{1-x}P/SiO_2$) were prepared with x values ranging between 0 and 1. This was done by varying the molar ratio of indium (III) nitrate ($In(NO_3)_3 \cdot yH_2O$, Aldrich, 99.9% trace metals basis) and gallium (III) nitrate ($Ga(NO_3)_3 \cdot zH_2O$, Alfa Aesar, 99.9% metals basis) used in the precursor synthesis. Hypophosphorous acid (H_3PO_2, Sigma-Aldrich, 50 wt. % in H_2O) was used as the phosphorous source, and nominal phosphorous to metal molar ratios (P/M, M = In + Ga) of ~1.25 on TiO_2, and 1.0 on SiO_2 were used in the synthesis of $In_xGa_{1-x}P$ catalysts unless otherwise stated.

The metal nitrate starting materials were dissolved in ~10 mL nanopure water and this solution was impregnated onto the support (either SiO_2 or TiO_2)until incipient wetness was achieved. Incipient wetness is reached by adding a solution to the support drop-wise until the first sign of homogenous wetness is observed, indicating that the pores of the support material are filled. The impregnated support was then dried at 383 K for at least 2 h and crushed until powdered using a mortar and pestle. The impregnation process was repeated until the solution was completely added to the support, using a minimal amount of nanopure H_2O as a rinse for the

final impregnation. This resulted in supported metal nitrates, which were then calcined at 673 K for 3 h (unless stated otherwise) to yield supported metal oxide precursors ($In_xGa_{2-x}O_3/SiO_2$ or $In_xGa_{2-x}O_3/TiO_2$). The resulting $In_xGa_{2-x}O_3/SiO_2$ catalyst was then impregnated to incipient wetness with ~2 mL of an aqueous solution of H_3PO_2 followed by drying for at least 3 h (at 343 K, to avoid H_3PO_2 decomposition at higher temperatures). Once in powdered form, ~0.5 g of the H_3PO_2-$In_xGa_{1-x}P$/(support) material was placed on a bed of quartz wool at the bottom of a U-tube, which was then subjected to temperature programmed reduction (TPR). Synthesis of indium-gallium phosphides is summarized in Scheme 2.1, using SiO_2 as an example support.

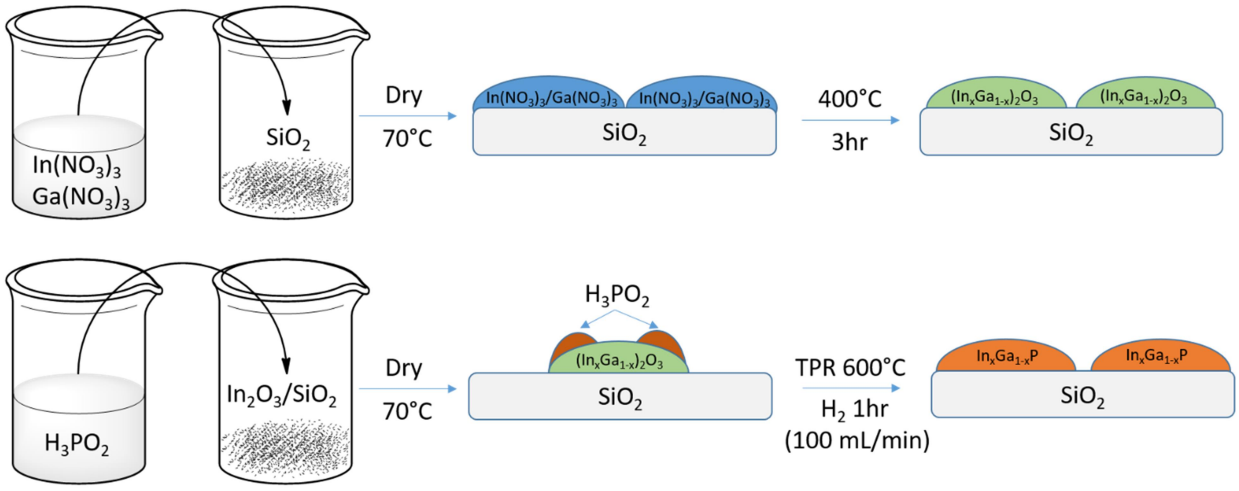

Scheme 2.1 Synthesis of silica-supported metal phosphide photocatalysts.

The TPR setup is shown in Figure 2.2.1. Prior to the reduction step, the oxide precursor catalyst was purged with flowing He at 60 mL/min for 30 min. H_2 gas was

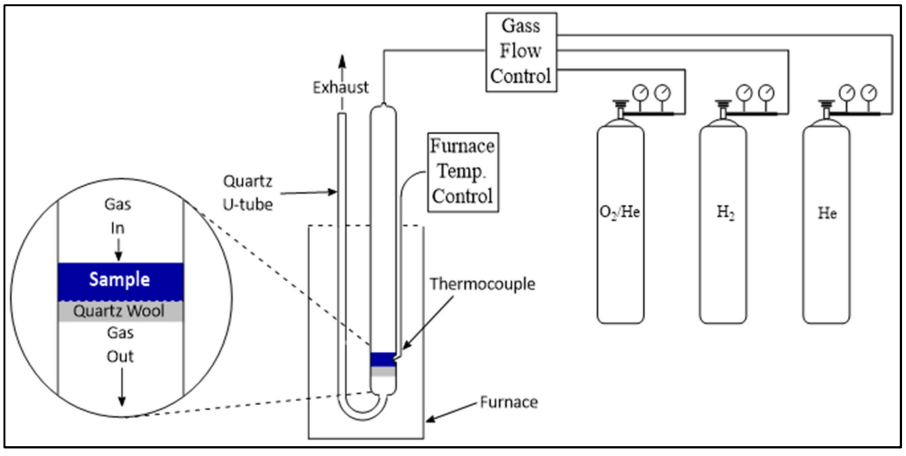

Figure 2.2.1 Diagram of TPR gas flow and furnace setup for sample reduction in a quartz U-tube.

then passed through the oxide precursor at 100 mL/min while the temperature was increased at a ramp rate of 5 K/min to a final temperature of 873 K, which was held for 1 h in order to completely reduce the precursors to their corresponding indium-gallium phosphides ($In_xGa_{1-x}P/SiO_2$ or $In_xGa_{1-x}P/TiO_2$). Once the $In_xGa_{1-x}P$/(support) catalyst was cooled to below 343 K, the U-tube was purged with He at 60 mL/min for 30 min to remove H_2, in preparation for the passivation step. Passivation consisted of flowing 1.001 mol% O_2/He through the catalyst at 60 mL/min for 2 h, slowly forming an oxidized layer on the surface of the $In_xGa_{1-x}P$ particles. Passivation prevents a deeply penetrating, rapid oxidation event upon direct exposure to the high concentration of O_2 in the air atmosphere (~21% O_2). The temperature program used is plotted in Figure 2.2.2.

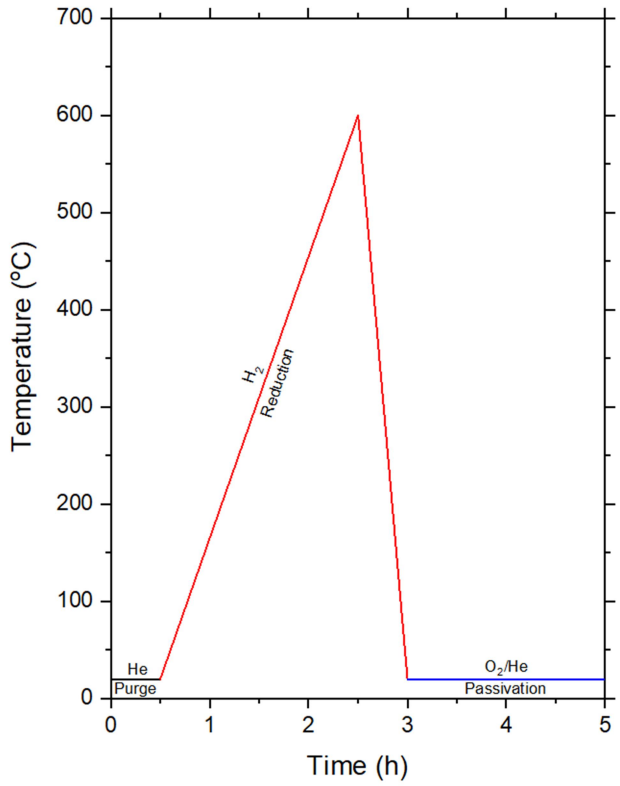

Figure 2.2.2 Graphical representation of the temperature program used for the conversion of the $In_xGa_{2-x}O_2$/support precursor to the final $In_xGa_{1-x}P$/support product.

Reactant quantities used in the $In_xGa_{2-x}O_3/SiO_2$ syntheses, the precursors for the 20 wt% $In_xGa_{1-x}P/SiO_2$ catalysts, are listed in Table 2.2.1.

Table 2.2.1 Reagent masses used in the $In_xGa_{2-x}O_3/SiO_2$ syntheses, the precursors for the 20 wt% $In_xGa_{1-x}P/SiO_2$ catalysts.

Target Composition	SiO_2 (g)	$In(NO_3)_3 \cdot 4.2H_2O$ (g)	$Ga(NO_3)_3 \cdot 0.1H_2O$ (g)
Ga_2O_3/SiO_2	3.00	---	1.9193
$In_{0.5}Ga_{1.5}O_3/SiO_2$	3.0003	0.6308	1.2940
$InGaO_3/SiO_2$	3.00	1.1460	0.7842
$In_{1.5}Ga_{0.5}O_3/SiO_2$	3.0005	1.5738	0.3594
In_2O_3/SiO_2	0.9586	0.6452	---

The 20 wt% $In_xGa_{1-x}P/SiO_2$ catalysts were synthesized by first massing exactly one third of the $In_xGa_{2-x}O_3/SiO_2$ precursor and impregnating it with an aqueous solution of 50 wt% H_3PO_2. Due to the fact that the record of these $In_xGa_{2-x}O_3/SiO_2$ masses have been lost, they have been calculated based on the masses of SiO_2, $In(NO_3)_3 \cdot 4.2H_2O$, and $Ga(NO_3)_3 \cdot 0.1H_2O$ listed in Table 2.2.1. The masses used in the syntheses of the 20 wt% $In_xGa_{1-x}P/SiO_2$ catalysts are presented in Table 2.2.2.

Table 2.2.2 Masses used in the syntheses of 20 wt% $In_xGa_{1-x}P/SiO_2$ catalysts (P/M=1).

Target Composition	$In_xGa_{2-x}O_3/SiO_2$ (g)	50 wt% H_3PO_2 (g)
GaP/SiO_2	1.2328	0.3281
$In_{0.25}Ga_{0.75}P/SiO_2$	1.2346	0.2950
$In_{0.5}Ga_{0.5}P/SiO_2$	1.2360	0.2678
$In_{0.75}Ga_{0.25}P/SiO_2$	1.2372	0.2453
InP/SiO_2*	1.1965	0.2262

*All of the In_2O_3/SiO_2 precursor (1.1965 g) was used in the synthesis of 20 wt% InP/SiO_2.

Reactant quantities used in the In_2O_3/SiO_2 syntheses, the precursors for the 5-20 wt% $In_xGa_{1-x}P/SiO_2$ catalysts, are listed in Table 2.2.3.

Table 2.2.3 Reagent masses used in the In_2O_3/SiO_2 syntheses, the precursors for 5-20 wt% InP/SiO_2.

Target InP Loading	SiO_2 (g)	$In(NO_3)_3 \cdot 4.2H_2O$ (g)
5 wt%	1.0010	0.1357
10 wt%	1.0115	0.2875
15 wt%	1.0094	0.4570
20 wt%	0.9586	0.6452

The 5-20 wt% InP/SiO_2 catalysts were synthesized by first impregnating the In_2O_3/SiO_2 precursor it with an aqueous solution of 50 wt% H_3PO_2. Due to the fact that the record of these In_2O_3/SiO_2 masses have been lost, they have been calculated based on the masses of SiO_2 and $In(NO_3)_3 \cdot 4.2H_2O$ listed in Table 2.2.3. The masses used in the syntheses of the 5-20 wt% InP/SiO_2 catalysts are presented in Table 2.2.4.

Table 2.2.4 Masses used in the syntheses of the 5-20 wt% InP/SiO_2 catalysts (P/M=1).

InP Loading	In_2O_3/SiO_2 (g)	50 wt% H_3PO_2 (g)
5 wt%	1.0510	0.0473
10 wt%	1.1175	0.1003
15 wt%	1.1779	0.1603
20 wt%*	1.1965	0.2262

*All of the In_2O_3/SiO_2 precursor (1.1965 g) was used in the synthesis of 20 wt% InP/SiO_2.

Reactant quantities used in the $In_xGa_{2-x}O_3/TiO_2$ syntheses, the precursors for the 20 wt% $In_xGa_{1-x}P/TiO_2$ catalysts, are listed in Table 2.2.5.

Table 2.2.5 Reagent masses used in the $In_xGa_{2-x}O_3/TiO_2$ syntheses, the precursors for the 20 wt% $In_xGa_{1-x}P/TiO_2$ catalysts.

Target Composition	**TiO_2 (g)**	**$In(NO_3)_3 \cdot zH_2O$ (g)***	**$Ga(NO_3)_3 \cdot 0.1H_2O$ (g)**
GaP/TiO_2	3.002	---	1.917
$In_{0.25}Ga_{0.75}P/TiO_2$	3.005	0.540	1.295
$In_{0.5}Ga_{0.5}P/TiO_2$	3.006	0.981	0.785
$In_{0.75}Ga_{0.25}P/TiO_2$	3.006	1.348	0.359
InP/TiO_2	1.000	0.6178	---

*z $\approx$ 3.3 in $In(NO_3)_3 \cdot zH_2O$ for the InP/TiO_2 synthesis and 1.9 for the remaining syntheses.

The 20 wt% $In_xGa_{1-x}P/TiO_2$ catalysts were synthesized by first massing exactly half of the $In_xGa_{2-x}O_3/TiO_2$ precursor and impregnating it with an aqueous solution of 50 wt% H_3PO_2. Due to the fact that the record of these $In_xGa_{2-x}O_3/TiO_2$ masses have been lost, they have been calculated based on the masses of TiO_2, $In(NO_3)_3 \cdot zH_2O$, and $Ga(NO_3)_3 \cdot 0.1H_2O$ listed in Table 2.2.5. The masses used in the syntheses of the 20 wt% $In_xGa_{1-x}P/TiO_2$ catalysts are presented in Table 2.2.6.

Table 2.2.6 Masses used in the syntheses of the 20 wt% $In_xGa_{1-x}P/TiO_2$ catalysts (P/M ~1.25).

Composition	**$In_xGa_{1-x}P/TiO_2$ (g)**	**50 wt% H_3PO_2 (g)**
GaP/TiO_2	1.8498	0.6155
$In_{0.25}Ga_{0.75}/TiO_2$	1.8499	0.5533
$In_{0.5}Ga_{0.5}P/TiO_2$	1.8489	0.5040
$In_{0.75}Ga_{0.25}P/TiO_2$	1.8474	0.4599
InP/TiO_2	0.6189	0.1421

Reactant quantities used in the In_2O_3/TiO_2 syntheses, the precursors for the 5-20 wt% $In_xGa_{1-x}P/SiO_2$ catalysts, are listed in Table 2.2.7.

Table 2.2.7 Reagent masses used in the syntheses of In_2O_3/TiO_2, the precursors for the 1-20 wt% InP/TiO_2 catalysts.

Target InP Loading	TiO_2 (g)	$In(NO_3)_3 \cdot zH_2O$ (g)*
1 wt%	1.999	0.051
2.5 wt%	1.999	0.133
5 wt%	2.000	0.2774
10 wt%	1.994	0.582
15 wt%	2.00	0.926
20 wt%	1.00	0.617

*$z \approx 3.3$ in the 20 wt% InP synthesis and 4.5 for remaining syntheses.

The 5-20 wt% InP/TiO_2 catalysts were synthesized by first impregnating exactly half of the In_2O_3/TiO_2 precursor it with an aqueous solution of 50 wt% H_3PO_2. Due to the fact that the record of these In_2O_3/TiO_2 masses have been lost, they have been calculated based on the masses of TiO_2 and $In(NO_3)_3 \cdot zH_2O$ listed in Table 2.2.7. The masses used in the syntheses of the 5-20 wt% InP/TiO_2 catalysts are presented in Table 2.2.8.

Table 2.2.8 Masses used in the syntheses of InP/TiO_2 catalysts (P/M ~1.25).

InP Loading	In_2O_3/TiO_2 (g)	50 wt% H_3PO_2 (g)
1 wt%	1.0087	0.0110
2.5 wt%	1.0236	0.0299
5 wt%	1.0503	0.0599
10 wt%	1.1025	0.1249
15 wt%*	0.8918	0.1519
20 wt%	0.6189	0.1421

*38.16% of the In_2O_3/TiO_2 precursor (0.8918 g) was used in this InP/TiO_2 synthesis.

2.3 Synthesis of Supported Nickel Phosphide

Titania-supported nickel phosphide catalysts (Ni_2P/TiO_2) were prepared using a nominal P/Ni ratio of 2.0. The nickel source was nickel (II) hydroxide ($Ni(OH)_2$, Alfa Aesar, Ni 61%) and the phosphorous source was 50 wt% H_3PO_2(aq). An aqueous solution of nickel hypophosphite ($Ni(H_2PO_2)_2$ was prepared by dissolving nickel hydroxide in H_3PO_2(aq), slowly adding a total of ~10 mL nanopure H_2O over the course of 1-3 days while stirring and heating at 343 K. The solution of $Ni(H_2PO_2)_2$(aq) was then used to impregnate 2.0 or 3.0 g of TiO_2. The remainder of the synthesis involves a TPR sequence similar to what was presented in Figure 2.2.2, using a reduction temperature of 673 K. The formation of $Ni(H_2PO_2)_2$ is described in Equation 2.1.

$$Ni(OH)_2(s) + 2H_3PO_2(aq) \rightarrow Ni(H_2PO_2)_2(aq) + 2H_2O(l) \qquad \textbf{2.1}$$

All reactant quantities used in the Ni_2P/TiO_2 syntheses are listed in Table 2.3.

Table 2.3 Reagent masses used in the syntheses of Ni_2P/TiO_2 catalysts (P/M=2).

Wt% Ni_2P	**TiO_2**	**$Ni(OH)_2$ (g)**	**50 wt% H_3PO_2 (g)**
1	3.00	0.0372	0.1071
2.5	2.00	0.0713	0.1825
5	2.00	0.1319	0.3750
10	2.00	0.2789	0.7923
15	2.01	0.4429	1.2565
20	3.00	0.9403	2.6660

The Ni_2P-InP/TiO_2 catalyst (20 wt% Ni_2P, 10 wt% InP) was prepared by impregnating 0.4832 g of 10 wt% InP to incipient wetness with a solution of $Ni(H_2PO_2)_2$ made by mixing 0.1519 g $Ni(OH)_2$ and 0.4295 g 50 wt% H_3PO_2 solution. The of $Ni(H_2PO_2)_2$-InP/TiO_2 sample was then reduced as described by a similar temperature program to what was plotted in Figure 2.2.2, using a reduction temperature of 673 K.

2.4 X-ray Diffraction

X-ray diffraction (XRD) patterns for SiO_2-supported catalysts were obtained using a PanAnalytical X'Pert MRD Pro diffractometer with a Cu K_α radiation source having a wavelength (λ) of 0.15406 nm. Samples of catalysts in powdered form were deposited onto a glass slide by wetting with methanol and allowing to air dry. The catalysts were then analyzed over a Bragg angle (2θ) range of 20-80°, using a step size of 0.02° and a dwell time of 5.2 s. Reference patterns were taken from the Crystallography Open Database (COD).[29]

XRD patterns for TiO_2-supported catalysts were obtained using a Rigaku MiniFlex 6G diffractometer with a Cu K_α radiation source with $\lambda = 0.15406$ nm. Catalysts were mounted on zero-background sample holders (Rigaku, 5mm x 0.2 mm Well, Si510) in powdered form and scanned over Bragg angles of 20-80° using a step size of 0.0025° and a dwell time of 0.3 s.

Crystal phase identification was carried out by comparison of the as collected XRD patterns and reference XRD patterns from the Crystallography Open Database (COD).[29] It was noted that, once subjected to TPR, XRD peaks associated with rutile TiO_2 grew in intensity relative to the anatase peaks, indicating an increase in the rutile:anatase ratio of the TiO_2. Average crystallite sizes (D_c) were determined using the "phase identification" and "configure size and strain" options in SmartLab Studio II software, neglecting XRD peaks significantly obstructed by signals from other crystalline phases such as rutile and anatase TiO_2. The method used in SmartLab Studio II for calculating crystallite sizes is the Halder-Wagner's method.[30]

2.5 Energy Dispersive X-ray Spectroscopy

Catalyst composition was probed by energy dispersive x-ray spectroscopy (EDS) with an Oxford X-Max energy dispersive x-ray spectroscopy (EDS) detector on either a Tescan Vega 3 Thermionic scanning electron microscope (SEM) or a JEOL JSM-7200F Field Emission SEM

using take-off angles of 35.0° and 29.0°, respectively. Powdered catalysts were affixed onto aluminum mounting tabs using carbon tape and analyzed with accelerating voltages of either 5 or 15 kV. EDS spectra were taken for 100-200 s and analyzed using Aztec 3.3 SP1 software (Oxford Instruments).

2.6 Ultraviolet-Visible-Near Infrared Spectroscopy

UV-Vis-NIR absorption spectra were acquired using a Jasco V-670 UV/Vis spectrometer equipped with a 60 mm diffuse reflectance integrating sphere. Catalysts were mounted in a powder sample cell (Jasco, PSH-002, 16 x 6 mm) and scans were taken from 300 to 1350 nm using a scanning speed of 200 nm/min, and bandwidths of 5.0 nm and 20.0 nm for UV/Vis and NIR regions, respectively. The raw data had a discontinuity at 750 nm, an artifact of an imperfect grating switch. To correct for this, the absorbance values associated with each point below 750 nm were increased until a smooth spectrum was obtained. This data manipulation did not affect the band gap analyses, for any shift in the y direction does not change the x intercept of the extrapolated lines and the data point range used for the extrapolations did not include 750 nm.

Band gap determination consisted of first plotting $(F(R)*h\nu)^{1/2}$, a function of reflectance (R), against photon energy (eV) for calculating a direct band gap, or plotting $F(R)*h\nu^2$ against (eV) for calculating an indirect band gap, as described by López and Gómez,[31] where $F(R) = \frac{(1-R)^2}{2R}$. Next, two lines were extrapolated; one through the most linear section of the absorption edge and one through the lowest, flattest section of the baseline. The x-coordinate of the intersection of these two lines is deemed to be the band gap of these materials. The most linear section of the absorption edge was located by plotting the derivative of the Tauc plot and pinpointing the maximum point in the range associated with the absorption edge. Using the TiO_2 support as an example, Figure 2.6 shows the resulting line extrapolation. The TiO_2 support

material consists of TiO_2 in two phases, rutile and anatase, both of which are identified on page __. It is reported that these phases have band gaps of 3.03 and 3.20 eV,[32] respectively, and the Tauc plot in Figure 2.6 shows the extrapolation of two lines, which leads to experimental determination of two band gaps in TiO_2: 3.04 and 3.12 eV, assigned to rutile and anatase, respectively. Figure A.1 in the appendix shows the Tauc plot of TiO_2 and its derivative superimposed, the range bars indicating the approximate range of data points used to extrapolate the two lines in Figure 2.6. These data points were chosen because they are near the maxima in the derivative, which corresponds to the most linear section of the Tauc plot.

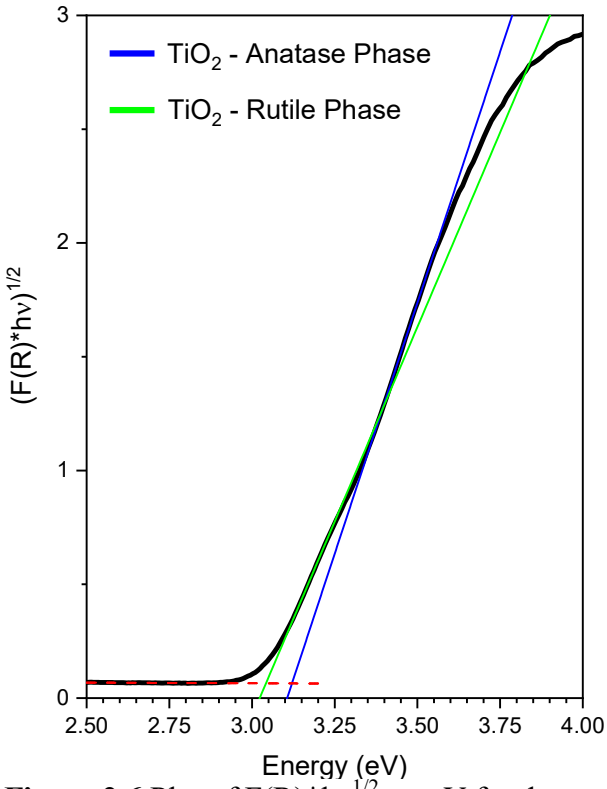

Figure 2.6 Plot of $F(R)*h\nu^{1/2}$ vs. eV for determining band gaps in the TiO_2 support material.

2.7 X-Ray Photoelectron Spectroscopy

X-ray photoelectron spectroscopy (XPS) spectra were collected using a Surface Physics M-Probe ESCA X-Ray Photoelectron Spectrometer equipped with a flood gun, a monochromatic Al K_α x-ray source (1486.6 eV), and a hemispherical analyzer with microchannel plate detectors. The take-off angle was 55°, which results in a sampling depth of 3-10 nm. The vacuum system includes a cryogenic pump and two turbo pumps, allowing all catalysts to be scanned at pressures below $5x10^{-7}$ Torr. The spectra were corrected for sample charging by using the C(1s) peak as a reference (284.6 eV) and they were fitted for analysis with CasaXPS software using a Shirley type background.

Chapter 3: Results

3.1 XRD Characterization of $In_xGa_{x-1}P/SiO_2$ Catalysts

X-ray diffraction was used to determine crystalline phases in the InP/SiO_2 catalysts. Crystal phase identification was done by comparing experimental XRD patterns with an InP reference pattern (Card No. 9008852) found in the COD (Crystallography Open Database) database.[29] For clarity while interpreting XRD plots, Figure 3.1.1 shows the layout that is used in each XRD section. The format has reference XRD patterns situated at the top of the graph, diffraction patterns for the catalysts below, and a scan of the support material (SiO_2 or TiO_2) at the bottom.

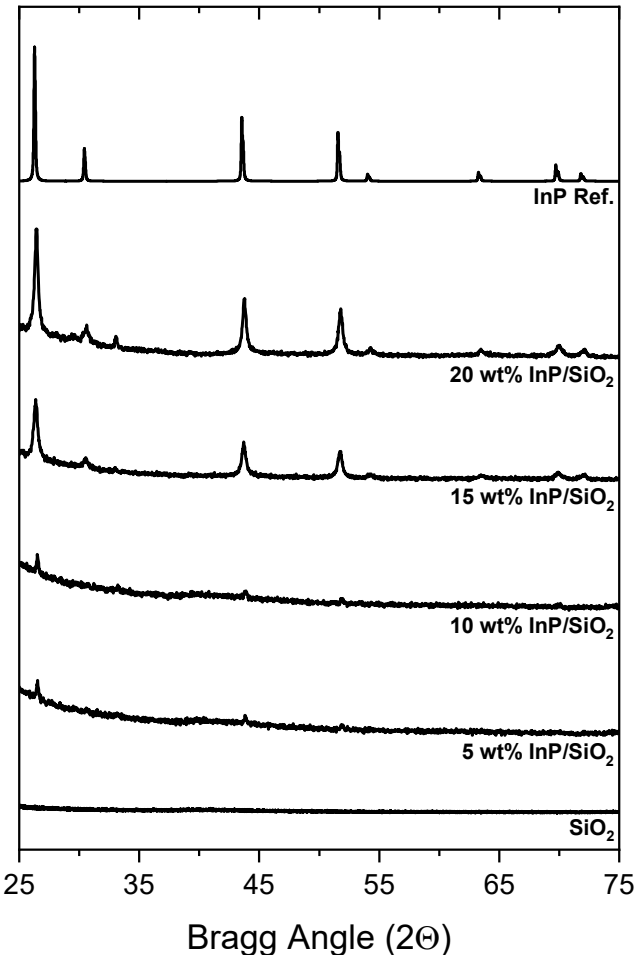

Figure 3.1.1 XRD patterns of InP/SiO_2 catalysts (5-20 wt%).

Figure 3.1.1 compares diffraction patterns of InP/SiO_2 catalysts with a range of InP loadings (5-20 wt%); the observed diffraction peaks are in agreement with the InP reference pattern. The most intense peaks at Bragg angles of 26.5°, 43.8°, and 51.8°, attributed to the (111), (220), and (311) InP crystalline planes, respectively, are observed for all InP loadings presented. These three peaks are shown to increase in intensity as InP loading increases from 5 to 20 wt% InP.

Figure 3.1.2 shows a stacked plot of diffraction patterns for $In_xGa_{1-x}P/SiO_2$ catalysts having different compositions (In/Ga molar ratio). The three InP peaks mentioned above are observed when the gallium content is below that of the $In_{0.25}Ga_{0.75}P/SiO_2$ catalyst. The (111) peak position of InP in the InP/SiO_2 catalyst appears at a Bragg angle of 26.4°. This peak shows at a higher Bragg angle (26.9°) in the $In_{0.5}Ga_{0.5}P/SiO_2$ pattern, which is less of a shift than predicted by Vegard's law (27.6°, the average of the expected (111) peak positions for InP and GaP). As gallium content is increased in these catalysts the InP peak decreases in intensity and is replaced by very broad peaks, indicative of an amorphous material.

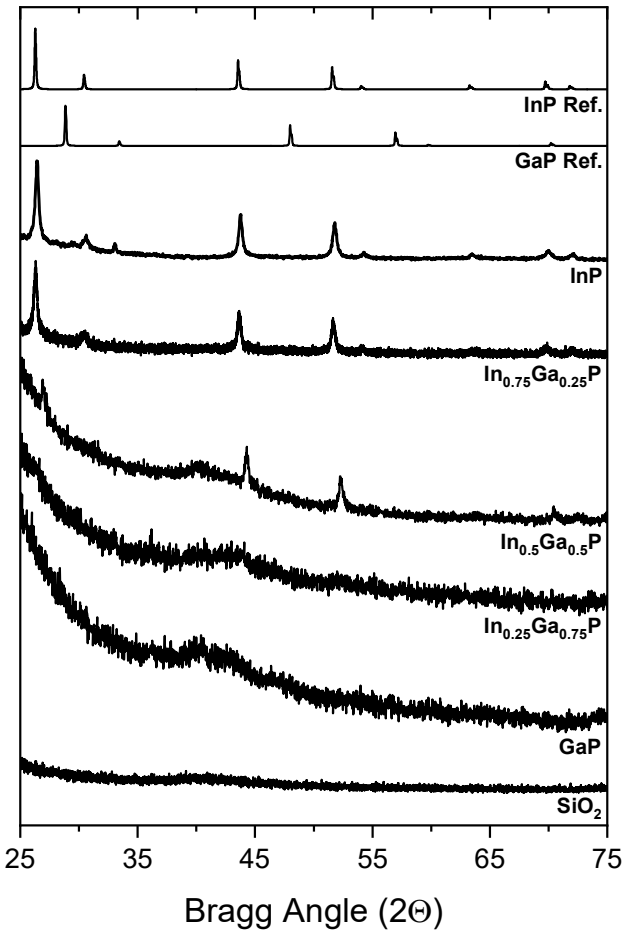

Figure 3.1.2 XRD patterns of 20 wt% $In_xGa_{1-x}P/SiO_2$ catalysts

3.2 Characterization of $In_xGa_{2-x}O_3/TiO_2$ Catalysts

3.2.1 XRD

The XRD patterns in the following plots include the diffraction pattern of the TiO_2 support material at the bottom of each stacked plot. The as-received TiO_2 material is composed of anatase and rutile crystal phases (with an anatase/rutile ratio of 80/20) and its diffraction pattern shows peaks characteristic of anatase (COD Card No. 9015929) and rutile (COD Card No. 90156662).[33] The most intense peaks from anatase are observed at 25.4°, 37.9°, and 48.1° (assigned to the (101), (004), and (200) crystal planes, respectively) and for rutile at 27.5°, 36.1°, and 54.4° (assigned to the (110), (101), and (211) crystal planes, respectively).

Figure 3.2.1 shows XRD patterns for the In_2O_3/TiO_2 catalysts. Crystal phase identification was done by comparing experimental XRD patterns with an In_2O_3 reference pattern found in the COD database (Card No. 1010341). At loadings of 10 wt% In_2O_3 and higher, the most intense diffraction peaks are observed at 30.6°, 35.5°, and 50.3°, which can be indexed to the (222), (400), and (440) crystal planes, respectively, of the cubic phase of In_2O_3 (COD Card No. 1010341). The hexagonal crystal phase of In_2O_3 is also identified, most noticeably by the (110) and (211) diffraction peaks at 32.6° and 51.0°, respectively. The only observed In_2O_3 diffraction peak in the 5 wt% In_2O_3 catalyst is the (222) peak at 30.6°. No In_2O_3 peaks are observed for the 2.5 wt% In_2O_3 catalyst.

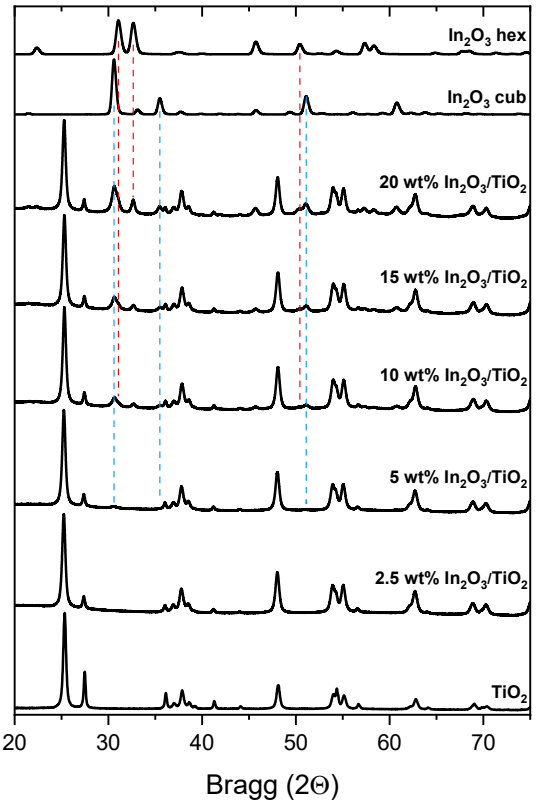

Figure 3.2.1 XRD patterns of In_2O_3/TiO_2 catalysts (2.5-20 wt%).

The In_2O_3/TiO_2 catalysts were analyzed for average crystallite size determination. The (111), (200), (220), (311), and (420) peaks were manually selected for this analysis due to lack of interference from TiO_2 peaks. The average In_2O_3 crystallite sizes can be found in Table 3.2.1.Catalysts with loadings of 2.5 and 5 wt% were not analyzed due to low signal to noise ratios. Based on the crystallite sizes listed in Table 3.2.1, average In_2O_3 crystallite size shows little dependence on loading.

Table 3.2.1 Average crystallite sizes for In_2O_3/TiO_2 catalysts.

Wt%	Crystallite Size (nm)
5	---
2.5	---
10	14
15	12
20	16

Figure 3.2.2 displays a stacked plot of XRD patterns for the $In_xGa_{2-x}O_3/TiO_2$ catalysts, and it reveals the (222), (400), and (440) diffraction peaks of In_2O_3 in its cubic crystal phase at 30.6°, 35.5°, and 50.3°, respectively, and the (110) and (211) peaks of its hexagonal phase at 32.6° and 51.0°, respectively, in the three most indium rich $In_xGa_{2-x}O_3/TiO_2$ catalysts. These peaks are most intense for the In_2O_3/TiO_2 catalyst. As indium content is decreased, the diffraction peaks assigned to the In_2O_3 phase diminish. For the two most gallium rich catalysts, only peaks belonging to TiO_2 are observed. Therefore, there is no XRD evidence for the presence of $In_xGa_{2-x}O_3$ crystals in these two catalysts.

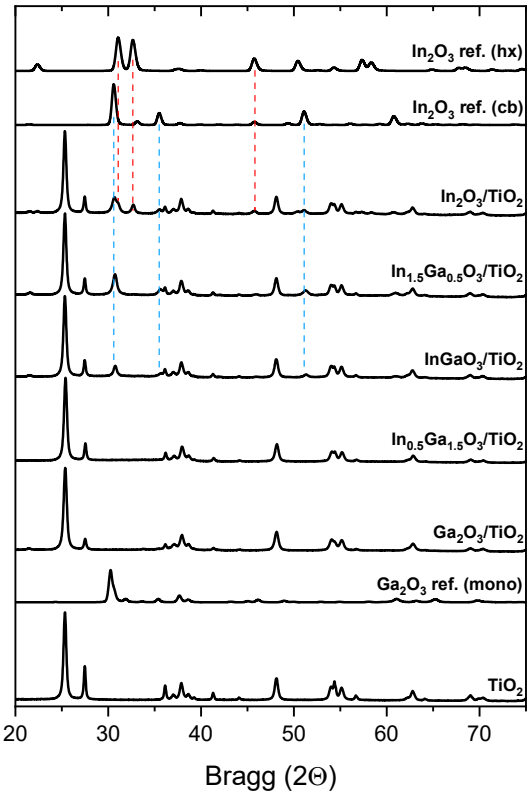

Figure 3.2.2 XRD patterns of 20 wt% $In_xGa_{2-x}O_3/ TiO_2$ catalysts.

The average $In_xGa_{2-x}O_3$ crystallite sizes for the $In_xGa_{2-x}O_3/TiO_2$ catalysts are presented in Table 3.2.2, and it reveals that, within uncertainty, crystallites grow to similar sizes as gallium content is varied.

Table 3.2.2 Average crystallite sizes for 20 wt% $In_xGa_{2-x}O_3/TiO_2$ catalysts.

Catalyst	Crystallite Size (nm)
Ga_2O_3	---
$In_{0.5}Ga_{1.5}O_3/TiO_2$	---
$InGaO_3/TiO_2$	16
$In_{1.5}Ga_{0.5}O_3/TiO_2$	13
In_2O_3/TiO_2	16

3.2.2 EDS and SEM

EDS analysis was done on the In_2O_3/TiO_2 catalysts (oxide precursors of InP/TiO_2) prepared using the incipient wetness technique and calcination at 673 K. The EDS spectra in Figure 3.2.3 show that the L_α, $L_{\beta1}$, $L_{\beta2}$, and L_γ spectral lines of indium, observed at energies of 3.3, 3.5, 3.7, and 3.9 keV, respectively, are detectable at least down to a 2.5 wt% loading of In_2O_3 and that when loading is increased to 20 wt%, a corresponding increase in indium signal intensity is observed.

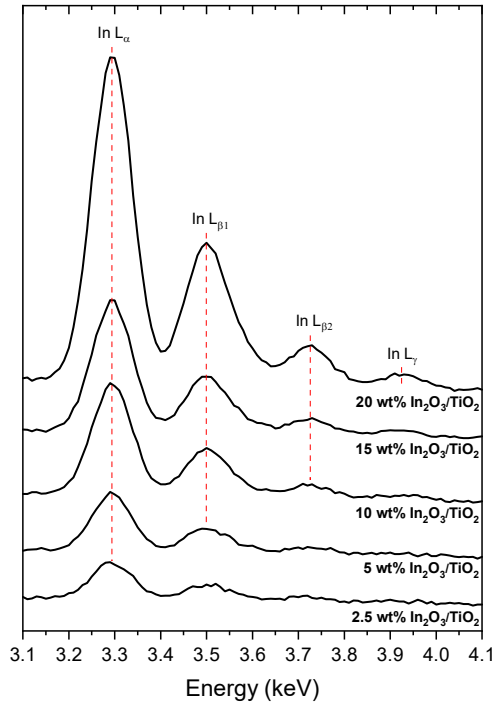

Figure 3.2.3 EDS spectra for In_2O_3/TiO_2 catalysts (2.5-20 wt%).

Figure 3.2.4 shows EDS spectra that correspond to two point-scans of a 20 wt% In_2O_3/TiO_2 catalyst. The locations of these EDS point-scans are indicated with red squares in the SEM image in the background of Figure 3.2.4. The particles seen in the top-right section of this image resemble the shape of grains of rice, though a few of the particles are oriented in such a way as to reveal a shape more accurately described as a disk. Length measurements were taken of the diameter and thickness of these particles, revealing averages of 110 and 28 nm, respectively. Also, an EDS point scan of one of the particles was taken (Spectrum 37) and compared to a point scan from an area that shows no evidence of these particles (Spectrum 36).

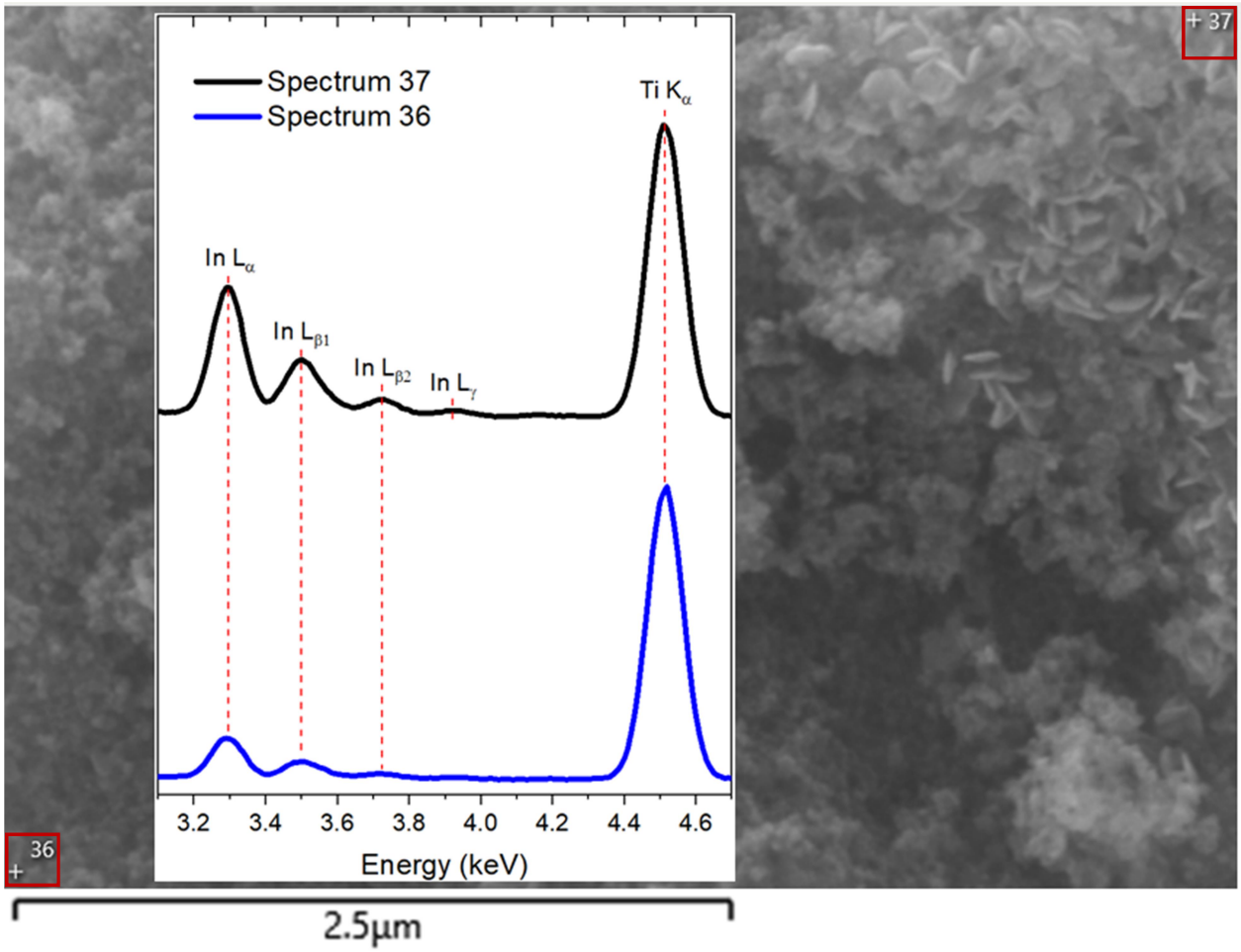

Figure 3.2.4 SEM image and EDS spectra of two point scans of a 20 wt% In_2O_3/TiO_2 catalyst.

The $In_xGa_{2-x}O_3/TiO_2$ catalysts (precursors of $In_xGa_{1-x}P/TiO_2$) prepared using the incipient wetness technique and calcination at 673 K were also subjected to EDS analysis. Elemental compositions were determined using the L_α peak of gallium at a ~1.1 keV binding energy and the L peaks of indium at binding energies of 3.3, 3.5, and 3.7 keV. The EDS spectra can be seen in Figure 3.2.5, and reveals that as the indium content (x) is varied from 1 to 0, the In L peaks diminish and the Ga L_α peak grows in.

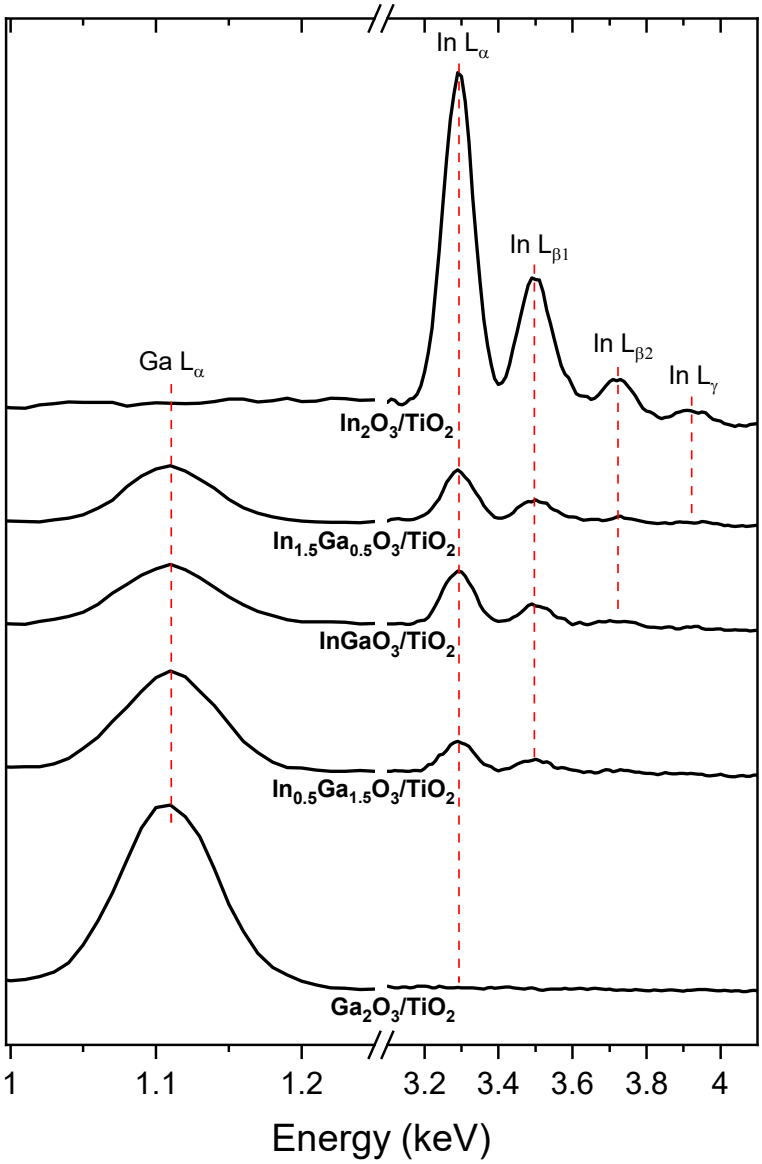

Figure 3.2.5 EDS spectra for 20 wt% $In_xGa_{2-x}O_3/TiO_2$ catalysts.

Elemental compositions of the $In_xGa_{2-x}O_3/TiO_2$ catalysts can be viewed in Table 3.2.3 along with the indium-to-gallium molar ratios (In/Ga). EDS determined In/Ga values range from being ~67% to ~230% the expected values (3.0 and 0.33 in the catalysts with target compositions of $In_{1.5}Ga_{0.5}O_3$ and $In_{0.5}Ga_{0.15}O_3$, respectively). The reason for the discrepancies in these bulk compositions is unclear, though one possible explanation stems from the uncertainty in the metal nitrate precursor hydrate numbers (y in $(In(NO_3)_3 \bullet yH_2O$ and z in $Ga(NO_3)_3 \cdot zH_2O$).

Table 3.2.3 Compositions of the 20 wt% $In_xGa_{2-x}O_3/TiO_2$ catalysts as determined by EDS.

Target Bulk Composition	Formula (EDS)	In/Ga (EDS)
Ga_2O_3	$Ga_2O_{3.00}$	0
$In_{0.5}Ga_{1.5}O_3$	$In_{0.87\pm0.02}Ga_{1.1\pm0.02}O_{3.00}$	0.77
$InGaO_3$	$In_{1.40\pm0.02}Ga_{0.60\pm0.02}O_{3.00}$	2.1
$In_{1.5}Ga_{0.5}O_3$	$In_{1.32\pm0.05}Ga_{0.68\pm0.05}O_{3.00}$	2.0
In_2O_3	$In_2O_{3.00}$	---

3.2.3 UV-Vis-NIR Spectroscopy

UV-Vis absorption spectra of a series of In_2O_3/TiO_2 catalysts are shown in Figure 3.2.6. The spectra of catalysts with loadings higher than 5 wt% In_2O_3 show a broad absorbance below 600 nm, consistent with what was reported in the literature.[34] This broad absorbance increases in relative intensity with increasing In_2O_3 loading.

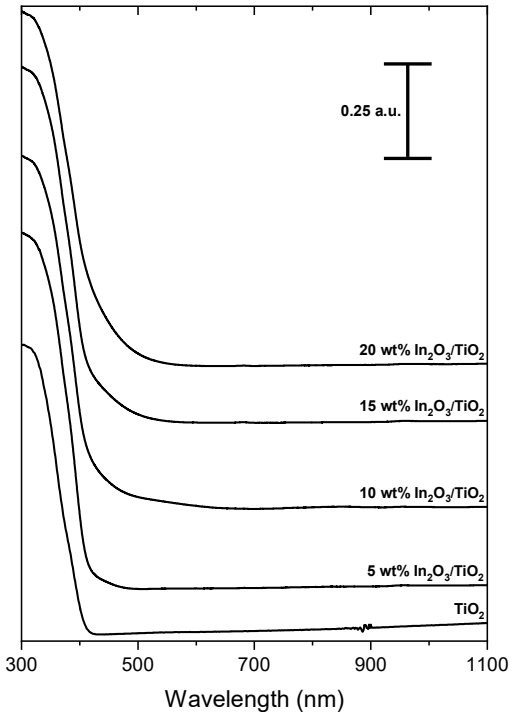

Figure 3.2.6 UV-Vis absorption spectra of In_2O_3/TiO_2 catalysts (5-20 wt%).

Figure 3.2.7 shows a Tauc plot of the 20 wt% In_2O_3/TiO_2 catalyst overlaid with a Tauc plot of the TiO_2 support in the ~310 nm to ~620 nm range. The extrapolated line led to a calculated band gap of 2.87 eV for the 20 wt% In_2O_3/TiO_2 catalyst. Band have been reported in the literature as 2.8 eV for In_2O_3 and ~3.1 eV for TiO_2.[22,35]

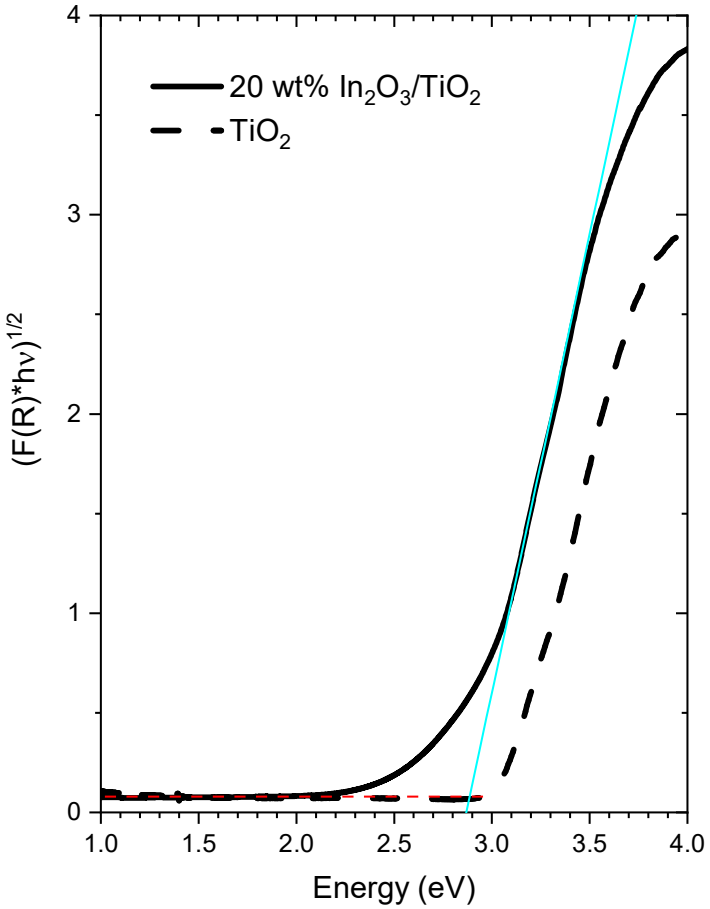

Figure 3.2.7 Plot of $F(R)*h\nu^{1/2}$ vs. eV for determining band gaps in a 20 wt% In_2O_3/TiO_2 catalyst.

Band gaps for the In_2O_3/TiO_2 catalysts are listed in Table 3.2.4. The absorbance by In_2O_3 is too low to quantify a separate band gap, leading to the determination of one band gap each catalyst.

Table 3.2.4. Band gaps of In_2O_3/TiO_2 catalysts as determined from Tauc plot analysis

Wt% In_2O_3	Band Gap (eV)
5	3.01
10	2.96
15	2.97
20	2.87

Absorbance spectra for the $In_xGa_{2-x}O_3/TiO_2$ catalysts are presented in Figure 3.2.8. It is apparent that the deposition of Ga_2O_3 onto TiO_2 has a minimal effect on the absorption spectrum. This can be explained by the fact that TiO_2 has a band gap of 3.0 eV. The <300 nm absorption onset for Ga_2O_3 (band gap = 4.8 eV) would be obscured by the intense absorption of TiO_2.[22,36] As indium content increases, the absorption onset at ~500 nm grows in intensity and appears to shift towards longer wavelengths (> 500 nm).

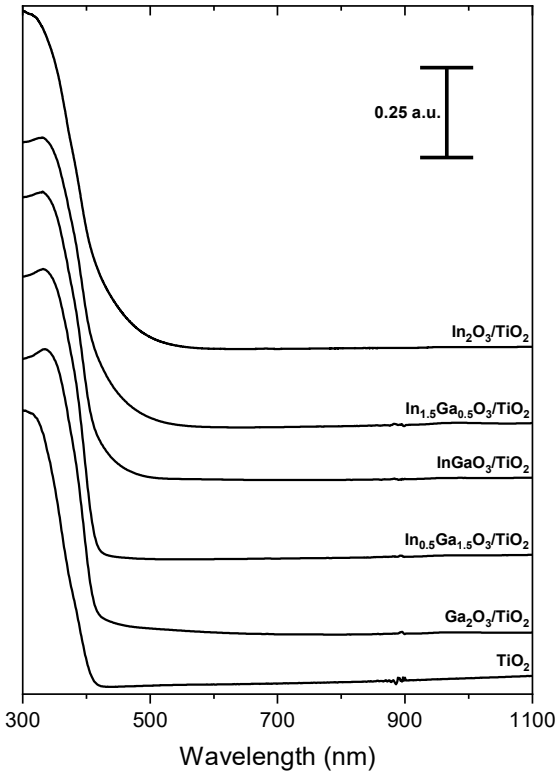

Figure 3.2.8 UV-Vis absorption spectra of 20 wt% $In_xGa_{2-x}O_3/TiO_2$ catalysts.

Figure 3.2.9 shows Tauc plots for the 20 wt% $In_xGa_{2-x}O_3/TiO_2$ catalysts. As indium content is increased, it is apparent from the absorption onset at ~2.5 eV that lower energy photons are absorbed relative to the TiO_2 and Ga_2O_3/TiO_2 catalysts, indicating a decrease in band gap. Figures A.5-A.9 (Appendix) is a collection of all Tauc plots in the 20 wt% $In_xGa_{2-x}O_3/TiO_2$ catalysts, which shows that the technique used to measure band gaps in this thesis work does yield smaller band gaps with an increasing x value, though not to the extent one would assume by observing the significant shift in the absorbance onset as x increases in Figure 3.2.9. It was not possible to determine accurate band gaps for the $In_xGa_{2-x}O_3$ material, due to the overpowering TiO_2 absorption in this region, though a trend towards lower band gaps as x increasing was observed.

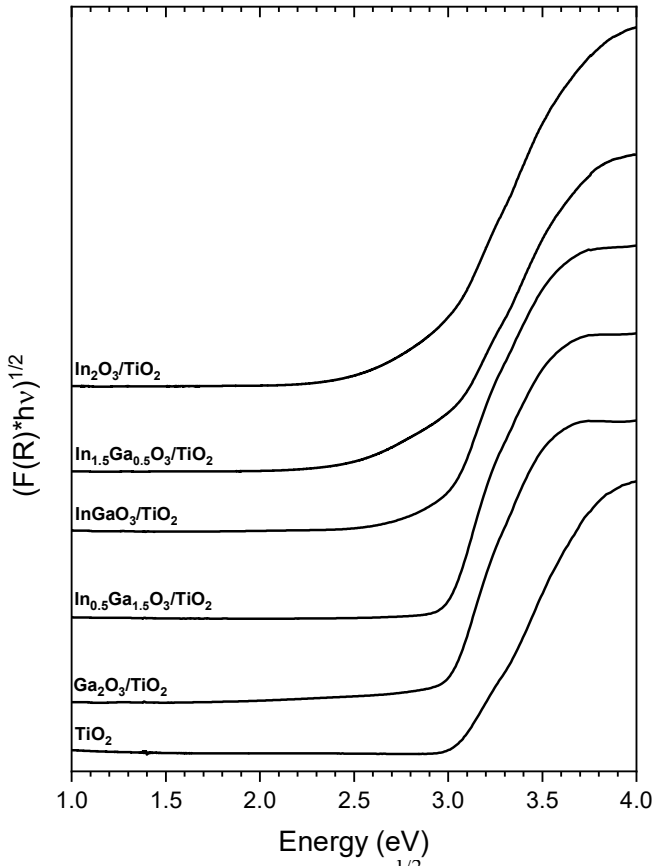

Figure 3.2.9 Plot of $F(R)*h\nu^{1/2}$ vs. eV for determining band gaps of 20 wt% $In_xGa_{2-x}O_3/TiO_2$. $(F(R)*h\nu)^{1/2}$ values are offset to create a stacked plot.

Band gaps for the 20 wt% $In_xGa_{2-x}O_3/TiO_2$ catalysts are listed in Table 3.2.5, which increase slightly with decreasing indium content (from 2.87 eV in In_2O_3/TiO_2 to 2.97 eV in Ga_2O_3/TiO_2).

Table 3.2.5 Band Gaps of 20 wt% $In_xGa_{2-x}O_3/TiO_2$ catalysts.

Catalyst	Band Gap (eV)
Ga_2O_3/TiO_2	2.97
$In_{0.5}Ga_{1.5}O_3/TiO_2$	2.97
$InGaO_3/TiO_2$	2.93
$In_{1.5}Ga_{0.5}O_3/TiO_2$	2.90
In_2O_3/TiO_2	2.87

3.2.4 XPS

XPS spectra for In_2O_3/TiO_2 catalysts having varying In_2O_3 loadings are plotted in Figure 3.2.10. The peak at 444.3-444.9 eV is assigned to the In($3d_{5/2}$) core level of In^{3+} in In_2O_3 based on the literature values of 444.2 and 444.5 eV.[34,37] The In($3d_{5/2}$) signal intensity increases with increasing In_2O_3 loading as expected.

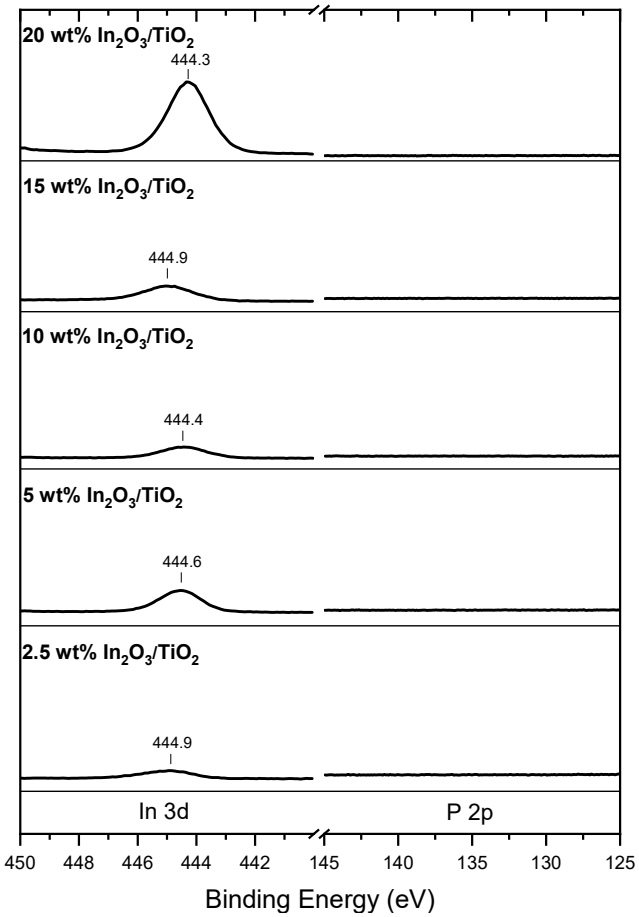

Figure 3.2.10 XPS spectra of In_2O_3/TiO_2 catalysts (2.5-20 wt%).

XPS spectra for the $In_xGa_{2-x}O_3/TiO_2$ catalysts are plotted in Figure 3.2.11 and they show peaks at 444.1-444.4 eV and 1117.4-1117.8 eV, corresponding to the $In(3d_{5/2})$ and $Ga(2p_{3/2})$ core levels in In_2O_3 and Ga_2O_3 reported in the literature between 444.2 and 444.5 eV, and between 1118.1 and 1118.3 eV, respectively.[38,39] The binding energy for $In(3d_{5/2})$ matches well with the In_2O_3 literature values, and the binding energy for $Ga(2p_{3/2})$ matches Ga_2O_3 the literature within uncertainty. Gallium in Ga_2O_3 is assigned a 3+ oxidation state.[40] The general trend in peak intensities is that $In(3d_{5/2})$ grows in as $Ga(2p_{3/2})$ diminishes with increasing In/Ga ratios, as expected.

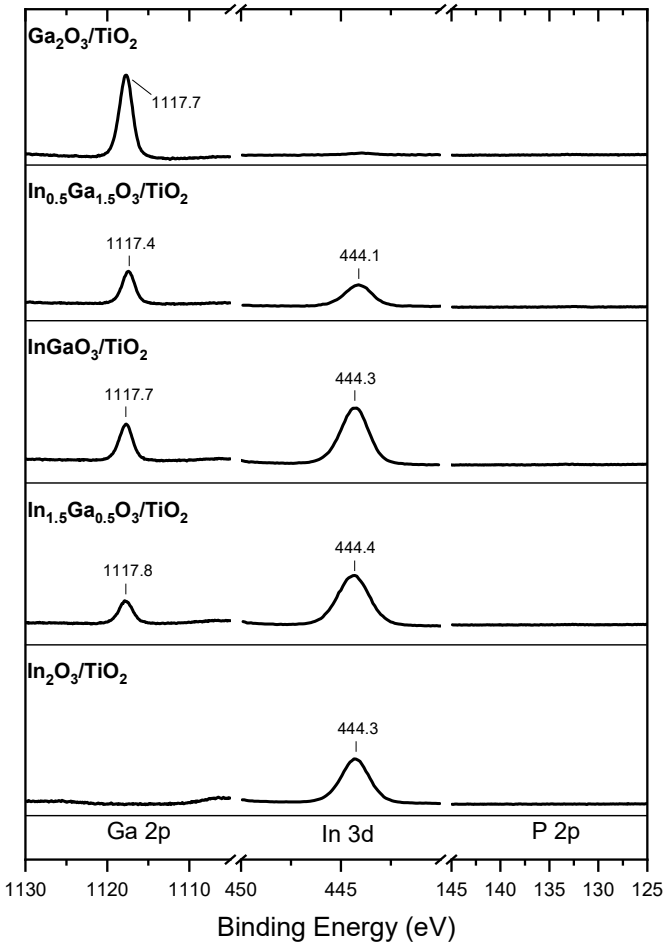

Figure 3.2.11 XPS spectra of 20 wt% $In_xGa_{2-x}O_3/TiO_2$ catalysts.

The XPS spectra were used to determine surface compositions of the $In_xGa_{2-x}O_3/TiO_2$ catalysts (Table 3.2.6). The subscript on oxygen was fixed at 3.00 in each case and the calculated In/Ga ratio was used to determine subscripts on In and Ga, based on an assumed metal-to-oxygen ratio of 2:3. The catalyst with the target composition of $In_{1.5}Ga_{0.5}O_3$ was determined to have a significantly lower XPS-determined In/Ga molar ratio (1.6) relative to what was expected (3.0), suggesting that this catalyst has an enrichment of gallium on its surface.

Table 3.2.6 Surface compositions of 20 wt% $In_xGa_{2-x}O_3/TiO_2$ catalysts as determined by XPS.

Target Bulk Composition	**XPS-Composition**	**In/Ga Molar Ratio (XPS)**
Ga_2O_3	$Ga_2O_{3.00}$	0
$In_{0.5}Ga_{1.5}O_3$	$In_{0.61}Ga_{1.39}O_{3.00}$	0.4
$InGaO_3$	$In_{1.03}Ga_{0.97}O_{3.00}$	1.1
$In_{1.5}Ga_{0.5}O_3$	$In_{1.23}Ga_{0.77}O_{3.00}$	1.6
In_2O_3	$In_2O_{3.00}$	---

3.3 Characterization of $In_xGa_{1-x}P/TiO_2$ Catalysts

3.3.1 XRD

XRD patterns for the InP/TiO_2 catalysts are presented in Figure 3.3.1. The most intense peaks in the XRD patterns line up well with the peaks assigned to the (111), (220), and (311) crystal planes of the InP reference pattern (COD Card No. 9008852). These peaks are visible at 26.2°, 43.5°, and 51.6°, respectively. The 15 and 20 wt% InP/TiO_2 catalysts show impurity peaks assigned $In_2P_2O_7$ between 28.3° and 29.7° (COD Card No. 1535390) and an indium metal impurity peak at 32.9°(COD Card No. 2100456). Figure A.10 shows a stacked XRD plot of the 20 wt% InP/TiO_2 catalyst, and reference patterns for $In_2P_2O_7$ and In metal for visual verification.

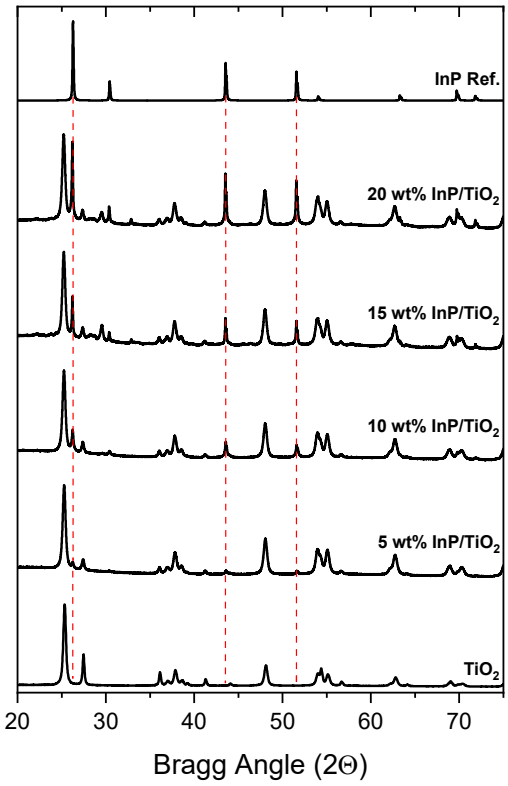

Figure 3.3.1 XRD patterns of InP/TiO_2 catalysts (5-20 wt%).

The InP/TiO_2 catalysts were analyzed for average InP crystallite size determination. The (111), (200), (220), (311), and (420) crystal plane peaks were manually selected for this analysis due to lack of interference from TiO_2 peaks. The average InP crystallite sizes can be found in Table 3.3.1, and reveal the general trend that lower loading results in smaller crystallites.

Table 3.3.1 Average crystallite sizes for InP/TiO_2 catalysts.

Wt% InP	Crystallite Size (nm)
5	36
10	36
15	55
20	46

XRD patterns for the 20 wt% $In_xGa_{1-x}P/TiO_2$ catalysts are presented in Figure 3.3.2. With the exception of the GaP/TiO_2 catalyst, the patterns show peaks that line up well with the peaks assigned to the (111), (220), and (311) crystal planes of the InP reference pattern. The InP/TiO_2 and $In_{0.75}Ga_{0.25}P/TiO_2$ catalysts show impurity peaks arising from $In_2P_2O_7$ and, as mentioned earlier, the InP/TiO_2 catalyst pattern contains an indium metal peak at 32.9°. The GaP/TiO_2 catalyst shows only peaks from the TiO_2 support, and a weak peak at 22° that may originate

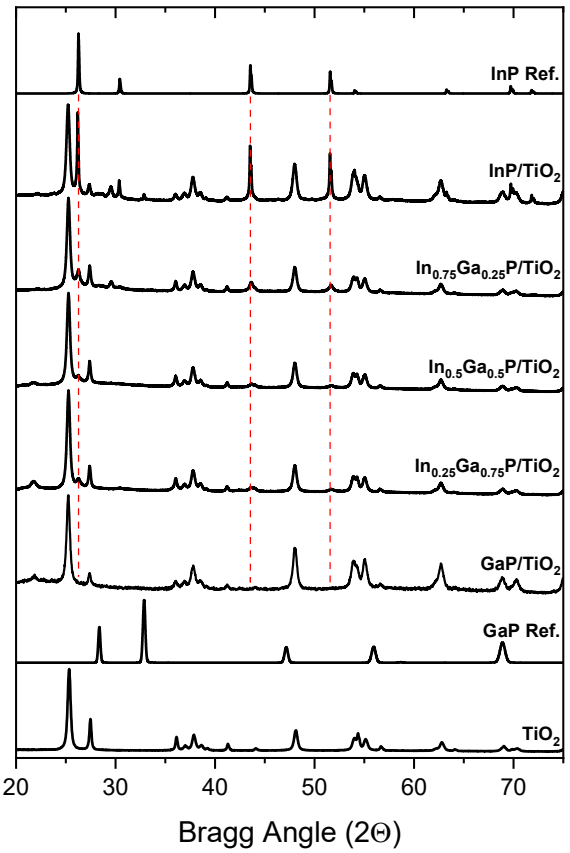

Figure 3.3.2 XRD patterns of 20 wt% $In_xGa_{1-x}P/TiO_2$ catalysts.

from surface-oxidized GaP (GaO_4P; COD: 5910199). Figure A.11 shows this GaO_4P peak in the region expected for this impurity. Identification of these impurities reveals that the current synthetic route is flawed and must be optmimized in order to yield phase pure material.

Figure 3.3.3 shows an expansion of the 43.0° to 47.5° region of the $In_xGa_{1-x}P/TiO_2$ diffraction patterns. These patterns reveal a shift of the (220) peak position of InP from 43.5° to 43.6° upon incorporation of gallium (comparing the InP/TiO_2 and $In_{0.75}Ga_{0.25}P/TiO_2$ catalysts) followed by another shift to 43.7° upon further addition of gallium.

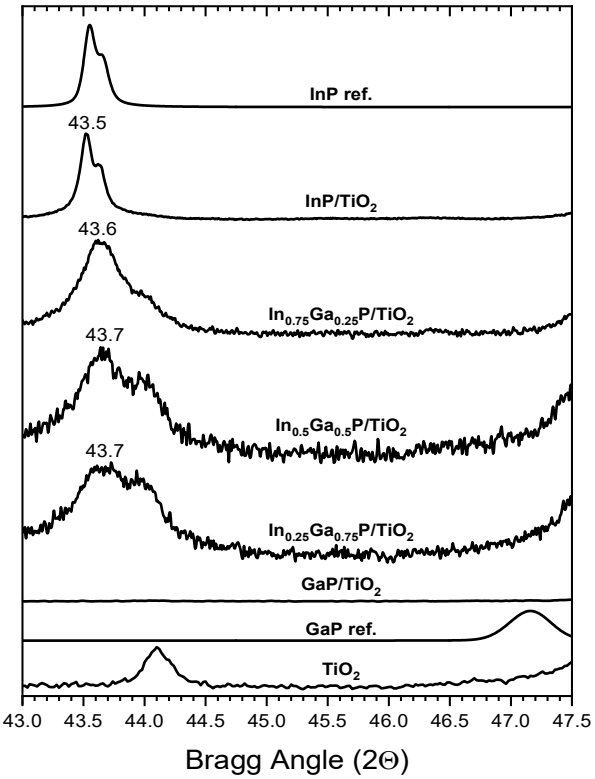

Figure 3.3.3 Expansion of 20 wt% $In_xGa_{1-x}P/TiO_2$ XRD plots in the 43.0° - 47.5° range.

The preparation and properties of $In_xGa_{1-x}P$ nanowires have been reported in the literature,[28] and the XRD peaks for these nanowires have been shown to follow Vegard's law for solid solutions. Vegard's law states that when varying the concentration of two constituent elements in a solid solution, there is a linear relationship between the relative concentration of the constituent elements and the lattice parameter of the resulting crystal structure.[28] The consequence of this law in terms of XRD is that by varying x in $In_xGa_{1-x}P$ from 1 to 0, a linear shift in the (220) crystal plane peak should occur from ~ 43.5° in InP to 47.1° in GaP.

Average crystallite sizes for the $In_xGa_{1-x}P/TiO_2$ catalysts can be viewed in Table 3.3.2. This table shows the trend of increasing indium content resulting in larger crystallites in the

range of 13 to 46 nm. The InP crystallite size determined (46 nm) is significantly higher than the $In_xGa_{1-x}P$ crystallite sizes found in the remaining catalysts, which could be explained by the fact that InP has a lower melting point (1330-1510 K) than GaP (1620-1950 K), causing nanoparticles composed of phases that include gallium to experience less of a sintering effect when heated.[41] Crystallite sizes for the GaP/TiO_2 catalyst could not be determined, due to the absence of GaP peaks in the diffraction pattern.

Table 3.3.2 Average crystallite sizes for 20 wt% $In_xGa_{1-x}P/TiO_2$ catalysts.

Catalyst	Crystallite Size (nm)
GaP/TiO_2	---
$In_{0.25}Ga_{0.75}P/TiO_2$	13
$In_{0.5}Ga_{0.5}P/TiO_2$	13
$In_{0.75}Ga_{0.25}P/TiO_2$	16
InP/TiO_2	46

3.3.2 EDS and SEM

Bulk elemental compositions of the InP/TiO_2 catalysts were determined via EDS. Indium was analyzed using the L_α peak at 3.3 keV, and analysis of phosphorous utilized the K_α peak just above 2 keV. The spectra in Figure 3.3.4 show the In L_α peak intensities growing in tandem with P K_α intensities as InP loading is increased.

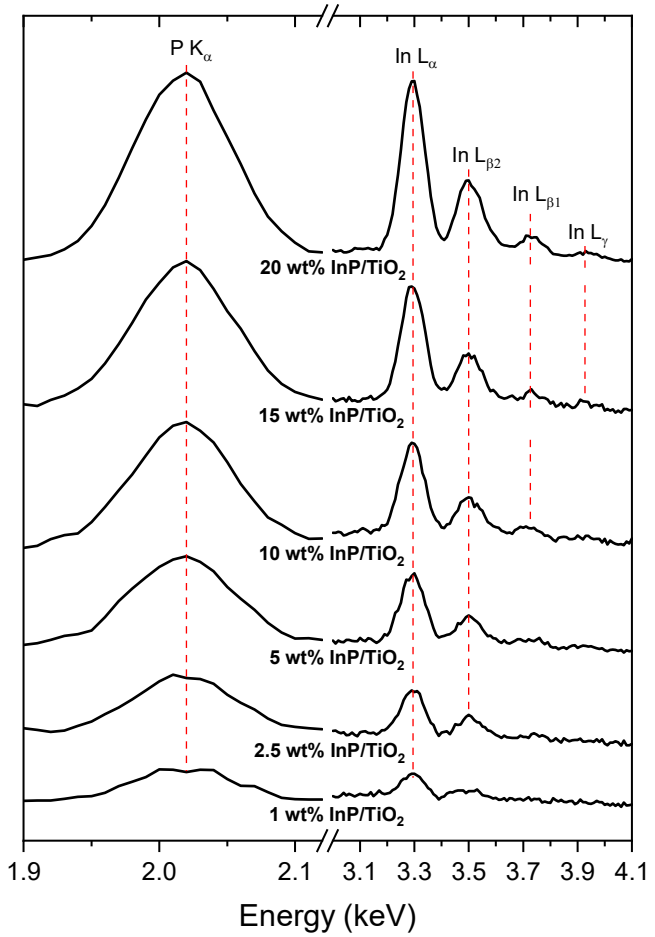

Figure 3.3.4 EDS spectra for InP/TiO_2 catalysts (1-20 wt%).

The bulk compositions of the InP/TiO_2 catalysts are presented in Table 3.3.3. The expected P/In ratio is 1.00, based on the stoichiometric 1:1 ratio in InP, but was determined to be greater than 1.00 for each InP/TiO_2 catalyst. The formulas were determined by fixing the P subscript to 1.00, and using the calculated In/P ratio as the In subscript. The uncertainties provided in Table 3.3.3 are the standard deviations based on 3-5 measurements.

Table 3.3.3 Bulk compositions of InP/TiO_2 catalysts as determined by EDS.

Wt% InP	Atomic P/In (EDS)	Formula (EDS)
1	1.37±0.06	$In_{0.73\pm0.03}P_{1.00}$
2.5	1.31±0.09	$In_{0.9\pm0.07}P_{1.00}$
5	1.07±0.02	$In_{0.93\pm0.02}P_{1.00}$
10	1.34±0.14	$In_{0.76\pm0.08}P_{1.00}$
15	1.20±0.05	$In_{0.83\pm0.03}P_{1.00}$
20	1.13±0.09	$In_{0.9\pm0.07}P_{1.00}$

Bulk elemental compositions of the $In_xGa_{1-x}P/TiO_2$ catalysts were also determined via EDS. Indium and gallium were analyzed using the L_α peaks at 3.3 and 1.1 keV, respectively, and analysis of phosphorous utilized the K_α peak just above 2 keV. The spectra shown in Figure 3.3.5 reveal increasing In L_α peak intensities and decreasing Ga L_α peak intensities as the value of x in the $In_xGa_{1-x}P/TiO_2$ catalysts increased.

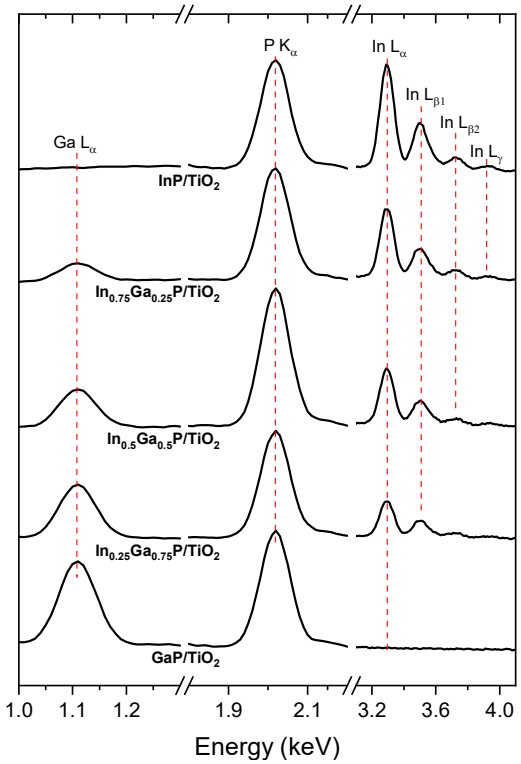

Figure 3.3.5 EDS spectra for 20 wt% $In_xGa_{1-x}P/TiO_2$ catalysts.

Bulk compositions of the $In_xGa_{1-x}P/TiO_2$ catalysts are presented in Table 3.3.4. The expected trend of increasing indium-to-gallium ratio with increasing x is apparent, while the P/M molar ratio was greater than 1.0 for these catalysts. This may be a consequence of either the uncertainty in the metal nitrate precursor hydrate numbers (y in $In(NO_3)_3 \bullet yH_2O$ and z in $Ga(NO_3)_3 \cdot zH_2O$) or it could be due to excess phosphate species as a consequence of the syntheses having a nominal P/M of ~1.25. A P/M molar ratio greater than 1.0 was used in the synthesis to account for phosphorous lost as phosphine (PH_3) during the 873 K reduction step. The formulas in Table 3.3.4 were determined by fixing the P subscript to 1.00, and using the calculated In/P and Ga/P ratios as subscripts for In and Ga, respectively.

Table 3.3.4 Compositions of 20 wt% $In_xGa_{1-x}P/TiO_2$ catalysts, as determined by EDS.

Target Bulk Composition	**In/Ga (EDS)**	**P/M (EDS)**	**Formula (EDS)**
$Ga_{1.00}P_{1.00}$	0	3.09±0.64	$Ga_{0.33\pm0.06}P_{1.00}$
$In_{0.25}Ga_{0.75}P_{1.00}$	0.70±0.16	1.41±0.03	$In_{0.29\pm0.04}Ga_{0.42\pm0.04}P_{1.00}$
$In_{0.50}Ga_{0.50}P_{1.00}$	1.58±0.27	1.46±0.14	$In_{0.42\pm0.06}Ga_{0.27\pm0.03}P_{1.00}$
$In_{0.75}Ga_{0.25}P_{1.00}$	3.28±0.49	1.43±0.17	$In_{0.52\pm0.06}Ga_{0.16\pm0.02}P_{1.00}$
$In_{1.00}P_{1.00}$	---	1.13±0.09	$In_{0.89\pm0.07}P_{1.00}$

3.3.3 UV-Vis-NIR Spectroscopy

The UV-Vis spectrum labeled "TiO_2" in the following plots is the absorbance spectrum for a sample of TiO_2 that has been calcined at 673 K and subjected to the same TPR program that was used in the syntheses of the $In_xGa_{1-x}P/TiO_2$ catalysts it is compared to. Figure A.12 in the appendix shows the absorption spectrum for TiO_2 after calcination and compares it to the absorption spectrum of the TiO_2 support after subsequent reduction under flowing hydrogen at 873 K. The comparison reveals that, upon reduction, TiO_2 develops broad absorption in the 400-1100 nm range (~1-3 eV). TiO_2 absorbance in the 1-3 eV range has also been reported in the literature in samples of TiO_2 that have been exposed to a reducing atmosphere (H_2) at elevated temperatures (>700 K).[42] The source of this increased absorption has been debated, though it seems likely due to defects in partially reduced TiO_2 (Ti^{3+} ions/oxygen vacancies). UV-Vis absorption spectra for the InP/TiO_2 catalysts are presented in Figure 3.3.6. The general trend is that as InP loading increases, the absorption in the 400-900 nm region increases.

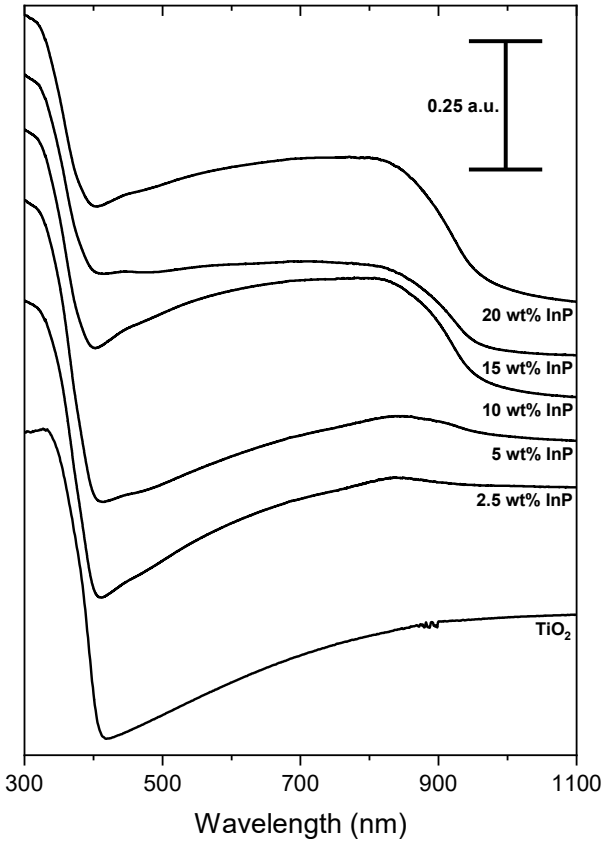

Figure 3.3.6 UV-Vis absorption spectra of InP/TiO_2 catalysts (2.5-20 wt%).

A Tauc plot for the 20 wt% InP/TiO_2 catalyst is presented in Figure 3.3.7 and is overlaid with a Tauc plot for TiO_2 for comparison. The band gaps for this InP/TiO_2 catalyst were measured to be 1.26 and 3.01 eV and were assigned to InP and TiO_2, respectively.

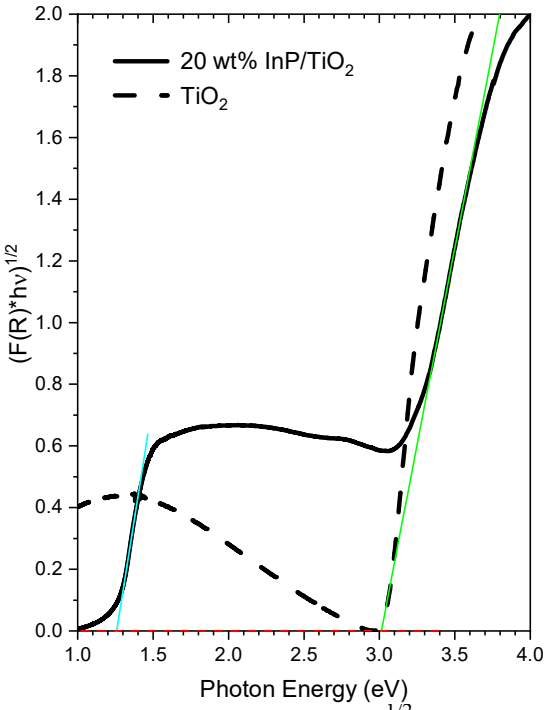

Figure 3.3.7 Plot of F(R)*$h\nu^{1/2}$ vs. eV for determining band gaps in a 20 wt% InP/TiO_2 catalyst.

Band gaps for the InP/TiO_2 catalysts with InP loadings of 5-20 wt% are listed in Table 3.3.5. As the InP peak decreases in intensity with decreasing loading, the measured band gap decreases. This is due to the InP peak being only weakly observed and obscured by the TiO_2 peak in the 1-3 eV range, a direct result of increased absorbance in this region upon reduction of TiO_2. This increased absorbance from the support causes the Tauc plot analysis to become unreliable at a loading of 5 wt% InP (See Figure A.13 in the appendix for the Tauc plot for 5 wt% InP/TiO_2).

Table 3.3.5 Band gaps of InP/TiO_2 catalysts as determined from Tauc plot analysis.

Wt%	**Band Gap of InP (eV)**	**Band Gap of TiO_2 (eV)**
5	1.19	3.16
10	1.28	3.13
15	1.28	3.04
20	1.26	3.01

UV-Vis spectra for the 20 wt% $In_xGa_{1-x}P/TiO_2$ catalysts are shown in Figure 3.3.8. The InP/TiO_2 spectrum shows a broad absorption band (400-900 nm), which is assigned to the InP species. The figure also shows that as indium content is decreased, InP absorption decreases is replaced by an absorption band in the 400-600 nm region when no indium is present (in the GaP/TiO_2 catalyst). Absorption in this region agrees well with the absorption peak at ~500 nm for GaP nanoparticles seen in previous published work (This GaP absorption spectrum was shown earlier in Figure 1.2).[11]

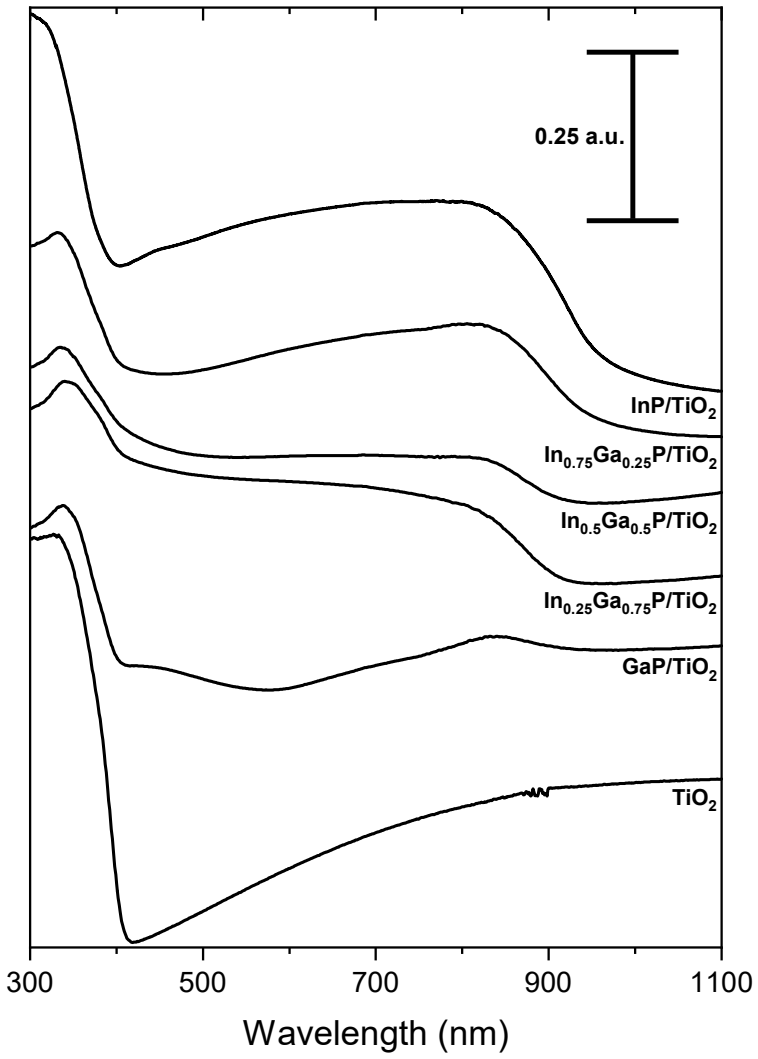

Figure 3.3.8 UV-Vis absorption spectra of 20 wt% $In_xGa_{1-x}P/TiO_2$ catalysts.

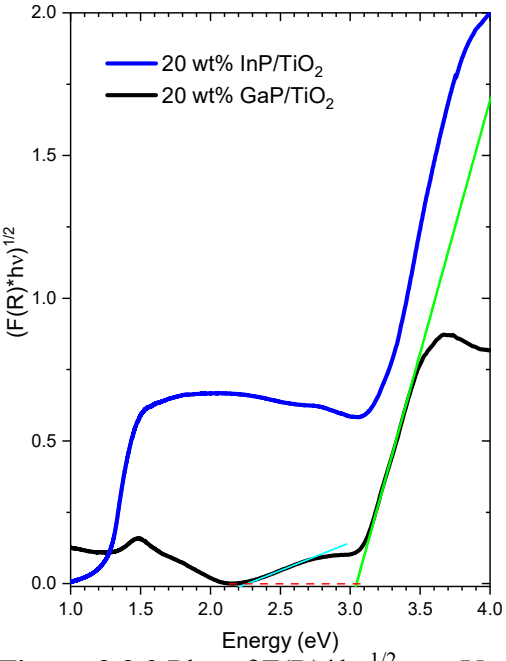

Figure 3.3.9 Plot of $F(R)*h\nu^{1/2}$ vs. eV for determining band gaps in a 20 wt% GaP/TiO_2 catalyst.

Figure 3.3.9 shows Tauc plots for the GaP/TiO_2 and InP/TiO_2 catalysts in the 1.0-4.0 eV region (1240-310 nm) for comparison. The derivative of the Tauc plot for GaP/TiO_2 revealed two maxima in the 2.0-4.0 eV region (Figure 3.3.10) and a line was extrapolated to baseline for each. Analysis led to the determination of two band gaps, 2.26 and 3.05 eV, assigned to be the band gaps of GaP (based on the literature value of 2.3 eV)[28] and TiO_2, respectively. Figure 3.3.10 is a stacked plot of the five Tauc plots for the $In_xGa_{1-x}P/TiO_2$ catalysts for ease of comparison across the series.

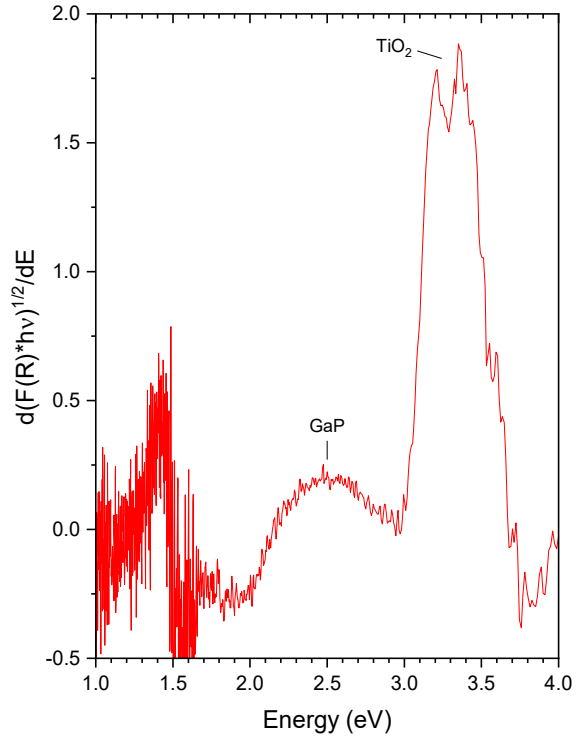

Figure 3.3.10 Derivative of the Tauc plot for 20 wt% GaP/TiO_2.

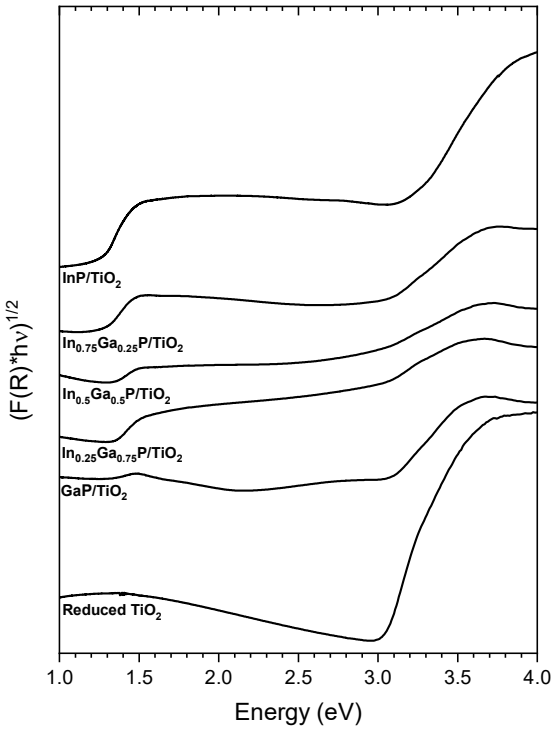

Figure 3.3.11 Plots of $F(R)*h\nu^{1/2}$ vs. eV for determining band gaps in 20 wt% $In_xGa_{x-1}P/TiO_2$. $(F(R)*h\nu)^{1/2}$ values are offset to create a stacked plot.

Table 3.3.6 lists the band gaps for the $In_xGa_{1-x}P/TiO_2$ series of catalysts and reveals a general trend of decreasing band gaps with increasing indium content, though the band gap shift (2.28 to 1.26 eV from x = 0.25 to x = 1.0, $\Delta E \approx -0.1$ eV) is not nearly what was expected based on literature (approximately 2.1 to 1.35 eV from x = 0.21 to x = 1.0, $\Delta E \approx -0.8$ eV).

Table 3.3.6 Band Gaps of 20 wt% $In_xGa_{1-x}P/TiO_2$ catalysts.

Catalyst	InP Band Gap (eV)	$In_xGa_{1-x}P$ Band Gap (eV)	GaP Band Gap (eV)	*TiO_{2-x} Band Gap (eV)
GaP/TiO_2	---	---	2.26	3.05
$In_{0.25}Ga_{0.75}P/TiO_2$	---	1.36	2.28	2.54
$In_{0.5}Ga_{0.5}P/TiO_2$	---	1.36	---	2.68
$In_{0.75}Ga_{0.25}P/TiO_2$	---	1.29	---	2.88
InP/TiO_2	1.26	---	---	3.01

*TiO_2 is expected to be partially reduced during the TPR step in the synthesis of $In_xGa_{1-x}P/TiO_2$.

Table 3.3.6 lists the $In_{0.25}Ga_{0.75}P/TiO_2$ catalyst as having three band gaps, which requires some explanation. Figure 3.3.12 shows the derivative of the Tauc plot for $In_{0.25}Ga_{0.75}P/TiO_2$, revealing three maxima. This led to the extrapolation of three lines, shown in the Tauc plot in Figure 3.3.13, ultimately resulting in the determination of three band gaps.

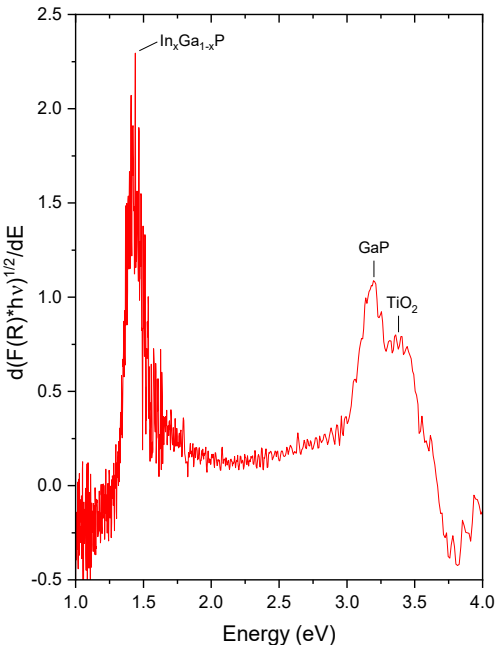

Figure 3.3.12 Derivative of the Tauc plot for 20 wt% $In_{0.25}Ga_{0.75}P/TiO_2$.

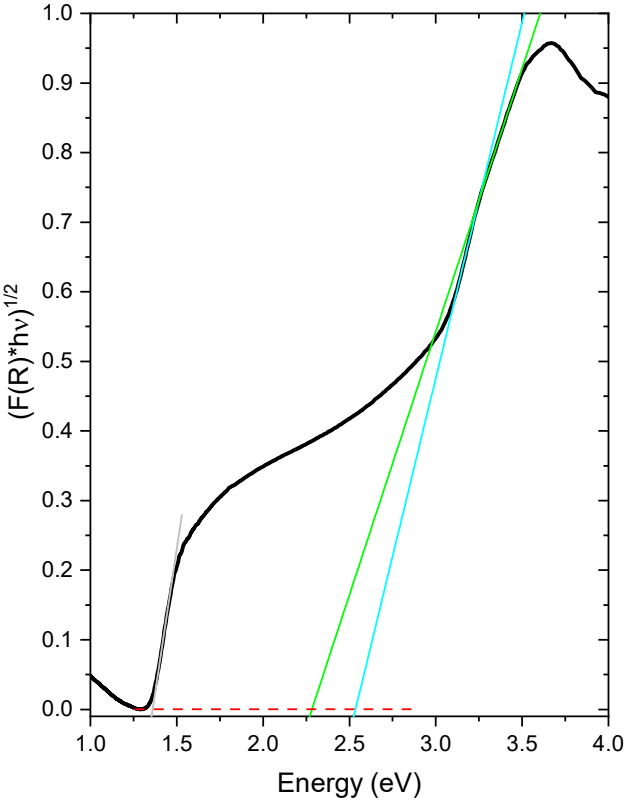

Figure 3.3.13 Tauc plot for the $In_{0.25}Ga_{0.75}P/TiO_2$ catalyst.

3.3.4 XPS

XPS spectra for the $In_xGa_{1-x}P/TiO_2$ catalysts are presented in this section. A challenge faced during the analysis of these XPS spectra stemmed from the fact that the supported phosphide phase ($In_xGa_{1-x}P$) is readily oxidized upon air exposure. For this reason, after synthesis and before exposing the catalysts to air, they were passivated by flowing dilute oxygen gas (1.001 mol% O_2/He) over the catalyst to form an oxide layer in a more controllable setting than direct exposure to air (~21% O_2). Due to the surface of the metal phosphides being oxidized, XPS analysis yielded spectra composed of peaks for the reduced ($In_xGa_{1-x}P$) nanoparticles and the oxidized outer layer of the particles

XPS spectra for the InP/TiO_2 catalysts (2.5-20 wt% InP) are shown in Figure 3.3.14. The spectra show the expected trend of increasing indium and phosphorous signals as the InP loading increases. The In($3d_{5/2}$) peak is in the 444.6-445.3 eV range, which is a higher binding energy than what is reported in the literature for InP (444.0 eV),[43] suggesting a more oxidized indium species, a consequence of the indium phosphides having an oxide layer. In fact, the binding energies found in these catalysts agree well with what has been reported for In_2O_3 (444.5 eV).[35] The dominant P (2p) peak appears in the 133.2-133.8 eV range, and a minor peak is observed at 128.2 and 128.5 eV. This is also in agreement with literature values (133.4 eV for oxidized InP and 128.8 eV for InP).[43,44]

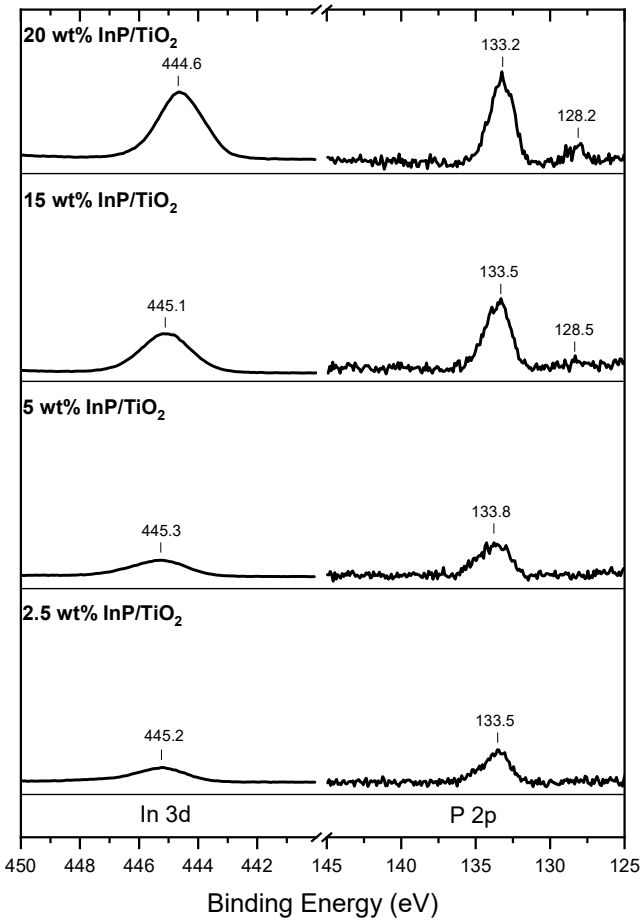

Figure 3.3.14 XPS spectra of InP/TiO_2 catalysts (2.5-20 wt%).

Surface compositions for the InP/TiO_2 catalysts are listed in Table 3.3.7; InP is expected to have a surface P/In molar ratio of 1. The XPS measurements reveal a relatively wide range of P/In values (0.79 to 1.38). The average P/In value across the InP/TiO_2 series is 1.12, slightly more phosphorous rich than the stoichiometric value.

Table 3.3.7 Surface compositions of InP/TiO_2 catalysts, as determined by XPS.

Wt% InP	Atomic P/In (XPS)	Formula (XPS)
2.5	1.22	$In_{0.82}P_{1.00}$
5	1.38	$In_{0.72}P_{1.00}$
15	1.09	$In_{0.92}P_{1.00}$
20	0.79	$In_{1.26}P_{1.00}$

XPS spectra of the $In_xGa_{1-x}P/TiO_2$ catalysts are shown in Figure 3.3.15. The Ga($2p_{3/2}$) peak positions were in the 1118.0 to 1118.6 eV range, which agrees well with what has been found for surface oxidized GaP particles (1118.1-1118.3 eV),[40,43] and In($3d_{5/2}$) peaks are still appearing in the 444.6-445.3 eV range as seen for the InP/TiO_2 catalysts. P(2p) peaks observed in this analysis range from 133.2-134.0 eV and 128.2-129.0 eV, also in agreement with literature values. XPS spectra of surface-oxidized InP nanocrystals and GaP crystals show P(2p) having binding energies

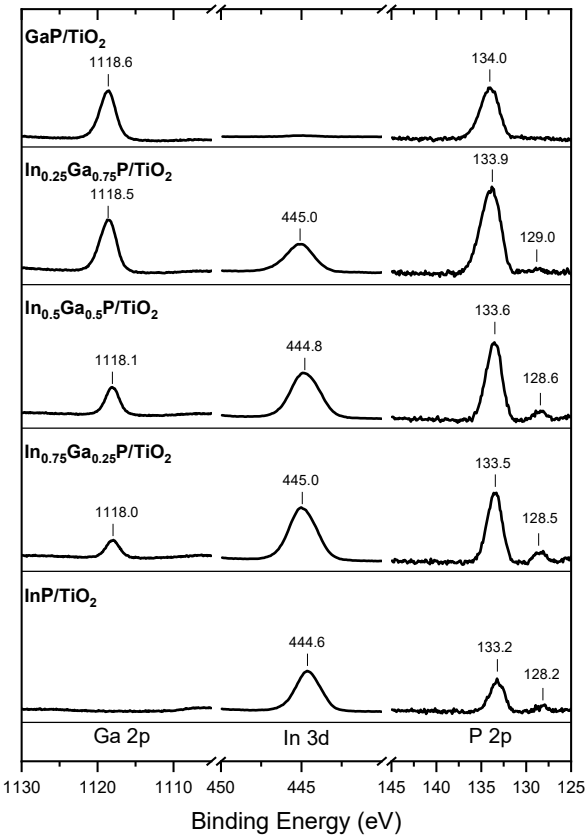

Figure 3.3.15 XPS spectra of 20 wt% $In_xGa_{x-1}P/TiO_2$ catalysts.

of 133 and 134 eV, respectively, while P(2p) peaks are expected at 128.8 eV for the reduced InP nanocrystals and GaP crystals.[38,43]

Surface compositions of the $In_xGa_{1-x}P/TiO_2$ catalysts are presented in Table 3.3.8, along with In/Ga and P/M molar ratios. The indium-to-gallium molar ratio is shown to increase with increasing indium content as expected, and the phosphorous to metal molar ratios were 0.66-0.89 with an average of 0.80, less than the expected P/M=1, indicating that the surfaces of the $In_xGa_{1-x}P$ particles are metal-rich.

Table 3.3.8 Surface compositions of 20 wt% $In_xGa_{1-x}P/TiO_2$ catalysts as determined by XPS.

Target Bulk Composition	XPS Composition	Atomic In/Ga (XPS)	Atomic P/M (XPS)
$Ga_{1.00}P_{1.00}$	$Ga_{1.51}P_{1.00}$	0	0.66
$In_{0.25}Ga_{0.75}P_{1.00}$	$In_{0.27}Ga_{0.85}P_{1.00}$	0.3	0.89
$In_{0.50}Ga_{0.50}P_{1.00}$	$In_{0.63}Ga_{0.54}P_{1.00}$	1.2	0.85
$In_{0.75}Ga_{0.25}P_{1.00}$	$In_{0.85}Ga_{0.39}P_{1.00}$	2.2	0.81
$In_{1.00}P_{1.00}$	$In_{1.26}P_{1.00}$	---	0.79

3.4 Characterization of Ni_2P/TiO_2 Catalysts

3.4.1 XRD

Diffraction patterns for Ni_2P/TiO_2 catalysts having loadings of 2.5-20 wt% Ni_2P are presented in Figure 3.4.1. As loading increases, starting with 10 wt%, three peaks become observable at the 40.7°, 44.6°, and 47.4° positions, which arise from the (111), (201), and (201) crystal planes of hexagonal Ni_2P, respectively (COD No. 1537576). There are no observable Ni_2P peaks between 53° and 56°, owing to the fact that the weak diffraction signals are shielded by the relatively intense TiO_2 peaks in this region.

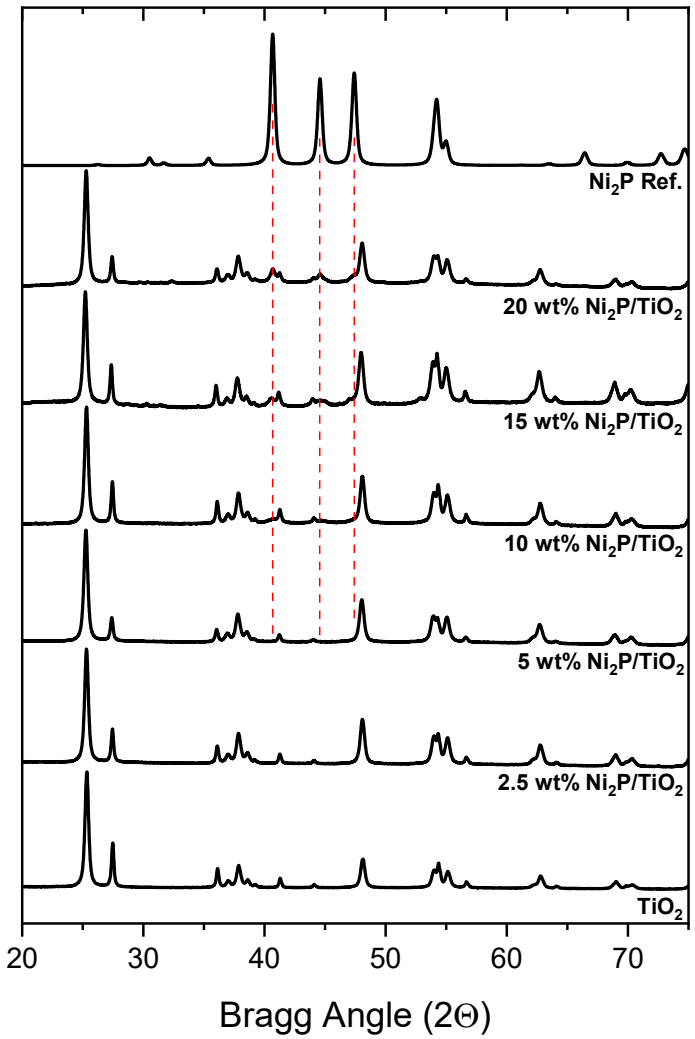

Figure 3.4.1 XRD patterns of Ni_2P/TiO_2 catalysts (2.5-20 wt%).

Ni_2P crystallites sizes were measured using the (101), (111), and (201) diffraction peaks. Crystallite sizes for catalysts with quantificational peaks can be viewed in Table 3.4.1.

Table 3.4.1 Average crystallite sizes for Ni_2P/TiO_2 catalysts.

Wt%	Crystallite Size (nm)
2.5	---
5	---
10	7
15	7
20	15

3.4.2 EDS and SEM

EDS spectra for the Ni_2P/TiO_2 catalysts are shown in Figure 3.4.2. These spectra show Ni L_α and P K_α peaks growing in at ~ 0.85 and 7.5 keV, respectively, as the Ni_2P loading increases. Elemental compositions and P/Ni molar ratios for the Ni_2P/TiO_2 catalysts are presented in Table 3.4.2. The subscripts on phosphorous were all fixed at 1.00, and the Ni/P molar ratios were used as the nickel subscripts. Uncertainties were taken as the standard deviation based on measurements from 5-8 locations on each sample. Most P/Ni ratios determined here are significantly higher

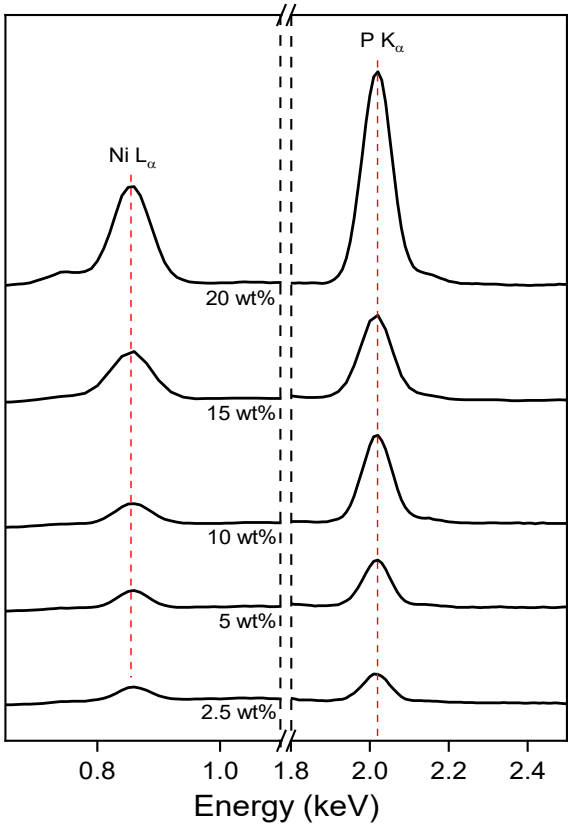

Figure 3.4.2 EDS spectra for the Ni_2P/TiO_2 catalysts (2.5-10 wt%).

than what is expected based on the presence of Ni_2P, evidenced by XRD pattern recognition. This can be explained by the fact that the nominal P/Ni ratio used in these syntheses was P/Ni=2. Excess phosphorous (hypophosphite) was expected to decompose and leave as gaseous PH_3 during the reaction, though it seems that some phosphorous species have remained on the Ni_2P/TiO_2 catalyst, possibly in the form of phosphate, closely associated with titanium atoms in TiO_2. The detector is receiving signals from all phosphorous species and is unable to distinguish between them, which distorts the EDS determined nickel phosphide formulae. Reducing the nominal P/Ni ratio in the synthesis of Ni_2P/TiO_2 has not yet been explored.

Table 3.4.2 Compositions of Ni_2P/TiO_2 catalysts as determined by EDS.

Wt% Ni_2P	**Atomic P/Ni (EDS)**	**Formula (EDS)**
2.5	1.45±0.16	$Ni_{0.70\pm0.08}P_{1.00}$
5	1.12±0.11	$Ni_{0.90\pm0.09}P_{1.00}$
10	0.98±0.11	$Ni_{1.03\pm0.11}P_{1.00}$
15	0.50±0.02	$Ni_{2.01\pm0.08}P_{1.00}$
20	1.78±0.17	$Ni_{0.57\pm0.05}P_{1.00}$

3.4.3 UV-Vis-NIR Spectroscopy

UV-Vis absorption spectra for the Ni_2P/TiO_2 catalysts are presented in Figure 3.4.3. The spectra show that as Ni_2P loading is increased, a broad absorption peak grows in at ~820 nm along with an increase in absorption between 400 and 900 nm (this increase in absorption can be seen by comparison with the TiO_2 absorption slope).

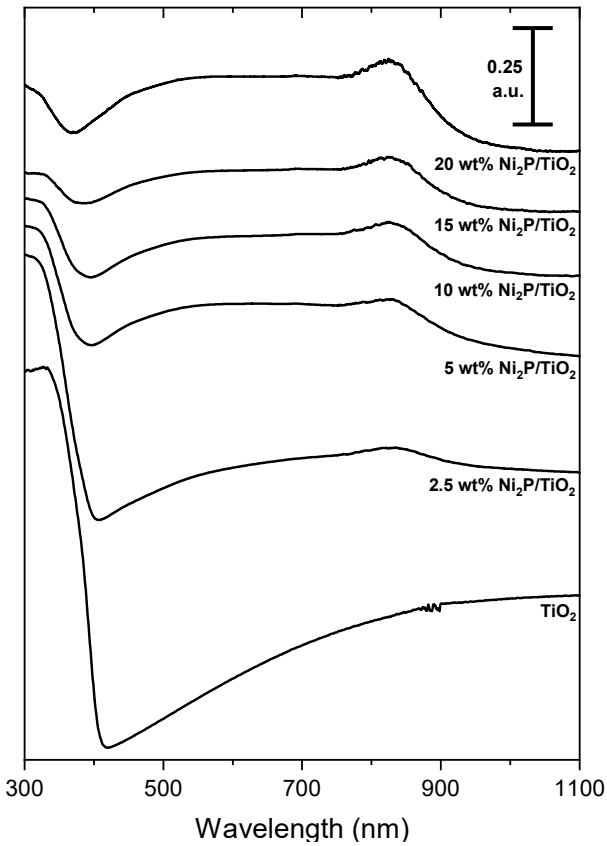

Figure 3.4.3 UV-Vis absorption spectra of Ni_2P/TiO_2 catalysts (2.5-20 wt%).

Previous literature has determined a 1.0 eV band gap for as-prepared "bulk" Ni_2P (in powder form), though it is widely debated that Ni_2P is metallic and has no band gap.[15,20] Figure 3.4.4 shows a Tauc plot in the 1.0-4.0 eV (1240 and 310 nm) region for the Ni_2P/TiO_2 catalysts. Two lines were extrapolated through the portion of the plot that corresponds to the Ni_2P and TiO_2 absorption onsets. This analysis leads to the calculation of two band gaps for the 20 wt% Ni_2P/TiO_2 catalyst. The first (1.2 eV)

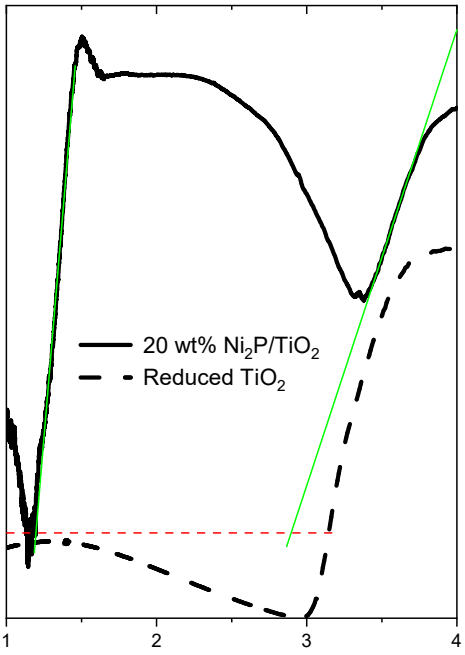

Figure 3.4.4 Plot of $F(R)*hv^{1/2}$ vs. eV for determining band gaps in a 20 wt% Ni_2P/TiO_2 catalyst.

is assigned to the band gap of Ni_2P and the second (2.9 eV) is assigned to TiO_2. The band gaps determined for the Ni_2P/TiO_2 catalysts are listed in Table 3.4.3.

Table 3.4.3 Band gaps of Ni_2P/TiO_2 catalysts as determined from Tauc plot analysis.

Wt% Ni_2P	Band Gap of Ni_2P (eV)	Band Gap of TiO_2 (eV)
2.5	1.1	3.2
5	1.1	3.3
10	1.2	3.2
15	1.3	3.2
20	1.2	2.9

3.4.4 XPS

XPS spectra for the Ni_2P/TiO_2 catalysts are shown in Figure 3.4.5. Three Ni(2p) peaks are identified in the Ni($2p_{3/2}$) region: 852.6-854.8 eV, 855.7-857.6 eV, and 860.6-862.9 eV. Based on the literature these can be assigned to nickel in Ni_2P (852.62 eV), oxidized Ni_2P (856.70 eV), and the Ni($2p_{3/2}$) satellite peak, respectively.[45] It is apparent that the 20 wt% Ni_2P catalyst has a significant amount of reduced nickel species, as indicated by the large low-binding-energy peak (at 852.6 eV). This is likely due to the fact that

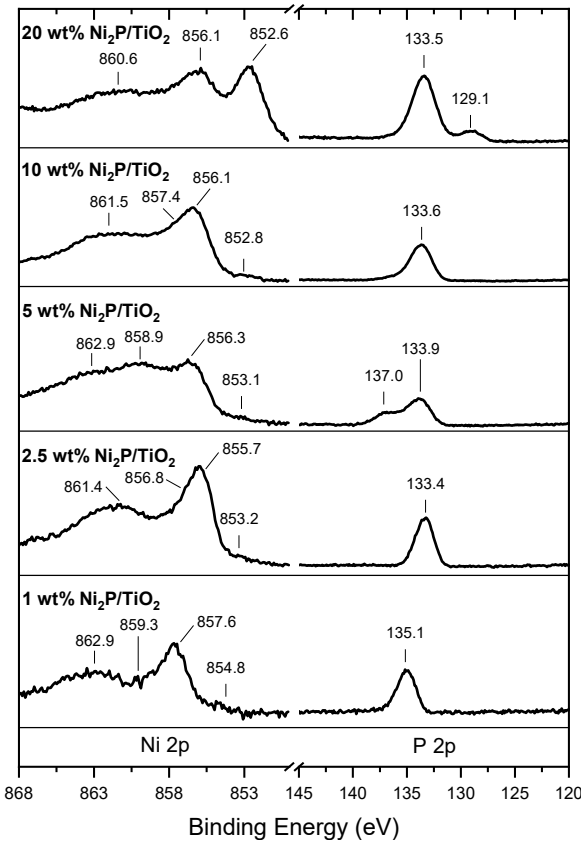

Figure 3.4.5 XPS spectra of Ni_2P/TiO_2 catalysts (1-40 wt%).

the particles are significantly larger (15 nm compared to 7 nm in catalysts with lower Ni_2P loadings), increasing their surface-to-volume ratio.

Surface compositions were calculated for the NiP/TiO_2 catalysts and are presented in Table 3.4.4 and the surfaces were determined to be phosphorous rich. All catalysts exhibit P/Ni molar ratios of 1.27 and higher, significantly larger than the target P/Ni molar ratio of 0.5 based on Ni_2P stoichiometry. P/Ni molar ratios are higher here than they were based on EDS analysis, likely due to XPS being sensitive to the excess phosphorous on the surface of the catalyst mentioned in the EDS discussion.

Table 3.4.4 Surface compositions of the Ni_2P/TiO_2 catalysts as determined by XPS.

Wt% Ni_2P	**Surface P/Ni (XPS)**	**Formula (XPS)**
1	1.49	$Ni_{0.67}P_{1.00}$
2.5	1.27	$Ni_{0.79}P_{1.00}$
5	1.34	$Ni_{0.75}P_{1.00}$
10	1.42	$Ni_{0.71}P_{1.00}$
20	3.15	$Ni_{0.32}P_{1.00}$

3.5 Characterization of Ni_2P-InP/TiO_2 Catalyst

3.5.1 XRD

The X-ray diffraction pattern for a Ni_2P-InP/TiO_2 catalyst is shown in Figure 3.5.1, along with Ni_2P and InP reference patterns above, and the diffraction pattern of the TiO_2 support below. Crystal phase identification was done by comparing experimental XRD patterns with Ni_2P (Card No. 1537576) and InP (Card No. 9008852) reference patterns found in the COD database. The most intense diffraction peaks for InP, corresponding to the (111), (220), and (311) crystalline planes, are observed at 26.2°, 43.5°, and 51.6°, respectively. Peaks assigned to Ni_2P were not detected.

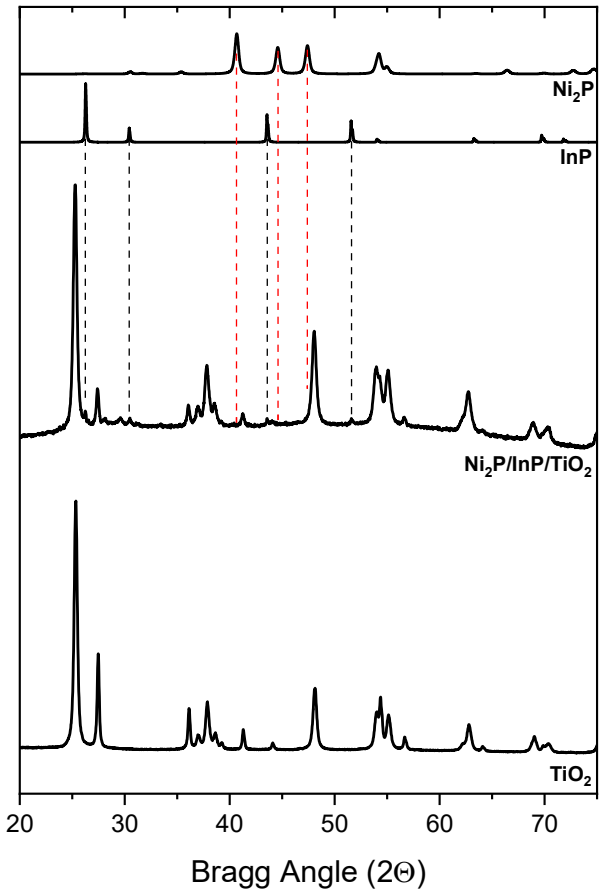

Figure 3.5.1 XRD pattern for Ni_2P-InP/TiO_2 catalyst (20 wt% Ni_2P, 10 wt% InP).

3.5.2 UV-Vis-NIR Spectroscopy

The UV-Vis absorption spectrum for the Ni_2P-InP/TiO_2 catalyst is presented in Figure 3.5.2 along with spectra for 20 wt% Ni_2P/TiO_2 and 10 wt% InP/TiO_2 catalysts for comparison. Unfortunately, separate Ni_2P and InP band gaps could not be determined due to the absorption assigned to Ni_2P and InP both appearing in the same portion of the spectrum. The combined measured band gap for Ni_2P-InP in this catalyst was measured 1.25 eV.

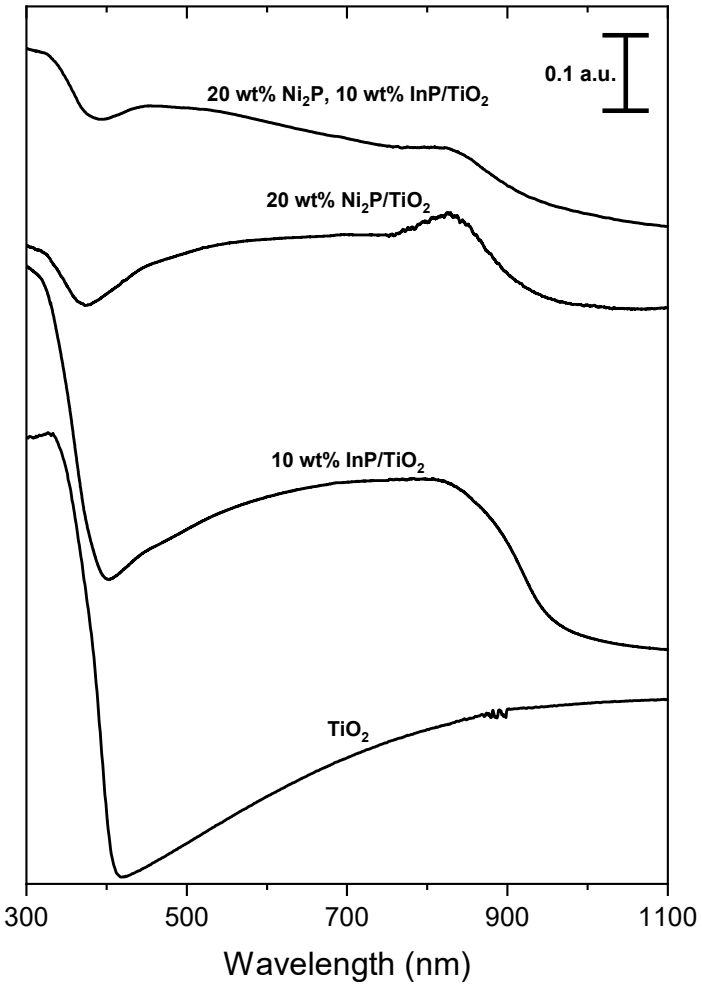

Figure 3.5.2 UV-Vis absorbance spectra of 10 wt% InP/TiO_2, 20 wt% Ni_2P/TiO_2 and Ni_2P-InP/TiO_2 (20 wt% Ni_2P, 10 wt% InP) catalysts.

Chapter 4: Discussion

The overarching goal of this thesis research was to synthesize $In_xGa_{1-x}P/TiO_2$, Ni_2P/TiO_2, and Ni_2P-$In_xGa_{1-x}P/TiO_2$ photocatalysts for the RWGS reaction. Major goals within the project included the development of a method for tuning the band gap of $In_xGa_{1-x}P$ nanoparticles on a TiO_2 support. Two methods were focused on for achieving band gap tunability. First was attempting to control the $In_xGa_{1-x}P$ particle size by varying the amount loaded onto TiO_2. Controlling particle size was not achievable with the incipient wetness impregnation technique used. The second technique that was explored was varying the In:Ga ratio in $In_xGa_{1-x}P$. Evidence summarized in this section suggests that single phase $In_xGa_{1-x}P$ has been synthesized on a TiO_2 support when x = 1.00, 0.75, 0.5, and 0.

In this thesis research, the XRD peak assigned to the (220) crystal plane of InP was shown to shift slightly towards higher Bragg angles (from 43.5° to 43.7°) as indium content was decreased from x = 1 to x = 0 in the $In_xGa_{1-x}P/TiO_2$ catalysts. Based on Vegard's law, the peak should shift linearly to 47.1° as x decreases to 0. The slight shift observed indicates that indium has been replaced by gallium in the crystal structure of InP, though not to the extent expected. XRD analysis has verified the presence of InP in the InP/TiO_2 catalysts, though the fact that no GaP peaks were observed for the GaP/TiO_2 catalyst suggests GaP is amorphous or the GaP crystallites are too small (<5 nm) to be detected by XRD.

UV-Vis spectral analysis determined band gaps for InP and GaP for the InP/TiO_2 and GaP/TiO_2 catalysts to be 1.26 and 2.26 eV, respectively, which are in agreement with the literature values of 1.35 eV for InP and 2.26 eV for GaP, suggesting the successful synthesis of InP and GaP on TiO_2.[28] Band gaps of $In_xGa_{1-x}P$ increased only slightly with increasing gallium

content (2.28 to 1.26 eV from x = 0.25 to x = 1.0, $\Delta E \approx -0.1$ eV) as compared to what was expected based on the literature (approximately 2.1 to 1.35 eV from x = 0.21 to x = 1.0, $\Delta E \approx -0.8$ eV). This small shift in band gap supports the hypothesis that gallium is being incorporated into the crystal structure of InP as expected, though not to the extent desired. The $In_{0.25}Ga_{0.75}P/TiO_2$ catalyst was determined to possess two band gaps, 2.28 and 1.36 eV, which are in agreement with literature values for GaP and InP, respectively. This suggests that some of the gallium is present as GaP and was not incorporated into the InP structure, resulting in phase segregation, although the presence of GaP was not verified by XRD.

XPS analysis identified the presence of In, Ga, and P in and probed the oxidized surface of the $In_xGa_{1-x}P$ nanoparticles in the $In_xGa_{1-x}P/TiO_2$ catalysts. Ga($2p_{3/2}$) and In($3d_{5/2}$) peaks were shown to range from 1118.0-1118.6 eV, and 444.6-445.0 eV, respectively, for the $In_xGa_{1-x}P/TiO_2$ catalysts, agreeing very well with the literature values found for Ga_2O_3 (1118.1 and 1118.3 eV) [40,43] and In_2O_3 (444.5 eV).[37] The trend found towards slightly lower Ga binding energies as indium content increased in the $In_xGa_{1-x}P/TiO_2$ catalysts is consistent with the fact that indium has a lower electronegativity than gallium (1.78 vs. 1.81, respectively).[46] This general trend was also shown in the binding energies of the indium atoms; higher gallium content results in higher binding energies as a result of the increased population of the higher electronegativity gallium atoms attracts more electron density than the indium atoms.

XRD patterns confirm the presence of Ni_2P nanocrystals the TiO_2 support. EDS analysis further confirmed the presence of Ni and P in the Ni_2P/TiO_2 catalysts with loadings of 2.5-20 wt% Ni_2P. Literature values for Ni($2p_{3/2}$) binding energies in Ni_2P have been reported to at least vary in the 852.2 to 856.03 eV range (for Ni^{2+} and $Ni^{\delta+}$), overlapping significantly with results found here (852.6 to 857.6 eV).[15,45,47] The peak found to vary between 858.9 and 862.9 eV

corresponds to the oxidized Ni_2P species, reported in the literature to vary between 856.9 and 865.1 eV.[15,45,47] UV-Vis analysis determined Ni_2P band gaps that ranged from 1.1 to 1.3 eV, just above the 1.0 eV that is expected based on literature results for as-prepared "bulk" Ni_2P (in powder form).[15,20]

XRD results have verified the presence of InP crystallites, though the lack of Ni_2P diffraction peaks lead to inconclusive results with respect to the presence of Ni_2P in the Ni_2P-InP/TiO_2 catalyst. UV-Vis analysis determined a band gap of 1.25 eV for the Ni_2P-InP/TiO_2 catalyst (20 wt% Ni_2P, 10 wt% InP), which is consistent with what has been found here for Ni_2P/TiO_2 catalysts (1.1-1.3 eV) and InP/TiO_2 catalysts (1.19-1.28 eV). Future directions for this project should involve the synthesis of a Ni_2P-InP/TiO_2 catalyst with a much higher loading of Ni_2P (25 wt% or higher), in order to confirm the coexistence of InP and Ni_2P crystallites on TiO_2 via XRD and to perform heterogeneous photocatalytic testing to determine the efficiency of this system towards the RWGS reaction.

Chapter 5: Conclusions

$In_xGa_{2-x}O_3/TiO_2$, the precursors for $In_xGa_{1-x}P/TiO_2$, were synthesized onto TiO_2 (In_2O_3/TiO_2). Two band gaps were measured for each of the $In_xGa_{2-x}O_3/TiO_2$ catalysts, 2.88-2.91 eV and 2.90-3.00 eV, attributed to $In_xGa_{2-x}O_3$ species and TiO_2, respectively. $In_xGa_{x-1}P/TiO_2$ catalysts were produced upon reduction of the $In_xGa_{2-x}O_3/TiO_2$ precursor series, though characterization results suggest that gallium has not been incorporated into the crystal structure of InP to the extent intended. Band gaps of $In_xGa_{x-1}P$ in the $In_xGa_{1-x}P/TiO_2$ catalysts were tuned from 1.26 to 2.26 eV by varying x between 1 and 0.

Ni_2P nanoparticles (7-15 nm) have been loaded onto TiO_2 to produce a series of Ni_2P/TiO_2 catalysts ranging from 2.5 to 20 wt% Ni_2P. The Ni_2P nanoparticles in 20 wt% Ni_2P/TiO_2 catalyst were determined to have a band gap of 1.2 eV. This is expected to be the most reliable measurement, due to the absorption spectrum having the most pronounced Ni_2P absorbance slope.

Ni_2P was attempted to be synthesized directly onto an InP/TiO_2 catalyst to produce a Ni_2P-InP/TiO_2 catalyst (20 wt% Ni_2P, 10 wt% InP). Verification of InP/TiO_2 was achieved, though the question as to the presence Ni_2P was inconclusive. A band gap of 1.25 eV was measured for the Ni_2P-InP/TiO_2 catalyst. Synthesis of Ni_2P-InP/TiO_2 catalysts should be done with Ni_2P and InP loadings at least in the range of 1-25 wt%. The resulting series of Ni_2P-InP/TiO_2 catalysts should be characterized via XRD, UV-Vis, EDS, and XPS. These Ni_2P-InP/TiO_2 catalysts and all catalysts presented in this document should be subjected to RWGS testing to probe their heterogeneous photocatalytic viability.

References

1. Hosseini, S. E.; Wahid, M. A. Utilization of Palm Solid Residue as a Source of Renewable and Sustainable Energy in Malaysia. *Renew. Sust. Energ. Rev.* **2014**, 40, 621–632.
2. Daza, Y. A.; Kuhn, J. N. CO_2 Conversion by Reverse Water Gas Shift Catalysis: Comparison of Catalysts, Mechanisms and Their Consequences for CO_2 Conversion to Liquid Fuels. *RSC Advances* **2016**, 6, 49675–49691.
3. Schneider, S. H.; Mastrandrea, M. D. Probabilistic assessment of ‘‘dangerous’’ climate change and emissions pathways. *PNAS*, **2005**, 102, 15728-15735.
4. Bhore, S. Paris Agreement on Climate Change: A Booster to Enable Sustainable Global Development and Beyond. *Int. J. Environ. Res. Public Health* **2016**, *13*, 1134.
5. Wang, Y.; Sun, G. J.; Zhang, F.; Qi, J.; Zhao, C. Y. Modeling Impacts of Farming Management Practices on Greenhouse Gas Emissions in the Oasis Region of China. *Biogeosciences* **2011**, *8*, 2377–2390.
6. The Atmosphere: Getting a Handle on Carbon Dioxide – Climate Change: Vital Signs of the Planet. https://climate.nasa.gov/news/2915/the-atmosphere-getting-a-handle-on-carbon-dioxide/ (accessed Apr 28, 2020).
7. Arora, S.; Prasad, R. An Overview on Dry Reforming of Methane: Strategies to Reduce Carbonaceous Deactivation of Catalysts. *RSC Adv.* **2016**, *6*, 108668–108688.
8. Bustamante, F.; Enick, R. M.; Cugini, A.; Killmeyer, R. P.; Howard, B. H.; Rothenberger, K. S.; Ciocco, M. V.; Morreale, B. D.; Chattopadhyay, S.; Shi, S. High-Temperature Kinetics of the Homogeneous Reverse Water-Gas Shift Reaction. *AIChE J.* **2004**, *50*, 1028–1041.
9. Kirk, R. E.; Othmer, D. F. *Encyclopedia of Chemical Technology*; John Wiley & Sons: New York, 1991.
10. Tahir, M.; Amin, N. A. S. Photo-Induced CO_2 Reduction by Hydrogen for Selective CO Evolution in a Dynamic Monolith Photoreactor Loaded with Ag-Modified TiO_2 Nanocatalyst. *Int. J. Hydrog. Energy* **2017**, *42*, 15507–15522.

11. rivastava, V.; Kamysbayev, V.; Hong, L.; Dunietz, E.; Klie, R. F.; Talapin, D. V. Colloidal Chemistry in Molten Salts: Synthesis of Luminescent $In_{1-X}Ga_xP$ and $In_{1-X}Ga_x$ As Quantum Dots. *J. Am. Chem. Soc.* **2018**, 140, 12144–12151.
12. Jia, J.; Wang, H.; Lu, Z.; Obrien, P. G.; Ghoussoub, M.; Duchesne, P.; Zheng, Z.; Li, P.; Qiao, Q.; Wang, L.; Gu, A.; Jelle, A. A.; Dong, Y.; Wang, Q.; Ghuman, K. K.; Wood, T.; Qian, C.; Shao, Y.; Qiu, C.; Ye, M.; Zhu, Y.; Lu, Z.-H.; Zhang, P.; Helmy, A. S.; Singh, C. V.; Kherani, N. P.; Perovic, D. D.; Ozin, G. A. Photothermal Catalyst Engineering: Hydrogenation of Gaseous CO_2 with High Activity and Tailored Selectivity. *Adv. Sci.* **2017**, 4, 1700252.
13. Ghoussoub, M.; Xia, M.; Duchesne, P. N.; Segal, D.; Ozin, G. Principles of Photothermal Gas-Phase Heterogeneous CO_2 Catalysis. *Energy Environ. Sci.* **2019**, *12*, 1122–1142.
14. Upadhye, A. A.; Ro, I.; Zeng, X.; Kim, H. J.; Tejedor, I.; Anderson, M. A.; Dumesic, J. A.; Huber, G. W. Plasmon-Enhanced Reverse Water Gas Shift Reaction over Oxide Supported Au Catalysts. *Catal. Sci. Technol.* **2015**, *5*, 2590–2601.
15. Shiraishi, Y.; Chishiro, K.; Tanaka, S.; Hirai, T. Photocatalytic Dinitrogen Reduction with Water on Boron-Doped Carbon Nitride Loaded with Nickel Phosphide Particles. *Langmuir* **2020**, 36, 734–741.
16. Sun, Z.; Zheng, H.; Li, J.; Du, P. Extraordinarily Efficient Photocatalytic Hydrogen Evolution in Water Using Semiconductor Nanorods Integrated with Crystalline Ni_2P Cocatalysts. *Energy Environ. Sci.* **2015**, *8*, 2668–2676.
17. Chen, Y.; Qin, Z. General Applicability of Nanocrystalline Ni_2P as a Noble-Metal-Free Cocatalyst to Boost Photocatalytic Hydrogen Generation. *Catal. Sci. Technol.* **2016**, 6, 8212–8221.
18. Guharoy, U.; Reina, T. R.; Gu, S.; Cai, Q. Mechanistic Insights into Selective CO_2 Conversion via RWGS on Transition Metal Phosphides: A DFT Study. *J. Phys. Chem. C* **2019**, *123*, 22918–22931.
19. Zhen, W.; Ning, X.; Yang, B.; Wu, Y.; Li, Z.; Lu, G. The enhancement of CdS photocatalytic activity for water splitting via anti-photocorrosion by coating Ni_2P shell and removing nascent formed oxygen with artificial gill. *Appl. Catal. B* **2018**, 221, 243–257

20. M. Sharon; G. Tamizhmani; C. Levy-Clement; J. Rioux; Study of electrochemical and photoelectrochemical properties of nickel phosphide semiconductors. *Sol. Cells* **1989**, 26, 303-312.
21. Goossens, A. An Impedance Study of Boron Phosphide Semiconductor Electrodes. *J. Electrochem. Soc.* **1992**, 139, 893-900.
22. Xu, Y.; Schoonen, M. A. The Absolute Energy Positions of Conduction and Valence Bands of Selected Semiconducting Minerals. *Am. Mineral.* **2000**, 85, 543–556.
23. Inoue, T.; Fujishima, A.; Konishi, S.; Honda, K. Photoelectrocatalytic Reduction of Carbon Dioxide in Aqueous Suspensions of Semiconductor Powders. *Nature* **1979**, 277, 637–638.
24. Chen, T.; Ding, J.; Liu, T.; Li, Q.; Luo, Y.; Dong, L.; Du, H.; Fang, M.; Bao, J.; Wu, Y. Two Anionic Ni(II) Porphyrinic Metal−Organic Frameworks: Syntheses, Flexibility and Roles in Visible-Light Photocatalytic CO_2 Reduction to CO in the $Ru(Bpy)_3Cl_2$/TEA/CH_3CN System. *J. Solid State Chem.* **2020**, 287, 121340.
25. Hoch, L. B.; O'Brien, P. G.; Jelle, A.; Sandhel, A.; Perovic, D. D.; Mims, C. A.; Ozin, G. A. Nanostructured Indium Oxide Coated Silicon Nanowire Arrays: A Hybrid Photothermal/Photochemical Approach to Solar Fuels. *ACS Nano* **2016**, 10, 9017–9025.
26. Makita, H.; Hastings, G. Inverted-Region Electron Transfer as a Mechanism for Enhancing Photosynthetic Solar Energy Conversion Efficiency. *PNAS* **2017**, 114 9267–9272.
27. Tamang, S.; Lincheneau, C.; Hermans, Y.; Jeong, S.; Reiss, P. Chemistry of InP Nanocrystal Syntheses. *Chem. Mater.* **2016**, *28*, 2491–2506.
28. Kornienko, N.; Whitmore, D. D.; Yu, Y.; Leone, S. R.; Yang, P. Correction to Solution Phase Synthesis of Indium Gallium Phosphide Alloy Nanowires. *ACS Nano.* **2015**, *9*, 3951-3960.
29. Grazulis, S.; Chateigner, D.; Downs, R. T.; Yokochi, A. T.; Quiros, M.; Lutterotti, L.; Manakova, E.; Butkus, J.; Moeck, P.; Le Bail, A. Crystallography Open Database – an open-access collection of crystal structures. *J. Appl. Cryst.* **2009**, 42, 726-729.
30. Halder, N. C.; Wagner, C. N. J. Separation of particle size and lattice strain in integral breadth measurements. *Acta. Cryst.* **1966**, 20, 312-313.

31. López, R.; Gómez, R. Band-Gap Energy Estimation from Diffuse Reflectance Measurements on Sol–Gel and Commercial TiO_2: A Comparative Study. *J. Sol-Gel Sci. Technol.* **2011**, 61, 1–7.
32. Scanlon, D. O.; Dunnill, C. W.; Buckeridge, J.; Shevlin, S. A.; Logsdail, A. J.; Woodley, S. M.; Sokol, A. A. Band alignment of rutile and anatase TiO_2. *Nat. Mater.* **2013**, 12, 798-801.
33. Alonso-Telleza, A.; Massona, R.; Robertb, D.; Kellera, N.; Keller, V. Comparison of Hombikat UV100 and P25 TiO_2 performance in gas-phase photocatalytic oxidation reactions. *J. Photochem. Photobiol. A.* **2012**, 250, 58-65.
34. Zhou, X.; Wu, J.; Li, Q.; Zeng, T.; Ji, Z.; He, P.; Pan, W.; Qi, X.; Wang, C.; Liang, P. Carbon decorated In_2O_3/TiO_2 heterostructures with enhanced visiblelight-driven photocatalytic activity. *J. Catal.* **2017**, 355, 26-39.
35. Scanlon, D. O.; Dunnill, C. W.; Buckeridge, J.; Shevlin, S. A.; Logsdail, A. J.; Woodley, S. M.; Catlow, C. R. A.; Powell, M. J.; Palgrave, R. G.; Parkin, I. P.; Watson, G. W.; Keal, T. W.; Sherwood, P.; Walsh, A,; Sokol, A. A. Band alignment of rutile and anatase TiO_2. *Nat. Mater.* **2013**, 12, 798-801.
36. Farvid, S. S.; Wang, T.; Radovanovic, P. V. Colloidal Gallium Indium Oxide Nanocrystals: A Multifunctional Light-Emitting Phosphor Broadly Tunable by Alloy Composition. *J. Am. Chem. Soc.* **2011**, 133, 6711–6719.
37. Li, C.; Ming, T.; Wang, J.; Wang, J.; Yu, J. C.; Yu, S. Ultrasonic aerosol spray-assisted preparation of TiO_2/In_2O_3 composite for visible-light-driven photocatalysis. *J. Catal.* **2014**, 310, 84-90.
38. Zhang, X.; Ptasinska, S. Distinct and dramatic water dissociation on GaP(111) tracked by near-ambient pressure X-ray photoelectron spectroscopy. *Phys. Chem. Chem. Phys.* **2015**, 17, 3909-3918.
39. Zhang, X.; Lamere, E.; Liu, X. Furdyna, J. K.; Ptasinska, S. Morphology dependence of interfacial oxidation states of gallium arsenide under near ambient conditions. *Appl. Phys. Lett.* **2014**, 104, 181602.
40. Ishikawa, T.; Ikoma, H. X-Ray Photoelectron Spectroscopy Analysis of the Oxide of GaAs. *Jpn. J. Appl. Phys.* **1992**, 31, 3981-3987.

41. Kumar, V.; Jha, V.; Shrivastava, A. K. Debye temperature and melting point of II-VI and III-Vsemiconductors. *Cryst. Res. Technol.* **2010**, 45, 920-924.
42. Lisachenko, A. A.; Kuznetsov, V. N.; Zakharov, M. N.; Mikhailov, R. V. The Interaction of O_2, NO, and N_2O with Surface Defects of Dispersed Titanium Dioxide. *Kinet. Catal.* **2004**, 45, 189-197.
43. Wei, S.; Lu, J.; Zeng, L.; Yu, W.; Qian, Y.; Hydrothermal Synthesis of InP Semiconductor Nanocrystals. *Chem. Lett.*, **2002**, 10, 1034-1035
44. Balasubramanian, S.; Gopinathl, C. S.; Subramaniant, S.; Balasubramanian, N. Exposure of InP to hydrogen plasma in the presence of a 'sacrificial' InP-an x-ray photoelectron spectroscopic study. *Semicond. Sci. Technol.*, **1994**, 9, 1604-1607.
45. Liang, G.; Waqas, G.; Yang, B.; Xiao, K.; Li, J.; Zhu, C.; Zhang, J.; Duan, H. Enhanced photocatalytic hydrogen evolution under visible light irradiation by p-type MoS_2/n-type Ni_2P doped g-C_3N_4. *Appl. Surf. Sci.* **2020**, 504, 144448.
46. Allen, L. C. Electronegativity Is the Average One-Electron Energy of the Valence-Shell Electrons in Ground-State Free Atoms. *J. Am. Chem. Soc.* **1989**, 111, 9003-9014.
47. Li, J.; Xin, X.; Li, Y.; Zhang, F.; Anpo, M.; Xu, Y. Visible light-induced conversion of biomass-derived chemicals integrated with hydrogen evolution over 2D Ni_2P–graphene–TiO_2. *Res. Chem. Intermed.* **2019**, 45, 5935-5946.

Appendix A

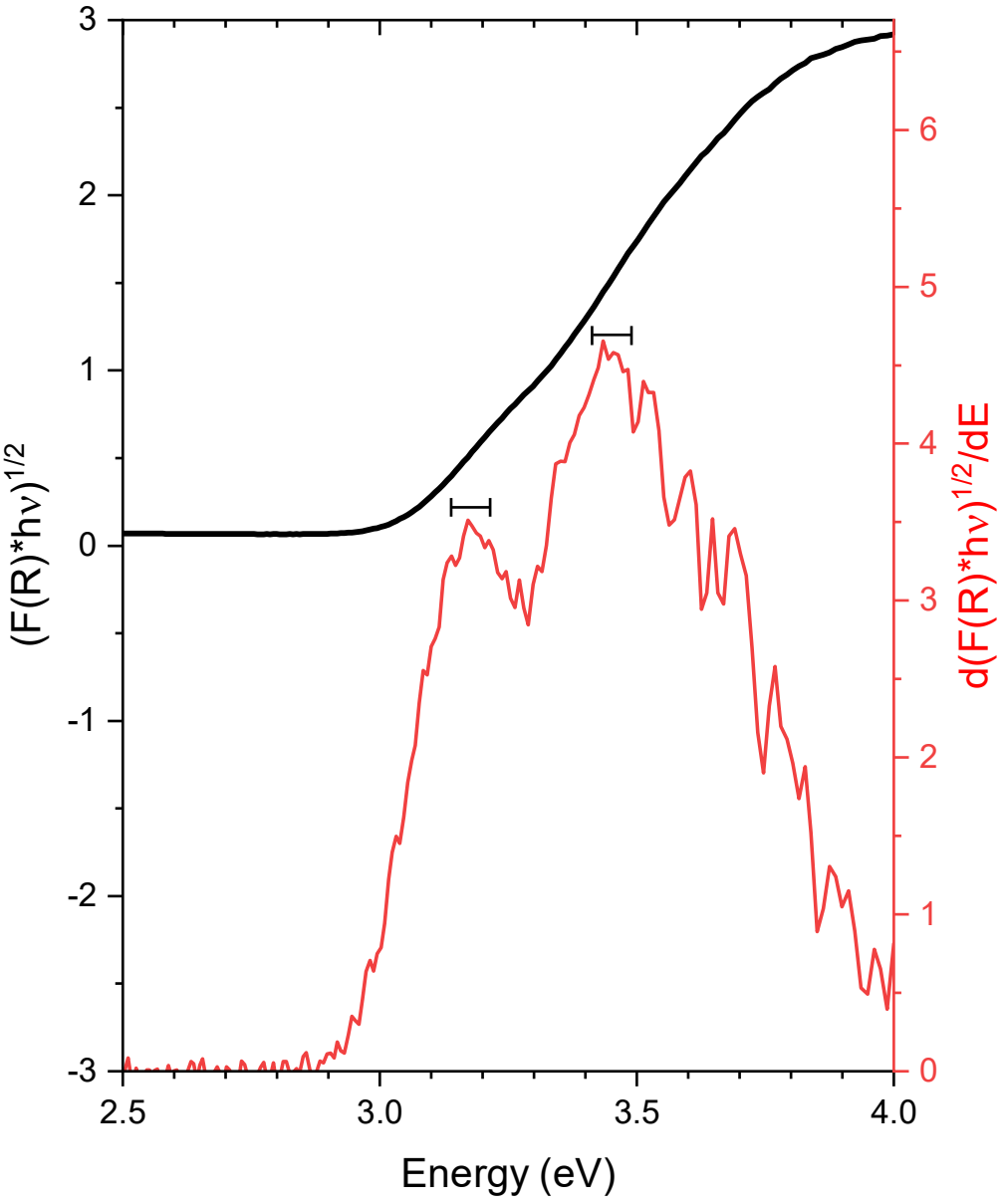

Figure A.1 Superposition of the Tauc plot (black) for TiO_2 and its derivative (red).

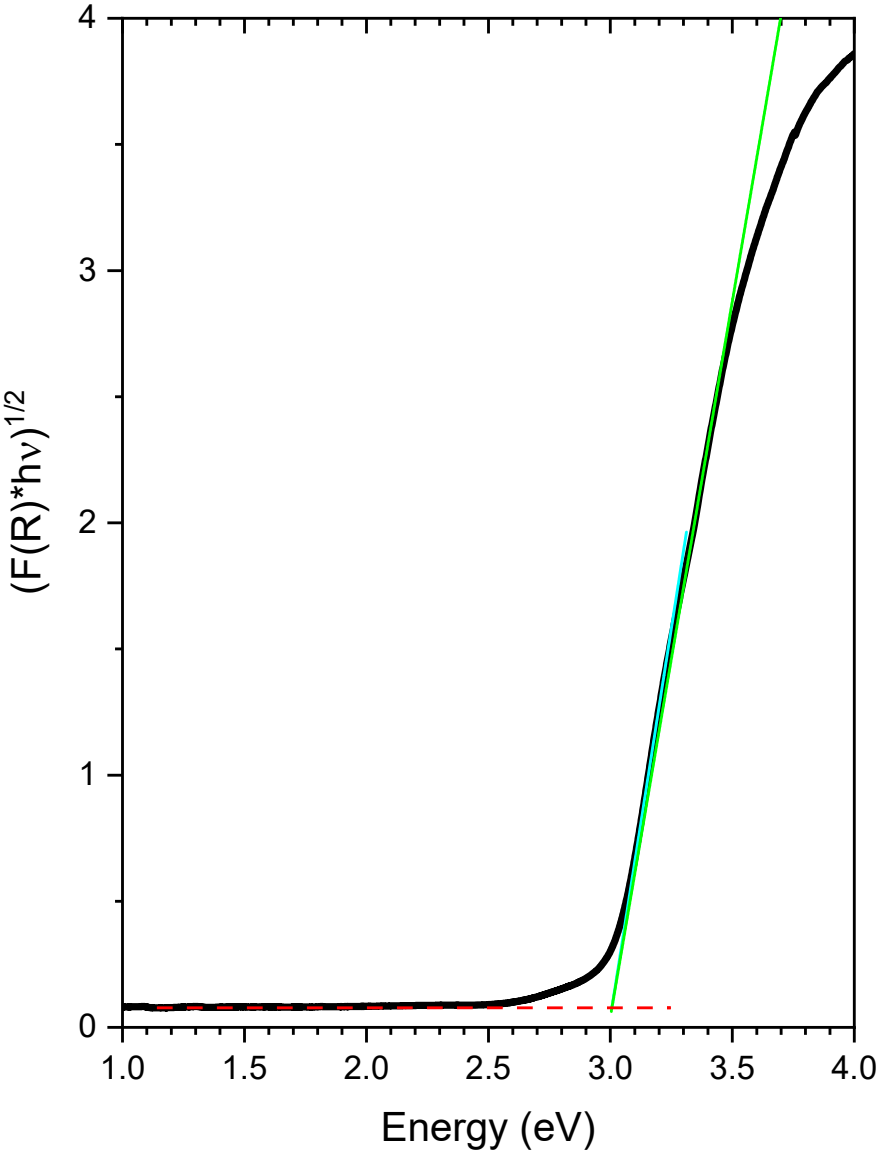

Figure A.2 Tauc plot analysis for determining the band gap of In_2O_3 in 5 wt% In_2O_3/TiO_2.

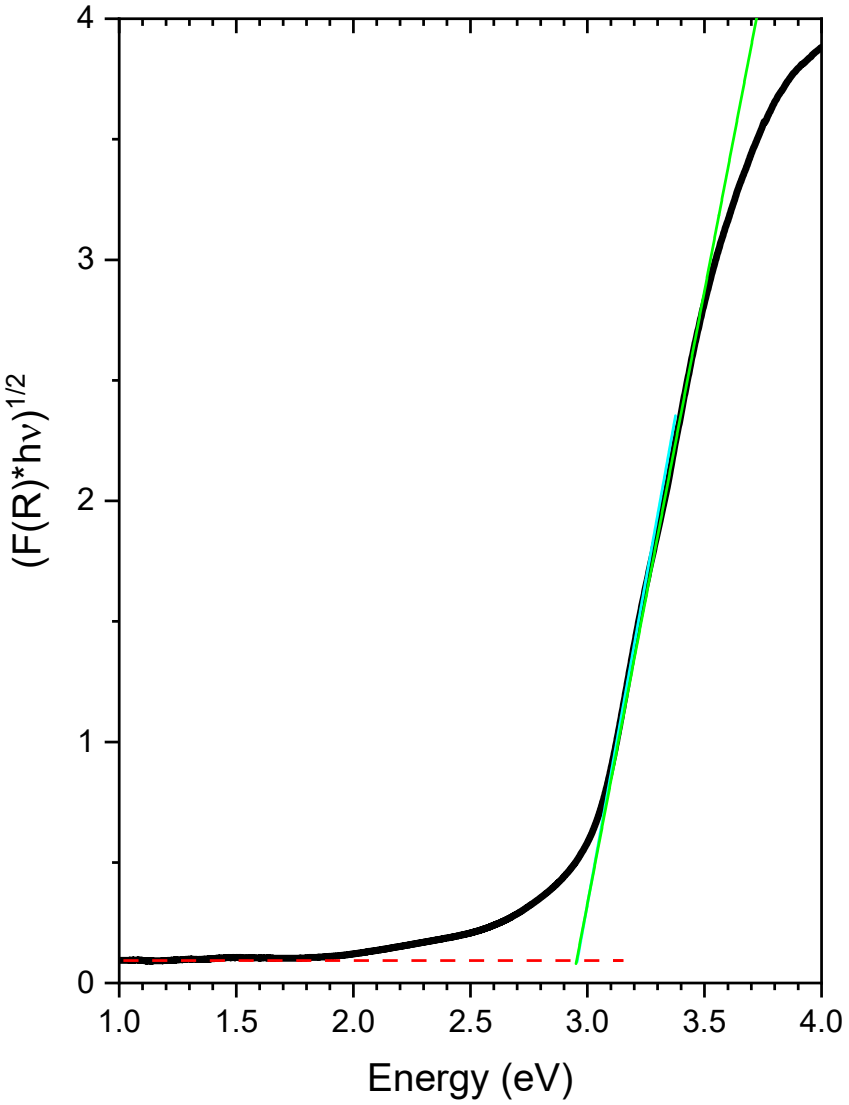

Figure A.3 Tauc plot analysis for determining the band gap of In_2O_3 in 10 wt% In_2O_3/TiO_2.

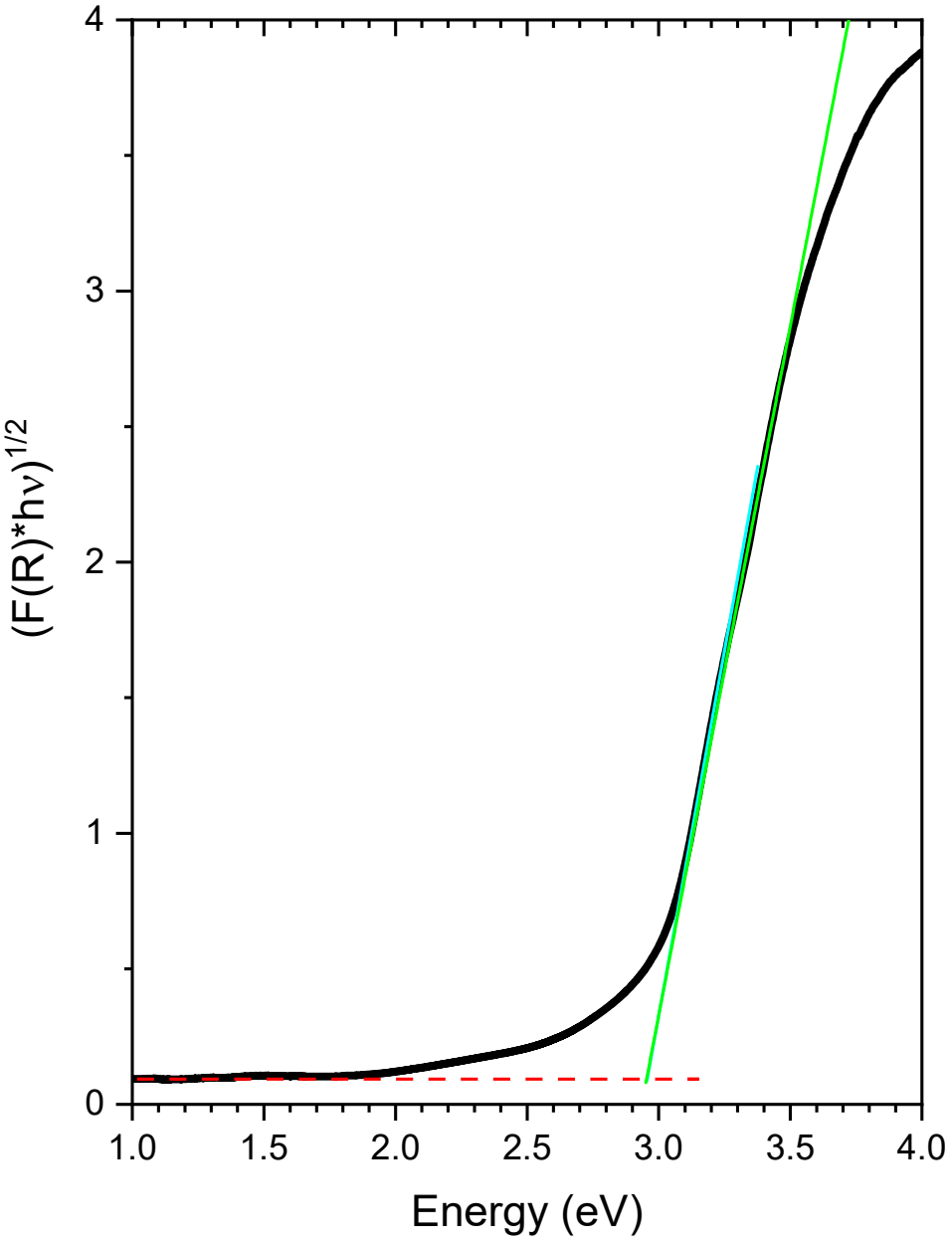

Figure A.4 Tauc plot analysis for determining the band gap of In_2O_3 in 15 wt% In_2O_3/TiO_2.

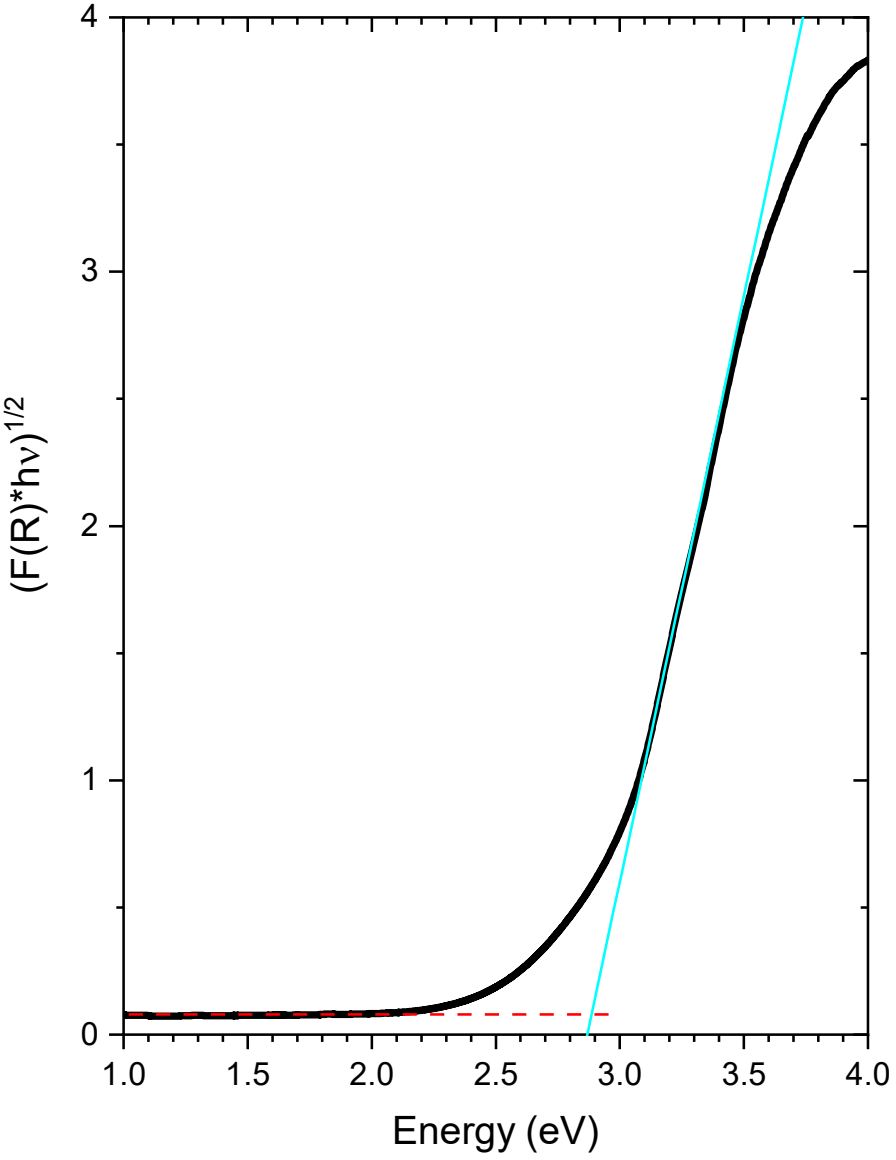

Figure A.5 Tauc plot analysis for determining the band gap of In_2O_3 in 20 wt% In_2O_3/TiO_2.

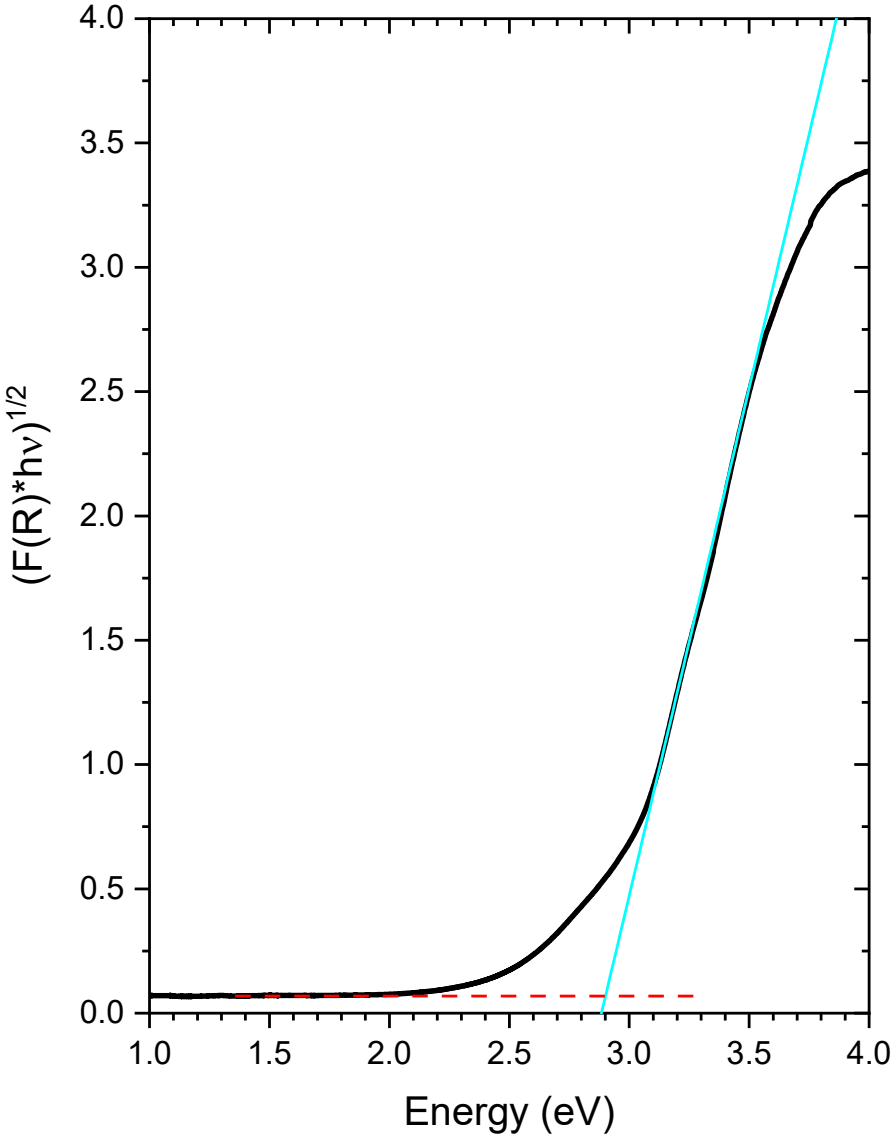

Figure A.6 Tauc plot analysis for determining the band gap of $In_{1.5}Ga_{0.5}O_3$ in 20 wt% $In_{1.5}Ga_{0.5}O_3/TiO_2$.

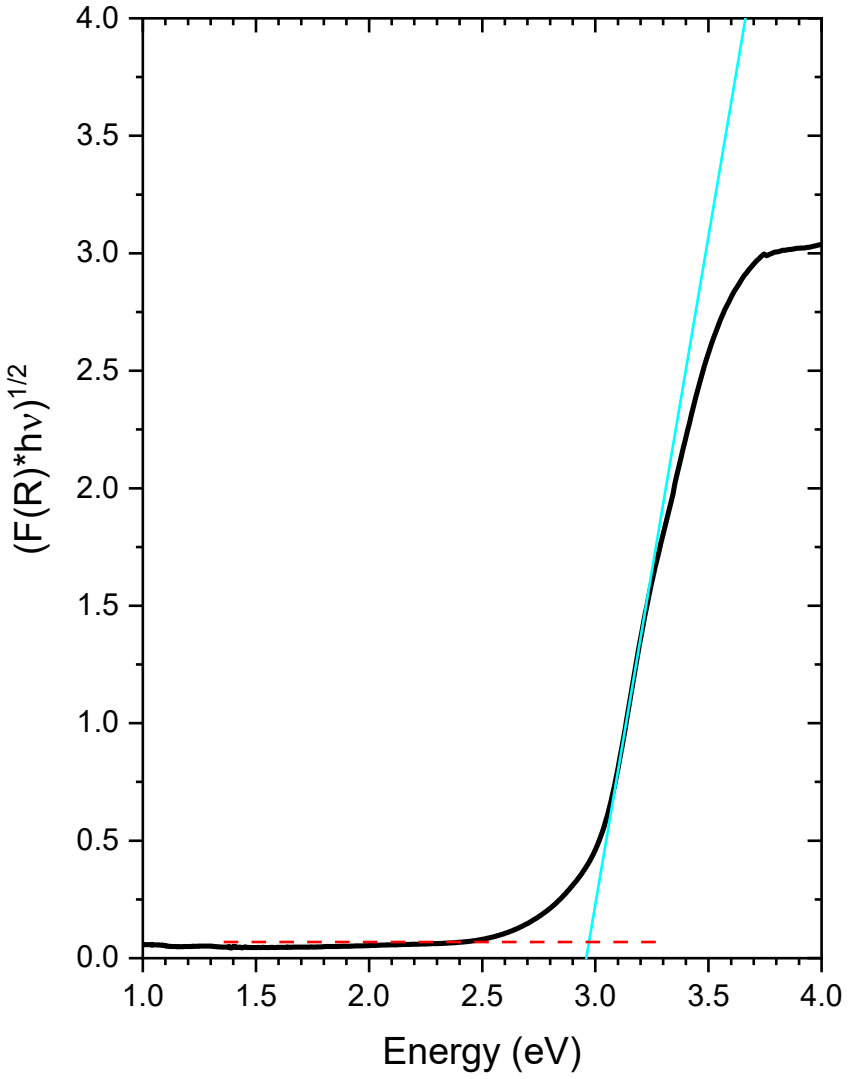

Figure A.7 Tauc plot analysis for determining the band gap of $InGaO_3$ in 20 wt% $InGaO_3/TiO_2$.

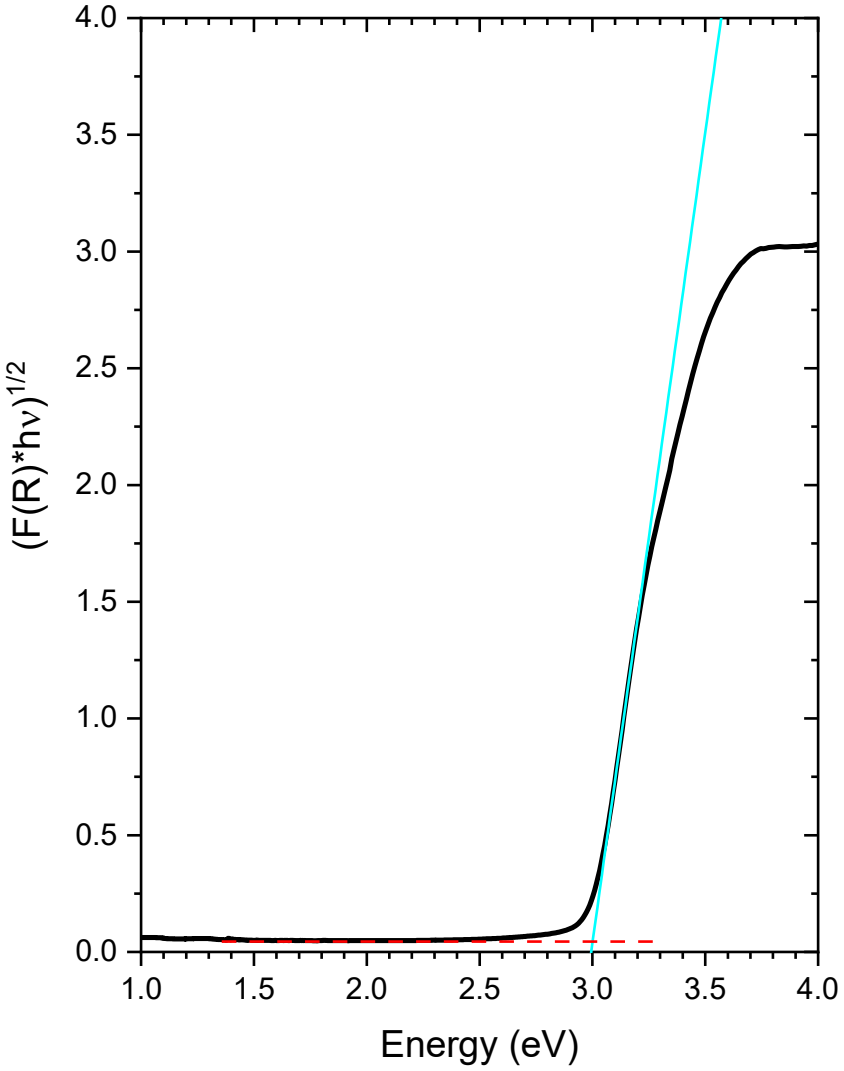

Figure A.8 Tauc plot analysis for determining the band gap of $In_{0.5}Ga_{1.5}O_3$ in 20 wt% $In_{0.5}Ga_{1.5}O_3/TiO_2$.

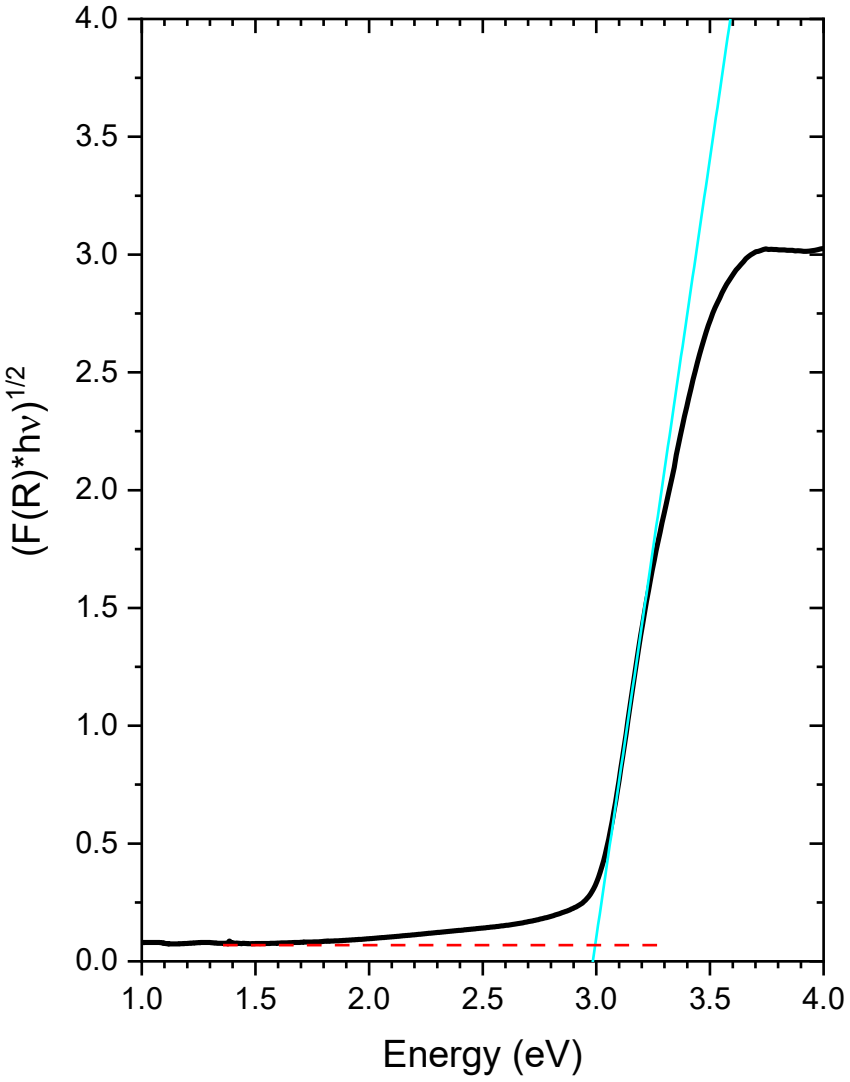

Figure A.9 Tauc plot analysis for determining the band gap of Ga_2O_3 in 20 wt% Ga_2O_3/TiO_2.

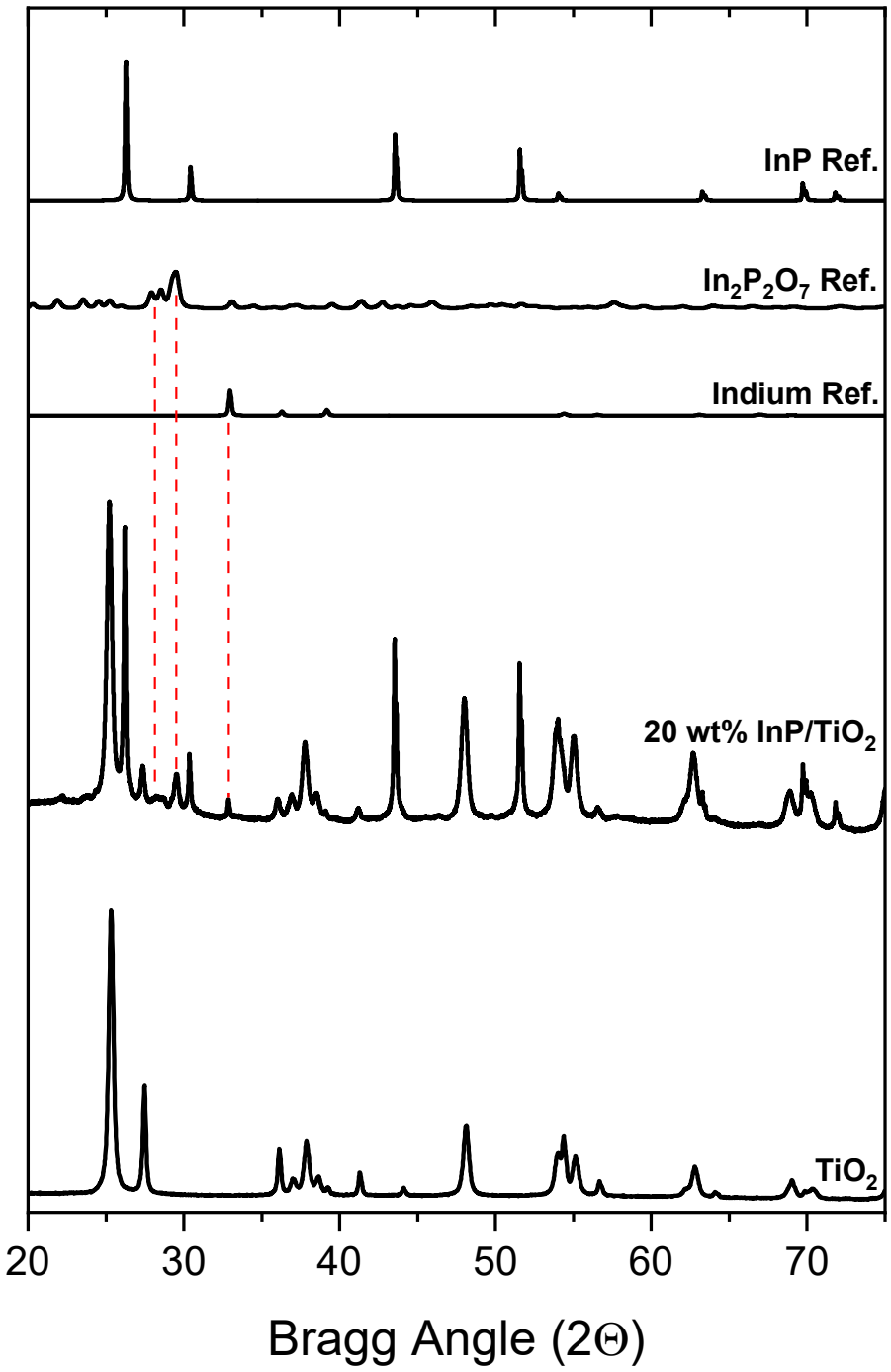

Figure A.10 Stacked XRD plot showing identification of In and $In_2P_2O_7$ impurities in InP/TiO_2.

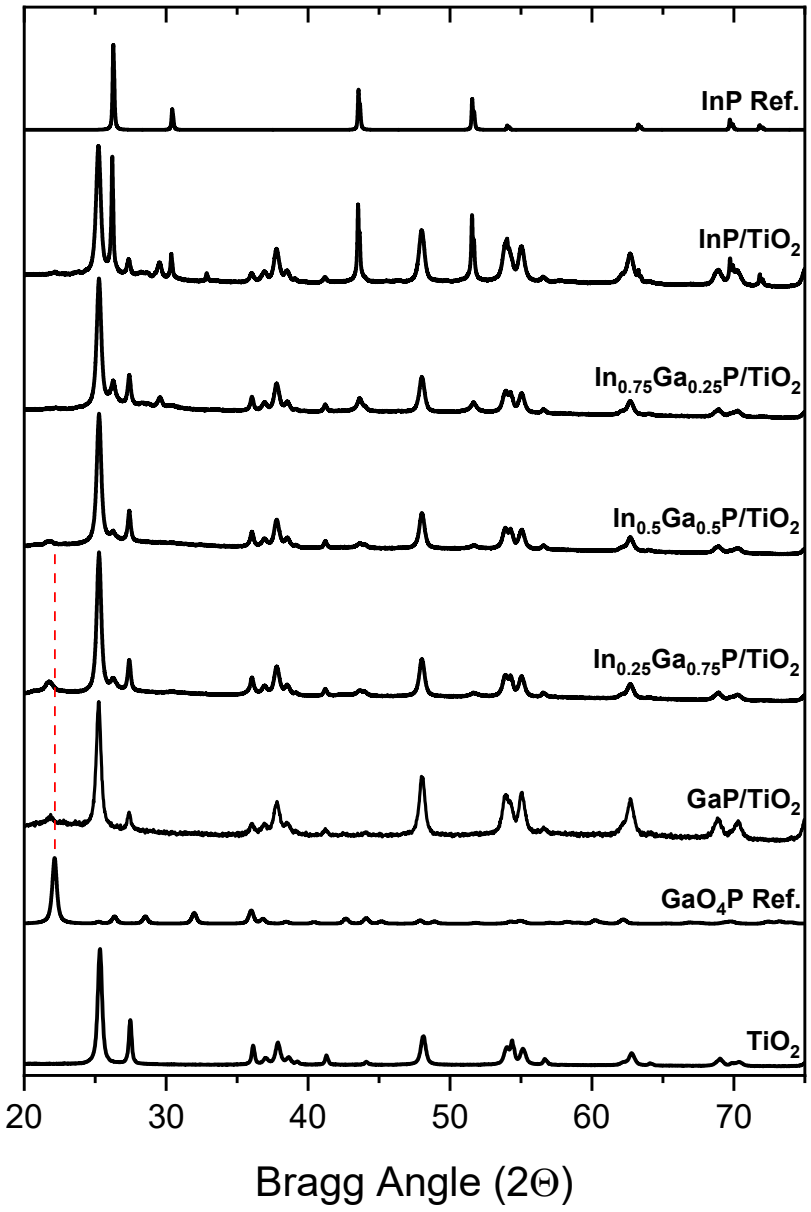

Figure A.11 Stacked XRD plot showing possible identification of GaO_4P impurity.

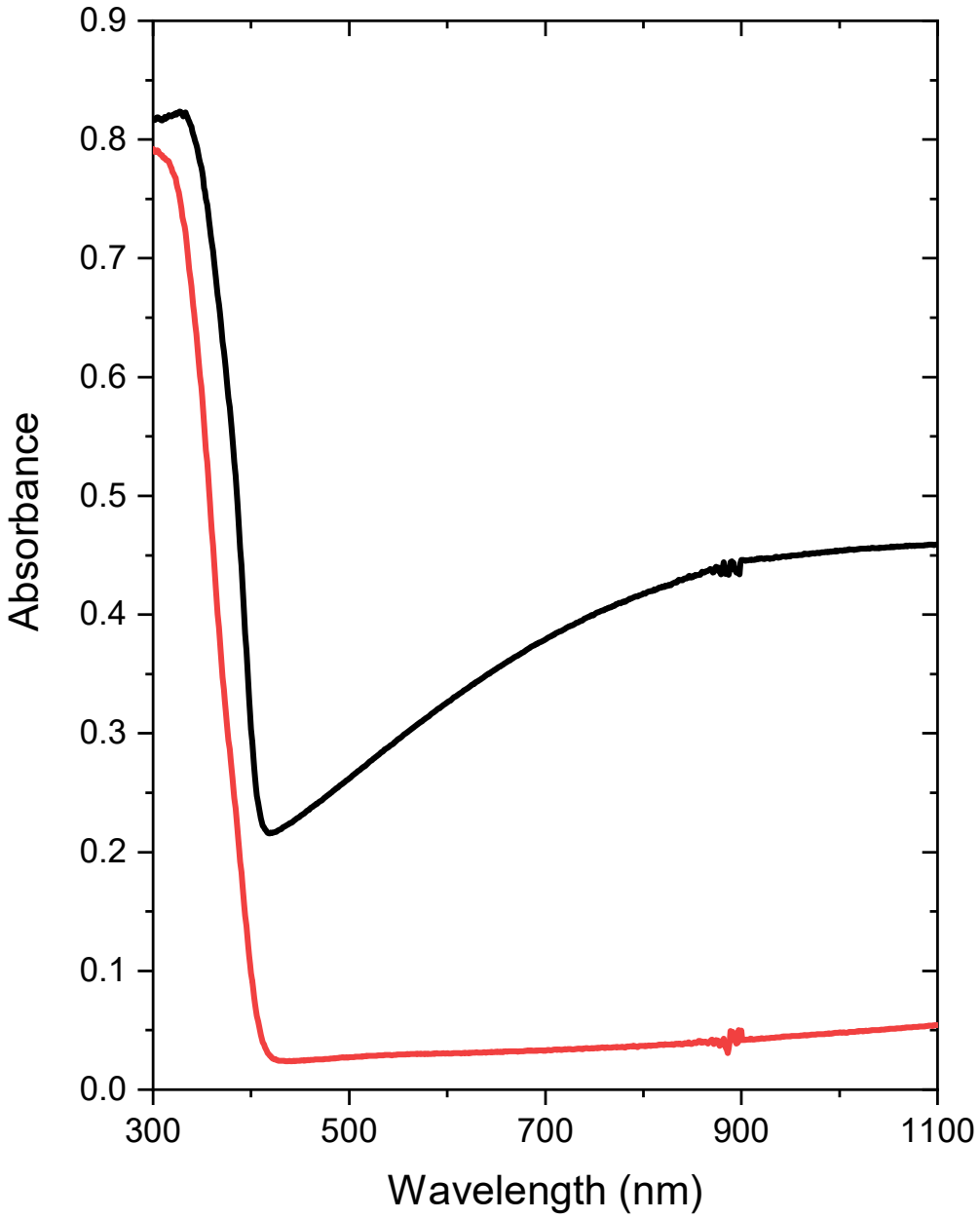

Figure A.12 Absorption spectra comparing the spectrum for TiO_2 (red) with the spectrum of reduced TiO_2 (black). TiO_2 was reduced in flowing hydrogen at 873 K.

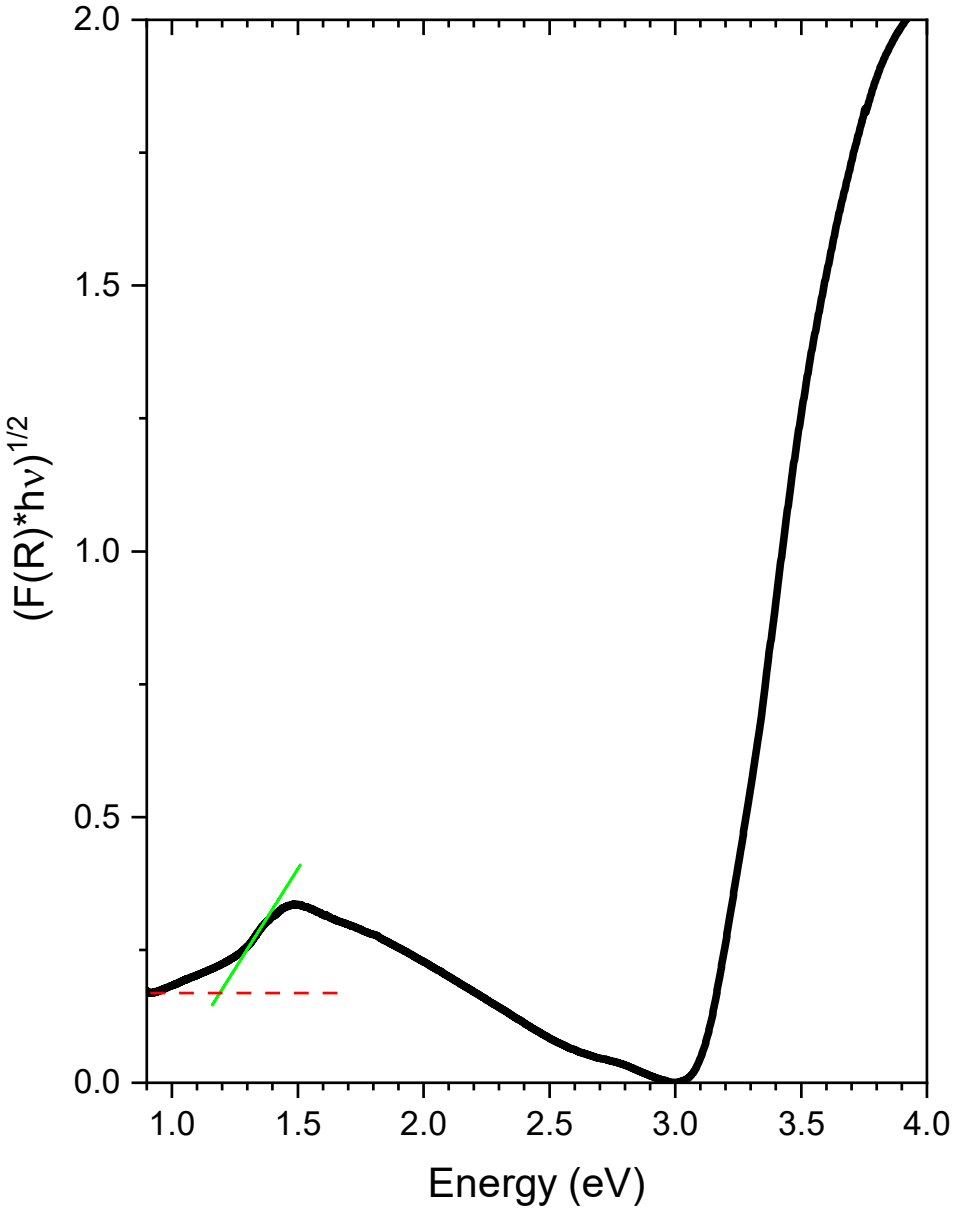

Figure A.13 Tauc plot analysis for determining the band gap of InP in 5 wt% InP/TiO_2.

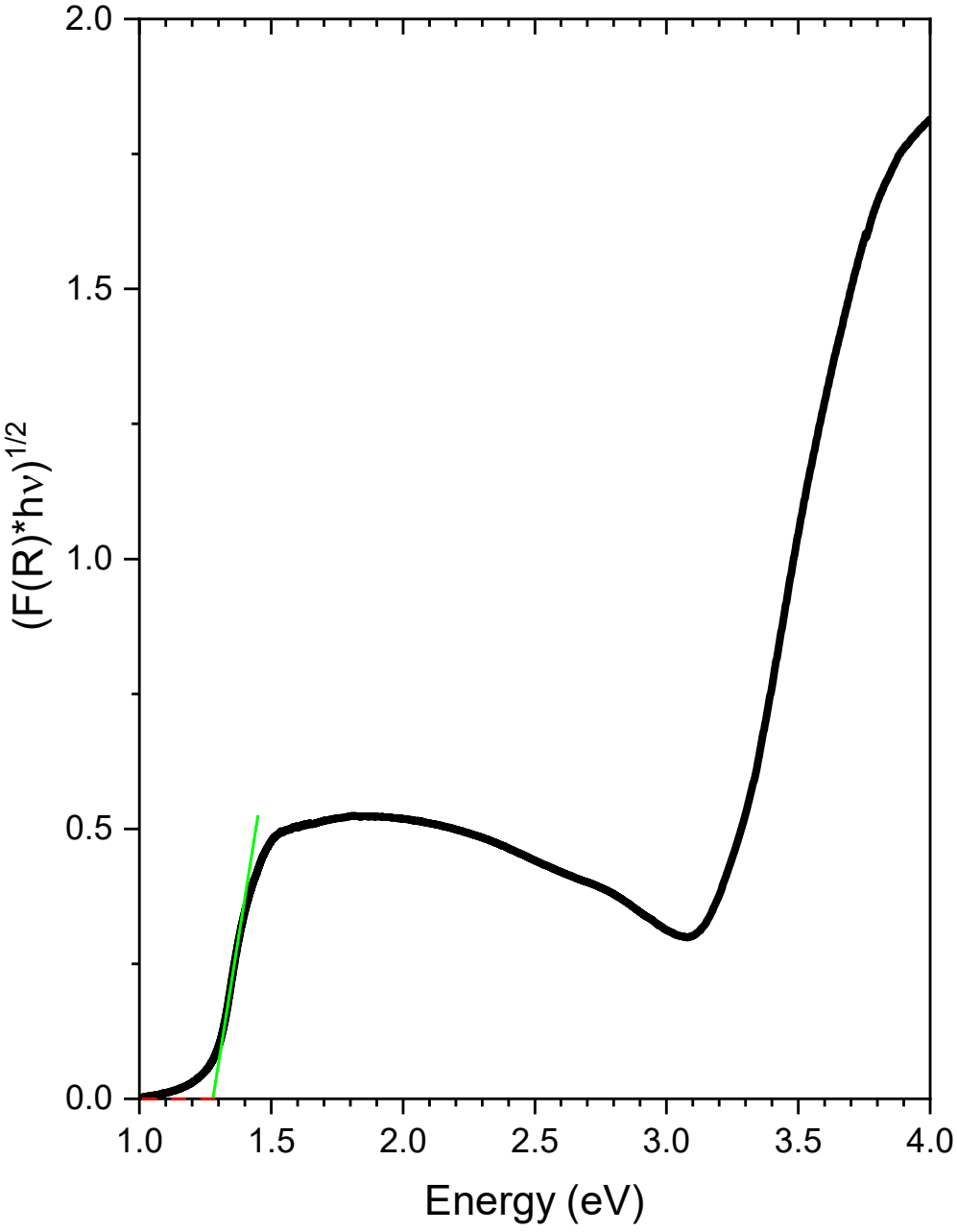

Figure A.14 Tauc plot analysis for determining the band gap of InP in 10 wt% InP/TiO_2.

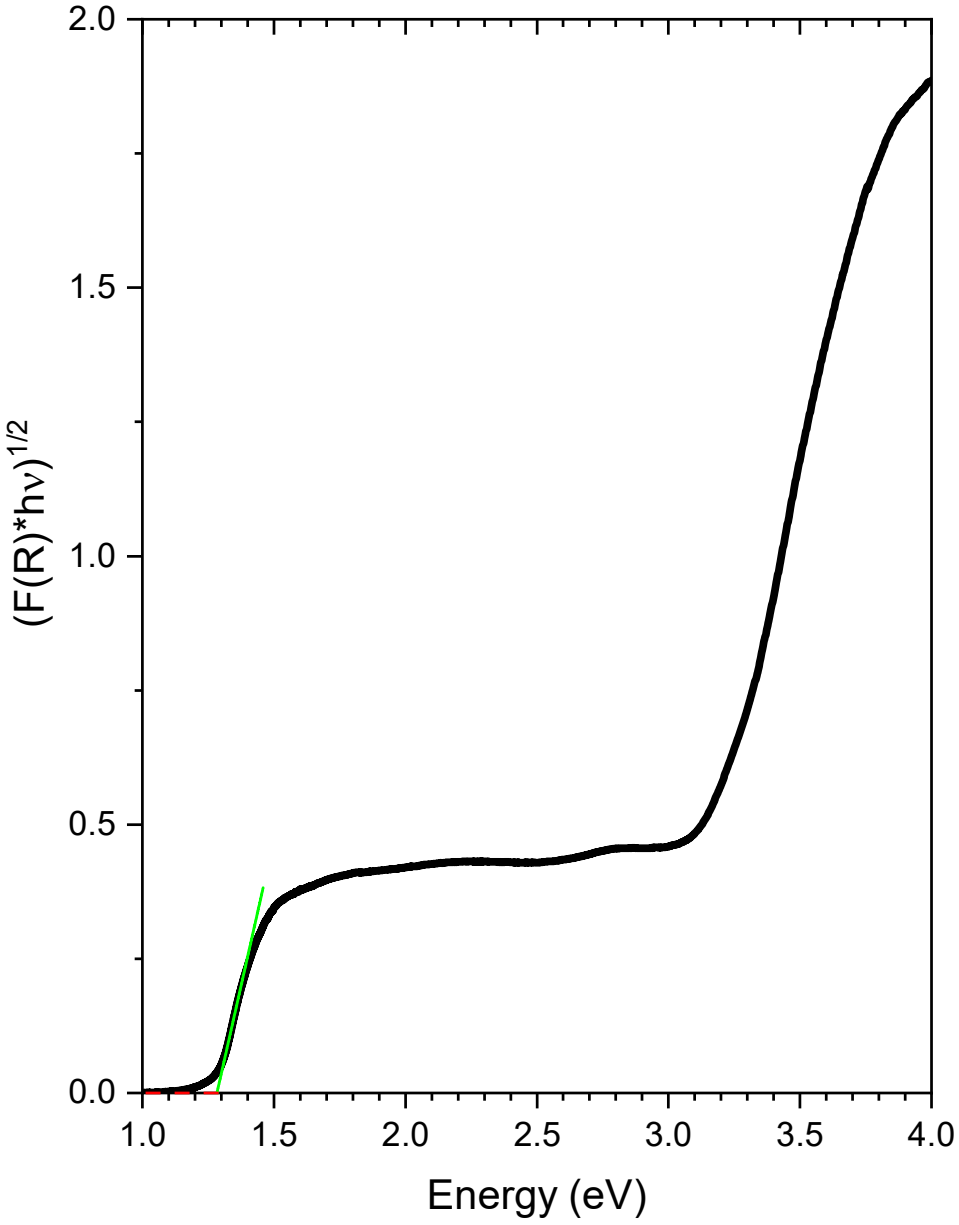

Figure A.15 Tauc plot analysis for determining the band gap of InP in 15 wt% InP/TiO_2.

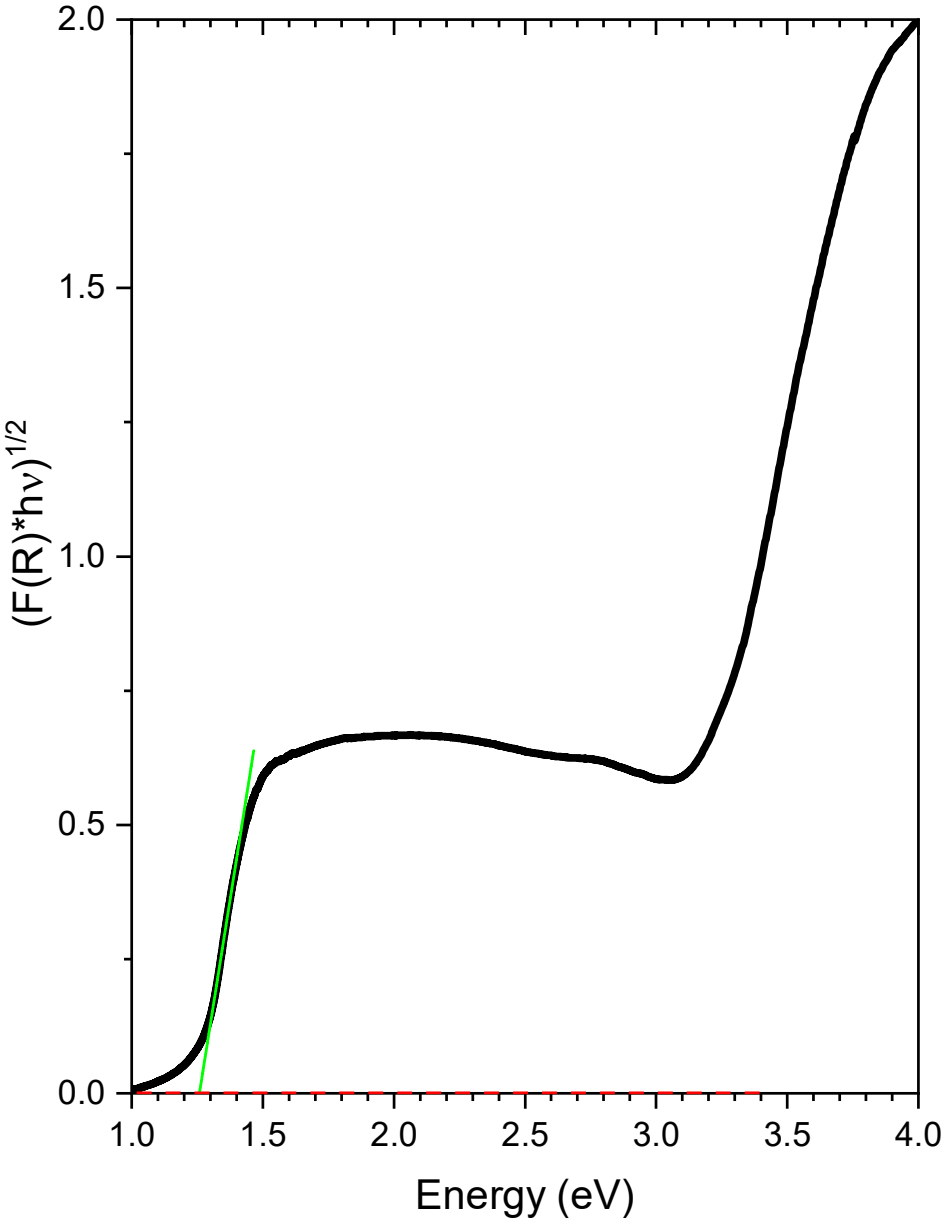

Figure A.16 Tauc plot analysis for determining the band gap of InP in 20 wt% InP/TiO_2.